UNIVERSITY OF CALIFORNIA SAN DIEGO

The global meridional overturning circulation in an idealized two-basin model

A dissertation submitted in partial satisfaction of the requirements for the degree
Doctor of Philosophy

in

Oceanography

by

C. Spencer Jones

Committee in charge:

Paola Cessi, Chair
Bruce Cornuelle
Ian Eisenman
Keiko Nomura
Shang-Ping Xie

2018

The Dissertation of C. Spencer Jones is approved, and it is acceptable in quality and form for publication on microfilm and electronically:

Chair

University of California San Diego

2018

EPIGRAPH

The fair breeze blew, the white foam flew,
The furrow followed free;
We were the first that ever burst
Into that silent sea.

Down dropt the breeze, the sails dropt down,
'Twas sad as sad could be;
And we did speak only to break
The silence of the sea!

All in a hot and copper sky,
The bloody Sun, at noon,
Right up above the mast did stand,
No bigger than the Moon.

Day after day, day after day,
We stuck, nor breath nor motion;
As idle as a painted ship
Upon a painted ocean.

Water, water, every where,
And all the boards did shrink;
Water, water, every where,
Nor any drop to drink.

Samuel Taylor Coleridge, *The Rime of the Ancient Mariner*

'The time has come,' the Walrus said,
'To talk of many things:
Of shoes – and ships – and sealing-wax –
Of cabbages – and kings –
And why the sea is boiling hot –
And whether pigs have wings.'

Lewis Carroll, *The Walrus and the Carpenter*

Table of Contents

List of Figures

List of Tables

ACKNOWLEDGEMENTS

Most of all I would like to thank my advisor, Paola, for her patience and helpful feedback without which this dissertation would not have been possible.

Christopher Wolfe, Matthew Mazloff and Ryan Abernathey taught me how to run the MITgcm and its various packages, and for this I will be forever grateful. The documentation is sometimes difficult and sometimes non-existent, so in-person help is invaluable. I should also thank my office-mate Ruth Musgrave, who helped when I was having more minor difficulties with the model, and Jinbo Wang for help with his particle advection code.

Then there is my committee: Bruce, Ian, Shang-Ping, David, and Keiko. All of these committee members provided helpful comments, especially Bruce who helped me learn how to interpret the output of the adjoint model. In addition, both Bruce and Ian have provided emotional support without which I would not be here today.

Next it seems only right to thank David Marshall and David Munday, who ignited my passion for oceanography and set me on the path to a PhD. They were great mentors gave me encouragement when I most needed it.

Speaking of great mentors, I would also like to thank Eric Chassignet, Claudia Cenedese, Paul Linden and Bruce Sutherland for their great advice during and after the GFD Summer Program.

I have too many friends and supporters to thank them all, but to name a few, I am indebted to Kate Adams, Marion Alberty, Navid Constantiou, Jess Carriere-Garwood, Nicole Couto, Sean Crosby, Yassir Eddebbar, Julia Fiedler Kannberg, Sean Haney, Eiren Jacobson, Peter Kannberg, Megan Liu, Jess Masich, Andy Mullen, Ruth Musgrave, Eric Orenstien, Anais Orsi, Nick Pizzo, Ben Reinemann, Kevin Sanchez, Anna Savage, Martha Schonau, Kate Snow, Peter Sutherland, Veronica Tamsitt, Chris Verlinden, Amy Van Cise, Greg Wagner and Kasia Zaba for their advice and support. Finally I'd like to thank my parents and my brother for their company, patience and help in times of difficulty.

Chapter 2, in full, is a reprint of the material as it appears in the Journal of Physical Oceanography 2016. Jones, C. S.; Cessi, Paola, American Meteorological Society, 2016.

Chapter 3, in full, is a reprint of the material as it appears in the Journal of Physical Oceanography 2017. Jones, C. S.; Cessi, Paola, American Meteorological Society, 2017.

Chapter 4, in full, has been submitted for publication in the Journal of Physical Oceanography 2018. Jones, C. S.; Cessi, Paola, American Meteorological Society, 2018.

Chapter 5, in full, is in preparation for submission to the Journal of Physical Oceanography. Jones, C. S.; Cessi, Paola, American Meteorological Society.

VITA

2011	Master of Physics University of Oxford
2018	Doctor of Philosophy Oceanography University of California San Diego

PUBLICATIONS

Components of salt transport in the upper branch of the Meridional Overturning Circulation.
C.S.Jones and Paola Cessi
submitted to Journal of Physical Oceanography

Size matters: another reason why the Atlantic is saltier than the Pacific
C.S.Jones and Paola Cessi
Journal of Physical Oceanography, **2017**, *47*

Warm-route versus cold-route: interbasin exchange in the meridional overturning circulation
Paola Cessi and C.S. Jones
Journal of Physical Oceanography, **2017**, *47*

Interbasin Transport of the Meridional Overturning Circulation
C.S.Jones and Paola Cessi
Journal of Physical Oceanography, **2016**, *46*

Gravity current propagation up a valley
Catherine S Jones, Claudia Cenedese, Eric P Chassignet, PF Linden and Bruce R Sutherland
Journal of Fluid Mechanics, **2015**, *762*

ABSTRACT OF THE DISSERTATION

The global meridional overturning circulation in an idealized two-basin model

by

C. Spencer Jones

Doctor of Philosophy

University of California San Diego, 2018

Professor Paola Cessi, Chair

This dissertation investigates the influence of ocean basin geometry on the stratification, circulation and salinity of the global ocean. This problem is studied using an idealized-geometry primitive-equation ocean-only model, in which two basins of different widths are connected by a re-entrant channel at the southern edge of the domain.

In addition to the primitive-equation model, we develop a conceptual model of the meridional overturning circulation (MOC). The conceptual model shows that if there is no deep-water formed in the wide basin, the northward Ekman transport into that basin must be returned southward by a geostrophic current. This geostrophic current flows southwards from the wide basin into the channel, and northwards from the channel into the narrow basin, balanced by the difference in the depth of isopycnals at the eastern boundaries of

each basin. The predictions of the conceptual model are confirmed in our primitive-equation model.

Under zonally uniform wind stress, temperature relaxation and freshwater flux, the primitive-equation model shows a preference for sinking in the narrower basin (which represents the Atlantic). The velocity field above a mid-depth isopycnal is a superposition of the wind-driven gyres and the MOC's upper branch in a western boundary current. This velocity field transports salt northward more efficiently in a narrower basin, causing the preference for narrow-basin sinking.

Characterizing the flow in the upper branch of the MOC using a pseudostream-function, we divide the salt transport into two components: transport by flow along open streamlines (which represents the warm-route transport) and transport by the gyres. We find that for larger interbasin flow, the northward salt transport along open streamlines in the sinking basin increases. We conclude that increasing the warm-route transport would bring more salt into the north of the Atlantic basin.

In the same idealized geometry, we explore the connection between the mid-depth and abyssal cells of the MOC. A ROC budget is used to visualize the pathway of the residual circulation: 40% of deep water formed in the north of the narrow basin is recycled through the abyss before returning to the upper ocean of the narrow basin.

Chapter 1

Introduction

The meridional overturning circulation (MOC) is a key component of the Earth's climate system. It transports heat northwards at all latitudes in the Atlantic. In equilibrium, this effect must be balanced by the atmosphere. At the equator, a southward atmospheric heat transport is achieved by a northward shift of the average position of the Inter-Tropical Convergence Zone, a region of low atmospheric pressure and high precipitation (Zhang & Delworth, 2005; Kang *et al.*, 2008). Weakening of Atlantic MOC (AMOC), which is predicted in the next 100 years (Collins *et al.*, 2013), may lead to regional dynamic sea level rise in the Atlantic (Levermann *et al.*, 2005), in addition to thermosteric and halosteric sea-level change caused by a reduction in northward heat and salt transport. The MOC also slowly flushes carbon-saturated water from above the thermocline into the deep ocean, allowing more anthropogenic carbon to be removed from the atmosphere (Maier-Reimer & Hasselmann, 1987) and reducing the strength of the greenhouse effect.

1.1 Background

In the Atlantic, Antarctic Intermediate Water (AAIW) flows northward, contributing to deep-water formation in the Labrador and Nordic Seas. Newly formed North Atlantic

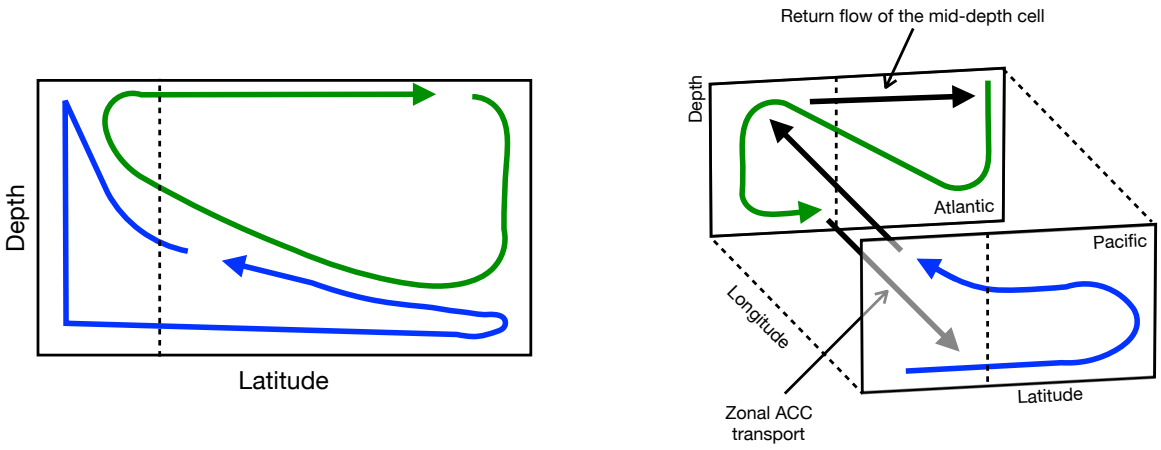

Figure 1.1: The mid-depth cell (green line) and abyssal cell (blue line) in the zonal average (left). A schematic of the continuous pathway (right), in which deep water is formed in the North Atlantic, flows southward and upwells in the Southern Ocean, where it feeds AABW formation (green line). This AABW then enters the Pacific and upwells across isopycnals (blue line), before returning to the Atlantic. The vertical dashed line indicates the latitude of the southern tip of Africa. Adapted from Thompson *et al.* (2016).

Deep Water (NADW) flows southward in a deep western boundary current (Stommel & Arons, 1959) and spreads eastward: NADW is found throughout the Atlantic basin between about 1500m and 3500m. Antarctic Bottom Water (AABW) is formed in the Weddell and Ross Seas and around Antarctica, proceeding northward into the basins below 3500m (Talley *et al.*, 2011).

The meridional overturning circulation (MOC) describes the three dimensional pathway water from the surface to depth and back again. In the zonal average, the MOC appears as two cells: 1) a mid-depth cell, in which AAIW flows northward, sinks in the North Atlantic to form NADW, flows southward at depth and upwells in the Southern Ocean; and 2) an abyssal cell, with formation of AABW in the Southern Ocean, diapycnal upwelling to intermediate depths and epipycnal return to the surface of the Southern Ocean (Lumpkin & Speer, 2007). A schematic of these two cells is shown in the left panel of figure 1.1.

Historically, it was thought that all deep water was returned to the surface by diapycnal diffusion (Stommel, 1958; Munk, 1966). Munk (1966) assumed that the ocean interior has uniform vertical diffusivity and that the downward diffusion of buoyancy is balanced by

upward advection. This implies that at low latitudes there is slow upwelling of cold deep water towards the surface. Munk (1966) found that in order for this diffusive upwelling to balance deep-water formation, the effective vertical diffusivity in the interior must be about $10^{-4}\,\mathrm{m^2\,s^{-1}}$, but measurements indicate that it is of the order $10^{-5}\,\mathrm{m^2\,s^{-1}}$ above 2000m depth and away from topography (Osborn, 1980; Whalen *et al.*, 2012; Waterhouse *et al.*, 2014). Assuming these estimates are representative of the whole ocean above 2000m, NADW cannot return to the surface by diapycnal diffusion alone.

Toggweiler & Samuels (1993, 1995) found that winds over the Southern Ocean set the strength of the mid-depth cell in a global ocean general circulation model with a more realistic vertical diffusivity of $3\times10^{-5}\,\mathrm{m^2\,s^{-1}}$. This brought about the more modern view that NADW follows isopycnals as it moves southward, upwelling adiabatically in the Southern Ocean where these isopycnals outcrop (Toggweiler & Samuels, 1998), as shown in figure 1.2. In this paradigm, NADW can return to the surface even if there is no vertical diffusion below the mixed layer. Toggweiler & Samuels (1995) argue that the mid-depth cell is driven by westerly winds over the Southern Ocean, which create a divergent Ekman transport at the surface, causing local upwelling.

Below 2000m, the vertical diffusivity is closer to $10^{-4}\,\mathrm{m^2\,s^{-1}}$ (Garabato *et al.*, 2004; Waterhouse *et al.*, 2014), allowing AABW to return to the surface by a combination of diapycnal upwelling below about 2000m and adiabatic upwelling in the Southern Ocean (dark blue region in figure 1.2).

Modern observations suggest that NADW is returned to the surface by a combination of wind-driven upwelling in the Southern Ocean and global diapycnal upwelling (Lumpkin & Speer, 2007; Talley, 2013). Upwelled water returns to the North Atlantic through the warm route via the Indonesian Throughflow (ITF; Gordon 1985), through the cold route via Drake Passage (Rintoul, 1991), and through the Tasman leakage (Speich *et al.*, 2002). Water from the ITF and Tasman leakage crosses the Indian Ocean and proceeds into the Atlantic via

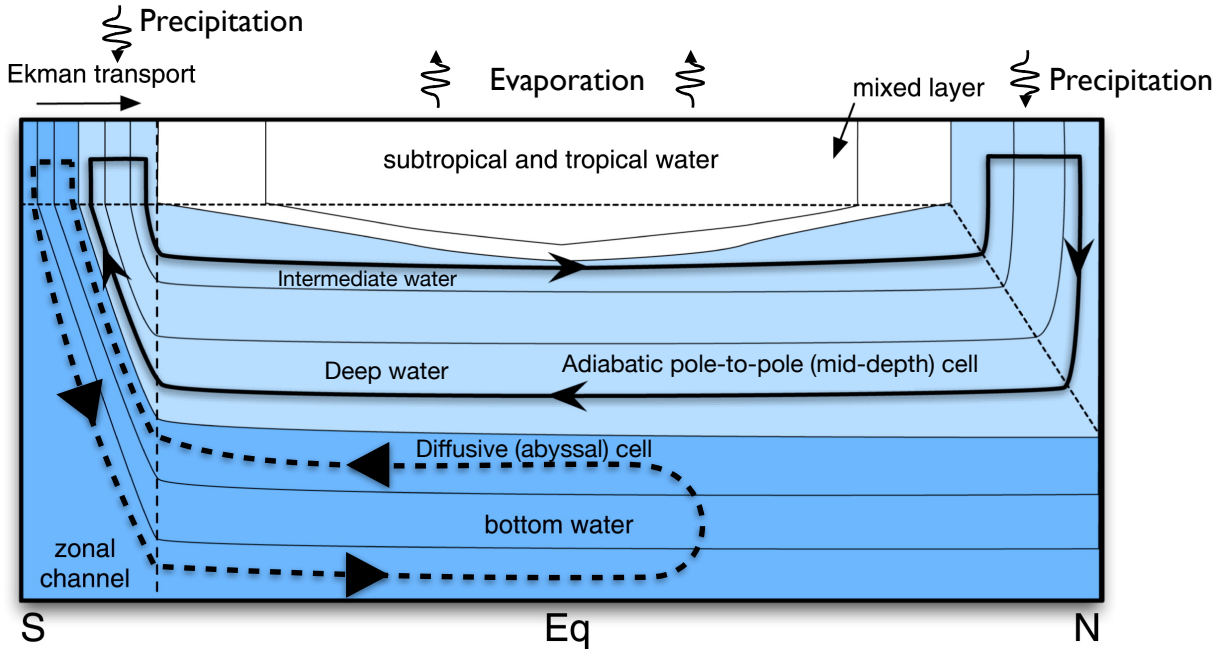

Figure 1.2: Schematic of the mid-depth cell and the abyssal cell in the Atlantic basin. In the light blue region, the isopycnals outcrop both in the Southern Ocean and in the North Atlantic. In this figure, the mid-depth cell is adiabatic, following isopycnals below the mixed layer. The isopycnals in the dark blue region outcrop in the Southern Ocean, but not in the North Atlantic, so the abyssal cell is closed by diapycnal upwelling at depth. Adapted from Wolfe & Cessi (2011)

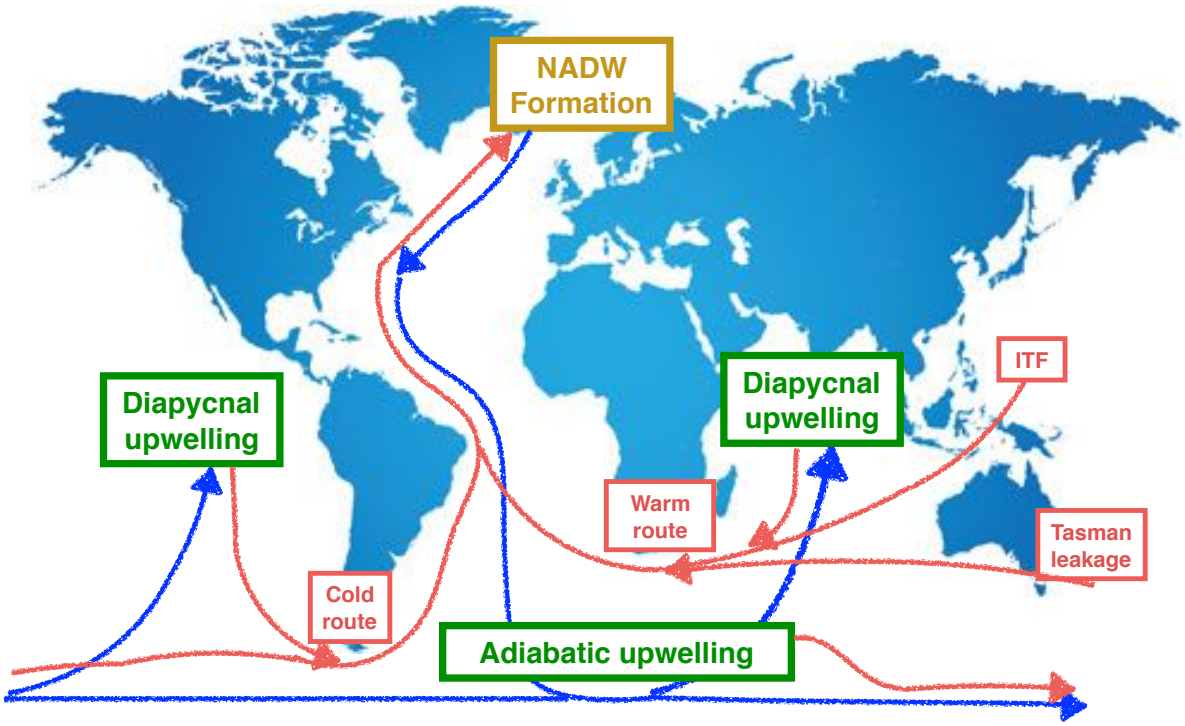

Figure 1.3: A schematic of the mid-depth cell of the meridional overturning circulation. North Atlantic Deep Water (blue lines) upwells along isopycnals in the Southern Ocean, and across isopycnals in the Indian and Pacific oceans. It then returns to the North Atlantic as intermediate water (pink lines), to sink again. The brown box indicates deep-water formation, the green boxes indicate upwelling and the pink boxes show the various pathways of the return flow.

the warm route. A schematic of these pathways is shown in figure 1.3.

The current view of the MOC is that strong westerly winds over the Southern Ocean drive northward Ekman transport. At the latitudes of Drake Passage, this transport is returned southward by geostrophic flow below the level of topography. This Eulerian circulation acts to steepen isopycnals, leading to baroclinic instability. The resulting eddies transport buoyancy across the Antarctic Circumpolar Current (ACC), releasing potential energy and reducing the isopycnal slope. The total buoyancy transport by the Eulerian circulation and the eddies is often described by the residual overturning circulation (ROC),

defined as the time and zonally averaged meridional transport at constant buoyancy, rather than at fixed depth levels (Marshall & Radko, 2003). Below the mixed layer of the Southern Ocean, the residual circulation is approximately adiabatic.

1.2 Conceptual models of the overturning circulation

Gent & McWilliams (1990) parametrized the tracer transport by mesoscale eddies to be proportional to the local slope of the isopycnals. Using this scaling, Gnanadesikan (1999) developed a conceptual model of the ROC for the mid-depth cell in a single basin. A schematic is shown in figure 1.4. This model parameterizes the Ekman, eddy, and diffusive transports, and deep water formation in the north of the basin, as a function of pycnocline depth. Then it predicts the strength of the overturning by applying volume conservation above the pycnocline. Both Gnanadesikan (1999)'s model and modern global circulation models predict that if Southern Ocean winds increase, the residual overturning strengthens and the pycnocline deepens. However in eddy-resolving models, the residual overturning is much less responsive to wind forcing, because an increase in Southern Ocean Ekman transport is compensated by an opposing increase in the eddy-induced transport (Hallberg & Gnanadesikan, 2006).

Another shortcoming of the Gnanadesikan (1999) model is that it divides the ocean circulation into the bulk transport by the winds, eddies, and diffusive upwelling across the pycnocline, but does not give any further information about the stratification or the vertical structure of the circulation. Marshall & Radko (2003) developed a continuous model for the stratification and the residual overturning circulation in the Southern Ocean. They average the buoyancy equation in time and along the streamlines of the ACC, to give

$$\overline{v}\frac{\partial \overline{b}}{\partial y} + \overline{w}\frac{\partial \overline{b}}{\partial z} + \frac{\partial}{\partial y}(\overline{v'b'}) + \frac{\partial}{\partial z}(\overline{w'b'}) = \frac{\partial B}{\partial z}\,, \tag{1.1}$$

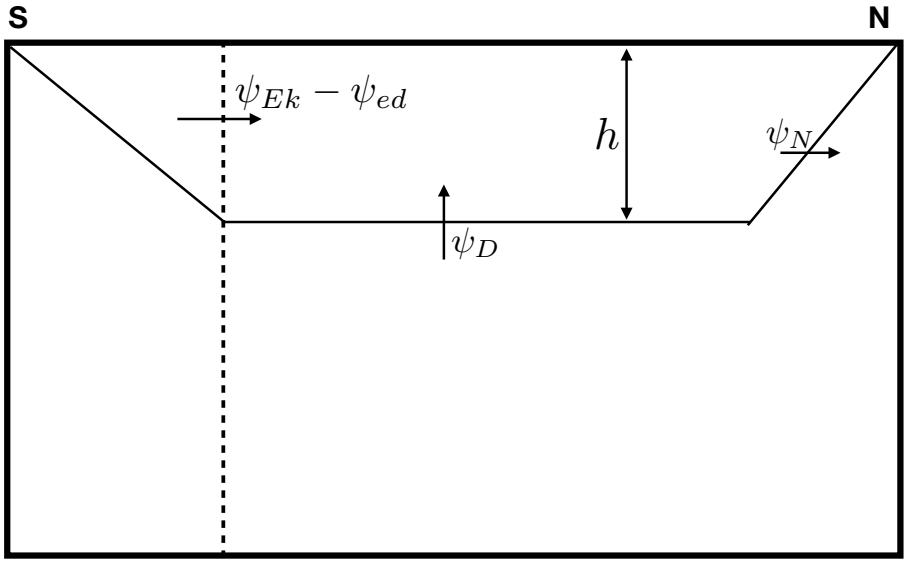

Figure 1.4: Schematic of Gnanadesikan (1999)'s model of the AMOC. The vertical dashed line represents the northern edge of the Southern Ocean. h represents the depth of the pycnocline, ψ_{Ek} represents the Ekman transport out of the Southern Ocean, ψ_{ed} represents the southward eddy transport, ψ_D is the cross-pycnocline transport due to diapycnal upwelling, and ψ_N represents the transport across the pycnocline due to deep water formation in the north of the basin. The vertical dashed line represents the northern edge of the re-entrant region. Adapted from Gnanadesikan (1999).

where b is the buoyancy, (v, w) are the meridional and vertical velocities, B is the surface buoyancy forcing, $\overline{}$ denotes the average along streamlines and in time, and $'$ denotes deviations from that average. Combining the Eulerian and eddy terms gives

$$J_{y,z,}(\Psi_{res}, \overline{b}) = \frac{\partial B}{\partial z} - \frac{\partial}{\partial y}\left[(1-\mu)\overline{v'b'}\right] , \tag{1.2}$$

where $\Psi_{res} = \overline{\Psi} + \Psi^*$ is the residual overturning streamfunction, $\overline{\Psi}$ is the Eulerian streamfunction, $\Psi^* = \overline{w'b'}/\overline{b_y}$ is the eddy streamfunction and $\mu = \left(\overline{w'b'}/\overline{v'b'}\right)\left(\overline{b_y}/\overline{b_z}\right)$ (Held & Schneider, 1999; Marshall & Radko, 2003). In the interior, $B = 0$ and the eddies are approximately adiabatic, so $\mu \approx 1$. Hence, the buoyancy is advected by the residual transport Ψ_{res}.

The Eulerian transport per unit width in the interior is given by $\overline{\Psi} = \overline{\tau}/\rho_0 f$, where $\overline{\tau}$ is the time-averaged wind stress along closed streamlines, f is the Coriolis parameter, and

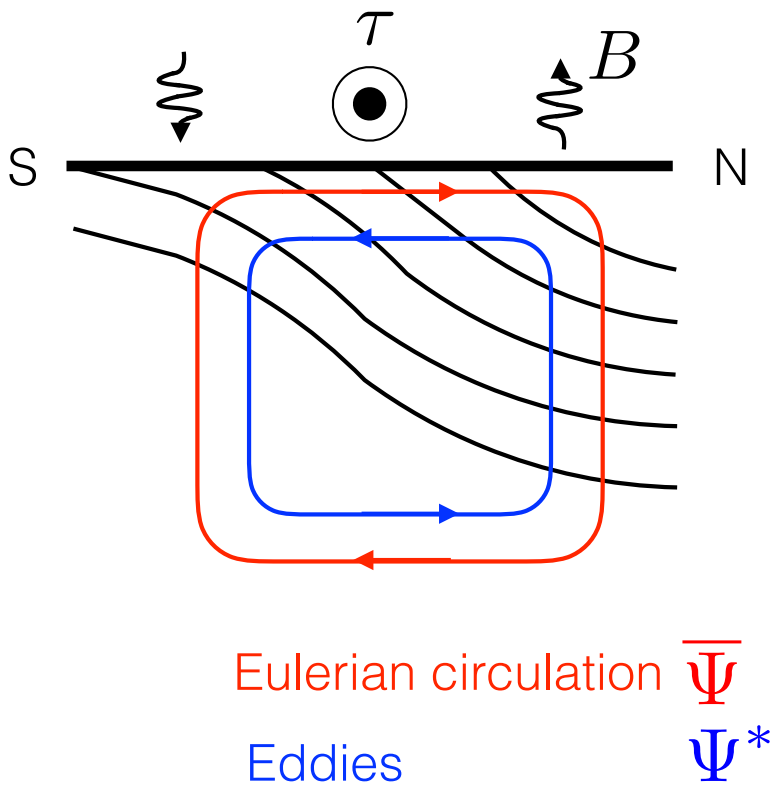

Figure 1.5: The residual overturning circulation, Ψ_{res}, in the Southern Ocean is a sum of the transport by the wind-driven Eulerian circulation, $\overline{\Psi}$ (red) and the eddies, Ψ^*(blue). The thinner black lines represent the isopycnals and the thick black line represents the surface. τ is the westerly wind stress over the ACC. B is the surface buoyancy flux. Adapted from Marshall & Radko (2003).

ρ_0 is the density, with Ekman layers at the surface and bottom and vertical transport in the interior (Karsten *et al.*, 2002).

Marshall & Radko (2003) solved equation (1.2), assuming that the eddy transport is proportional to the slope of the isopycnals. They found that the depth of the pycnocline is mostly determined by the wind stress and eddy strength, and the residual overturning circulation is approximately set by the buoyancy flux into the mixed layer. A schematic of the residual overturning in the Southern Ocean is shown in figure 1.5.

Marshall & Radko (2003)'s model only describes the ACC region, and only includes isopycnals that outcrop both in the Southern Ocean and in the North Atlantic. Wolfe &

Cessi (2011) proposed a continuous conceptual model of the mid-depth cell of the ROC in the adiabatic limit for a single basin. In this model, all diabatic processes take place in the mixed layer, and the transport of the eddies and the gyres are parameterized to be proportional to the isopycnal slope (though the eddy diffusivity in the basin is ten times that in the channel). This was the first conceptual model to parameterize the effects of the wind-driven gyres within the basin. There is no diffusive cell in this model, so the wind and eddies set the slope of isopycnals that outcrop in the Southern Ocean but not in the North Atlantic. The resulting stratification has thermostads that are representative of AAIW, NADW and AABW.

Nikurashin & Vallis (2012) introduced another continuous model of the ROC, modeling both the mid-depth and abyssal cells. The transport in the channel, basin and sinking region are parameterized and then matched where these regions meet. The models of both Wolfe & Cessi (2011) and Nikurashin & Vallis (2012) illustrate that a pole-to-pole circulation is only possible if 1) there are westerly winds over the Southern Ocean and 2) isopycnals exist that outcrop both in the Northern Hemisphere and the Southern Ocean.

Zonally averaged conceptual models do not describe the exchanges of volume, salt and heat between ocean basins. In particular, these models do not portray how mass is conserved in the Indo-Pacific: there is a northward Ekman transport into that basin but no deep water formation there, so mass must exit the Indo-Pacific sector and enter the Atlantic. In chapter 2, we address this question by extending Gnanadesikan (1999)'s model to two basins. We find that the Ekman transport into the Pacific is returned southward by a geostrophic transport, which then enters the Atlantic basin.

In our conceptual model, this geostrophic transport is balanced by the difference in pycnocline depth between the Atlantic and the Pacific. This difference provides an explanation for a long-held question in physical oceanography: why is the sea surface higher in the Pacific than in the Atlantic (e.g. Reid 1961)? We find that in order to balance the

geostrophic interbasin transport, mid-depth isopycnals in the Pacific must be deeper than in the Atlantic. Hence there is a larger volume of light water in the Pacific, leading to a higher sea surface.

Weakening of the AMOC due to climate change may lead to a reduction of the interbasin transport and hence a smaller difference in sea-surface height between the basins. Approximating the ocean as a two-layer system, changes in sea surface height, Δh, relate to changes in pycnocline depth, ΔD, by the relation

$$\Delta h = \Delta D \frac{\Delta \rho}{\rho}\,, \tag{1.3}$$

where $\Delta\rho/\rho$ is the relative density difference across the pycnocline. Wyrtki & Kendall (1967) find that $\Delta\rho/\rho \approx 5 \times 10^{-3}$ in the tropics. In the conceptual model discussed in chapter 2, reducing the number of isopycnals shared between the north of the narrow basin and the channel enough to give a 10% weakening in the overturning (which is the predicted weakening over the 21st century; Collins *et al.* 2013) causes the narrow basin's pycnocline to deepen by about 180m. This corresponds to a 90cm increase in sea-level, which is of the same order as the thermosteric and halosteric contributions to sea level change (Landerer *et al.*, 2007).

1.3 Salinity and deep water formation

To a good approximation, the temperature at the ocean surface is relaxed to the atmospheric temperature on a timescale of days, whereas the salt flux at the ocean surface is fixed. Therefore the velocity field controls the surface distribution of salt but has little influence on the surface temperature. A stronger AMOC transports more salt to high latitudes, strengthening the overturning, which transports more salt to high latitudes, and so on. This reinforcement is called the *salt-advection feedback* (Stommel, 1961).

Currently, deep water formation occurs in the North Atlantic because of the high

salinity (and density) there, but not in the North Pacific, where surface water at the same latitudes is much fresher (Warren, 1983; Broecker, 1991). Some isopycnals outcrop both in the Southern Ocean and in the North Atlantic: NADW flows southward along these isopycnals to replace surface waters driven northward by Southern Ocean winds. No such isopycnals connect the Southern Ocean with the North Pacific, so there is no significant deep water formation there. Weaver *et al.* (1999) summarizes a large number of explanations for the higher salinity of the North Atlantic.

In particular, evaporation and precipitation are thought to influence the location of sinking. The net freshwater flux into the North Atlantic is smaller than the flux into the North Pacific, causing an asymmetry in salinity between basins (Geay *et al.*, 2003). The different widths of the ocean basins may explain the lower surface freshwater flux in the Atlantic (Ferreira *et al.*, 2010; Nilsson *et al.*, 2013): the precipitation footprint of water that evaporates from the Atlantic extends into the Pacific, whereas the precipitation footprint of water that evaporates from the Pacific is contained completely within that basin.

Ferreira *et al.* (2010) and Nilsson *et al.* (2013) find a preference for narrow-basin sinking in coupled models, in which there are a large number of feedbacks between the ocean and the atmosphere. For example, the overturning transports heat northward more efficiently in the basin where deep-water formation occurs, causing more evaporation from the western boundary current, increasing the salinity and reinforcing the overturning. As a result of such feedbacks, it is difficult to separate the role of the atmosphere from that of the ocean in setting the location of deep-water formation. Thus, until now it was unclear how the width of the basins directly influences ocean velocities and how this affects the salinity distribution. In chapter 3, an ocean-only model is used to isolate the ocean's response to differences in basin width.

1.4 Warm-route salt transport

There may also be a preference for Atlantic sinking because the tip of Africa is at a much lower latitude than the tip of South America. The winds immediately south of Africa are westward, enabling warm-route flow into the Atlantic basin (Reid, 1961; Gordon, 1986; Nilsson *et al.*, 2013; Cessi & Jones, 2017), and allowing a supergyre to pass south of that continent. This supergyre joins the Atlantic, Indian and Pacific basins by passing south of Africa and Australia (Ridgway & Dunn, 2007).

Both the warm route and the supergyre may transport salt from the Indo-Pacific to the Atlantic (Gordon *et al.*, 1992; Ridgway & Dunn, 2007). No such salt transport into the Pacific is possible: the Americas end south of the zero-wind-stress-curl-line, which reduces the amount of westward transport possible in that region (Cessi & Jones, 2017). In addition, the high precipitation in Drake Passage would freshen any westward transport into the Pacific. This is one reason why the Pacific is fresher than the Atlantic, and why deep water is not formed in the Pacific.

In an idealized two-basin model, shortening the continent to the east of one of the basins increases that basin's salinity (Nilsson *et al.*, 2013; Cessi & Jones, 2017). This suggests that the northward salt transport intensifies, but it is not clear whether this change is effected by the gyres or by the MOC. Nilsson *et al.* (2013) partitioned the salt transport into a component effected by the gyres and a component effected by the overturning using Rahmstorf (1996)'s decomposition. This decomposition does not take into account that the upper branch of the overturning snakes around the gyres, as described by Stommel (1957), but rather approximates the northward transport as zonally uniform. In chapter 4, the salt transport in the idealized model is partitioned between the gyres and the interbasin flow as it snakes around the gyres. The effects of changing the strength of the warm-route interbasin transport are investigated.

1.5 Connections between the two cells

In the zonal average, the mid-depth and abyssal cells appear separate. However, recent work (Talley, 2013; Ferrari *et al.*, 2014, 2017) suggests that under present day conditions a portion of upwelled NADW contributes to abyssal-water formation in the Southern Ocean. From there, this abyssal water flows northward, upwelling in the Pacific before returning to the Atlantic and closing the circulation. This continuous pathway is shown in the right panel of figure 1.1. Analysis of observed tracer distributions suggests that about 25% of water in the deep Pacific originated in the North Atlantic (Gebbie *et al.*, 2010), but tracer analysis does not show the pathway of this water between basins.

The pathway of the circulation seems to be controlled by several factors. Ferrari *et al.* (2014) proposed that the MOC's mid-depth cell and abyssal cell were separated at the last glacial maximum (LGM). Upwelling of NADW is confined to the area north of the Antarctic sea-ice line, which was much further north during the LGM. Assuming the isopycnal slope in the Southern Ocean has not changed significantly, the maximum depth of NADW shoals as the sea ice line moves northward. The return flow of the abyssal cell is enabled by high diapycnal diffusivity below 2000m, so the cell cannot extend above this level. Thus the two cells were likely decoupled during the LGM.

Thompson *et al.* (2016)'s conceptual model builds on the work in chapter 2. In Thompson's model, NADW is usually recycled through the abyss (see the right panel of figure 1.1). However, if the vertical diffusivity is reduced above 2000m, the MOC transitions to the two-cell configuration for high rates of NADW formation. Chapter 5 examines the pathway of the MOC for parameters that give two-cell flow in Thompson's conceptual model.

1.6 Outline of this dissertation

1.6.1 Interbasin transport

Building on the work of Gnanadesikan (1999) and Allison (2009), chapter 2 advances a conceptual model of the mid-depth cell of the MOC. The geometry is shown in figure 1.6. Observations show that mid-depth isopycnals are deeper in the Pacific than in the Atlantic (e.g. Wolfe & Cessi 2011). Our conceptual model shows that this difference in isopycnal height is a consequence of deep water formation in the north of the Atlantic basin but not in the Pacific basin: it balances a geostrophic current that returns water from the Indo-Pacific to the Atlantic, completing the upper branch of the MOC.

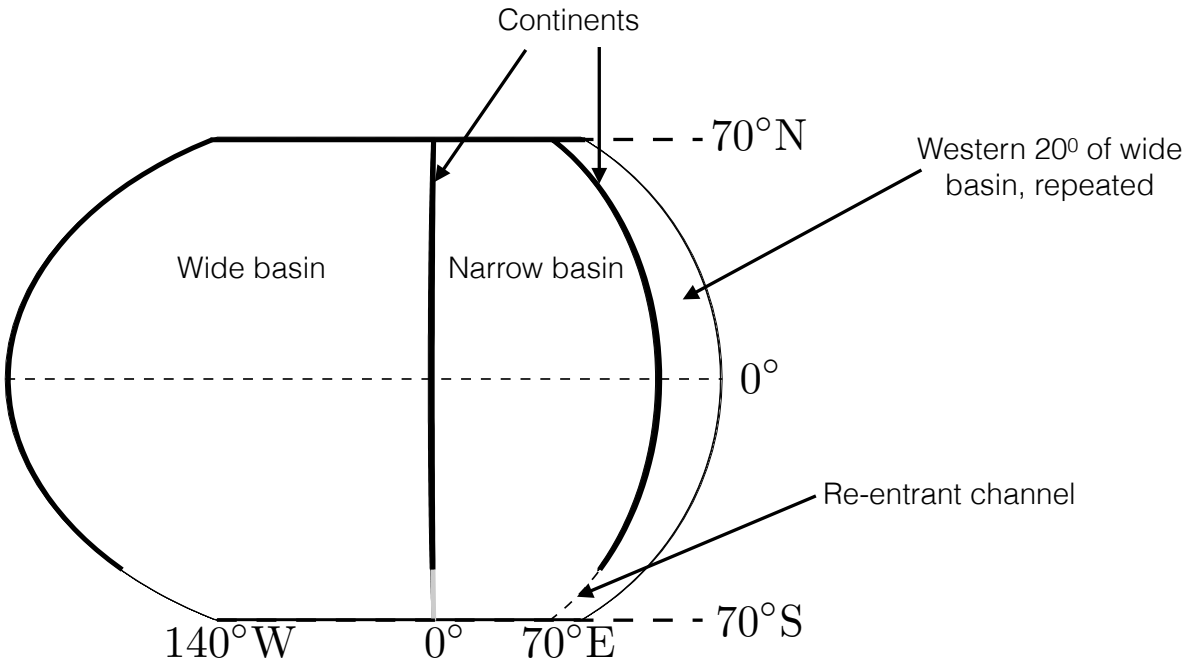

Figure 1.6: Geometry of the idealized model. The ridge is shown in grey and the land in black. The western 20° is repeated to the right of the figure. In chapters 2 and 3, the continents have equal length, extending to 52.5°S. In chapter 4, two experiments are performed in which one continent is shortened to end at 21°S. In chapter 5, the continent to the east of the narrow basin is shortened to end at 35°S.

Another important result of the conceptual model is that for both geometries the upper branch has about the same northward transport across the equator in the basin where

deep water is formed, regardless of its location. In other words, the transport-per-unit-width of the MOC is smaller in a wider basin.

We validated our conceptual model against a primitive equation model in the same geometry. This primitive equation model is further explored in chapter 3.

1.6.2 Basin width

Chapter 3 examines the effects of basin width on velocity and salinity in an ocean-only primitive-equation model. The model has two basins of different widths joined by a re-entrant channel south of 52.5°S, as shown in figure 1.6. It uses a vertical diffusivity of $2 \times 10^{-5}\,\mathrm{m^2\,s^{-1}}$, which is lower than the vertical diffusivity used in previous idealized models that explored the location of deep-water formation. For example, Marotzke & Willebrand (1991) use $5 \times 10^{-5}\,\mathrm{m^2\,s^{-1}}$ and Hughes & Weaver (1994) use a vertical diffusivity that increases with depth, exceeding $10^{-4}\,\mathrm{m^2\,s^{-1}}$ at 1000m. In this chapter, the narrow basin represents the Atlantic and the wide basin represents the Indo-Pacific. A preference for sinking in the narrower basin is found even for zonally uniform surface freshwater flux.

The sum of the gyres and the upper branch of the MOC (which is in a western boundary current) approximates the horizontal flow above a mid-depth isopycnal well in our primitive equation model (as predicted by Stommel 1957).

The transport in the interior of the subpolar gyre (SPG) is governed by the wind-stress-curl,

$$\beta \int_{-H}^{0} v_I \, dz \;=\; \frac{1}{\rho_0} \hat{\mathbf{k}} \cdot \nabla \times \boldsymbol{\tau} \,, \tag{1.4}$$

where ρ_0 is the density of the fluid, H is the depth of the basin and $\boldsymbol{\tau}$ is the vector wind stress field (e.g. Vallis 2006). This interior transport is returned by a western boundary current. Assuming the wind stress in the meridional direction is small, the western boundary current

transport is proportional to the width of the basin, L_x:

$$\Psi_{wbc} = -\int_0^{L_x} \int_{-H}^{0} v_I \, dz \, dx = L_x \frac{1}{\beta \rho_0} \frac{\partial \overline{\tau^x}}{\partial y} \,, \tag{1.5}$$

where Ψ_{wbc} is the transport of the western boundary current, τ^x is the wind stress in the zonal direction and v_I is the meridional velocity in the interior. The northward upper branch of the MOC cancels the southward western-boundary current of the SPG in a narrow basin. In a wider basin, the southward SPG western boundary current brings freshwater southward and eastward, reducing the surface density of the wide basin and causing a preference for narrow-basin sinking, as shown in chapter 3.

1.6.3 Salt transport by the warm route

In the idealized model from chapters 2 and 3, the return flow of the MOC follows the cold route into the narrow basin, passing eastward south of its western continent. When one continent is shortened to end north of the zero-wind-stress-curl line, most of the return flow follows the warm route westward south of the short continent (Cessi & Jones, 2017). Strengthening the warm route increases the salinity of the basin to the west of the short continent, causing deep-water formation in the north of that basin, regardless of its width.

Chapter 4 quantifies the salt transport of the warm-route interbasin current as it flows into the sinking basin and proceeds northward. Two experiments are performed: one in which the continent east of the narrow basin is shortened and one in which the continent east of the wide basin is shortened. The strength of interbasin transport is different in these two configurations. Characterizing the flow above a mid-depth isopycnal using a pseudostreamfunction, we divide the salt transport into two components: salt transport by flow along open streamlines (which represents the warm-route interbasin transport) and salt transport by the gyres. In the sinking basin, the flow along open streamlines transports salt

northward more efficiently in the geometry with the larger interbasin transport ie. when sinking occurs in the narrow basin, with the short continent positioned to the east of that basin.

The partition of the salt transport in these two configurations also supports the conclusions of chapter 3: when sinking occurs in the wide basin, the salt transport along streamlines is reduced between 40°N and 60°N. The pathway of the flow is pushed further south by the wind-driven subpolar gyre, which has a stronger western boundary current for a wider basin. As a result, there is an increased cross-streamline salt transport away from the sinking location at 40°N, freshening the north of the basin and inhibiting sinking.

1.6.4 Characterizing the global MOC

In chapter 5, a budget of the residual circulation is used to characterize the connection between the mid-depth and abyssal cells of the global overturning. Again, we use a primitive equation model with the domain shown in figure 1.6. The continent to the west of the narrow basin extends from 52.5°S to 70°N and the continent to the east of the narrow basin extends from 35°S to 70°N. In the southernmost 2° of the domain, a heat flux out of the ocean is added to the model used in the previous chapters. This heat flux models the effects of sea ice (Ferrari *et al.*, 2014). The diffusivity below 2000m is increased to $2 \times 10^{-4}\,\mathrm{m^2\,s^{-1}}$, allowing an abyssal cell to form (Jansen & Nadeau, 2016).

A thickness-weighted average residual budget finds that about 40% (about 5Sv) of newly-formed deep water leaving the narrow basin sinks into the abyss before returning to the surface (see figure 1.1). Of this 5Sv, about 2Sv travels through the abyss of the narrow basin and about 3Sv travels through the abyss of the wide basin. An adjoint tracer is released in the abyss of the wide basin: the adjoint tracer content of the upper ocean suggests that 2.5Sv of deep water formed in the narrow basin is recycled through the abyss of the wide basin.

Chapter 2

Interbasin transport of the meridional overturning circulation

2.1 Introduction

In the current climate system, deep water is formed in the North Atlantic, but not in the North Pacific, resulting in a global meridional overturning circulation (MOC) which transports heat northward in the Atlantic and contributes to a more marked southward heat flux in the South Indo-Pacific. The MOC is a global cell, driven by the wind-induced upwelling in the circumpolar region (Toggweiler & Samuels, 1993; Wolfe & Cessi, 2011), as well as by diffusive upwelling at the interface between the deep and abyssal waters (Stommel & Arons, 1959; Munk, 1966), dominated by the contribution in the Indo-Pacific sector. The upwelling in the circumpolar portion of the domain and in the passive basin – the Pacific – is balanced by downwelling near the northern end of the active basin – the Atlantic. This global circulation implies a transfer of intermediate water from the passive into the active basin (with a transfer of deep water in the opposite direction). This transfer occurs in the circumpolar region, as detailed in Talley (2013) (there is also a small exchange through the Bering Strait, which we neglect henceforth). The transfer of water between the basins is

geostrophically balanced at the southern boundary of each semi-enclosed basin, requiring a difference in the depth of the isopycnals separating the intermediate and deep waters at the eastern boundary of each basin. Specifically, these isopycnals are deeper in the South Pacific than in the South Atlantic in the present day MOC as noted by Reid (1961). More recent observations from the *World Ocean Altas* (Locarnini *et al.*, 2006; Antonov *et al.*, 2006) confirm that isopycnals near 1000m depth are shallower in the Atlantic than in the Indo-Pacific (see figure 2.1). The strength of the inter basin flow is set by the amount of Ekman transport and the upwelling into the intermediate waters of the Indo-Pacific. The interbasin transfer is only one component of the total transport that forms the upper branch of the MOC: in addition to the interbasin flow, the MOC, or more precisely the residual overturning circulation (ROC), must carry all of the Ekman transport that occurs along the northern boundary of the Antarctic Circumpolar Current (ACC) region, minus the eddy-flux of buoyancy at this boundary, as well as the diapycnal upwelling in the Atlantic.

The mechanism for size-dependent interbasin transport is illustrated here by considering a generalization of the model by Gnanadesikan (1999) to two basins connected by a circumpolar region. A geostrophically balanced interbasin flow, ψ_g, which transfers water from the passive basin to the active basin, is necessary to satisfy the buoyancy budget (as shown in figure 2.2). The depth of the intermediate water layer must be deeper in the passive basin than in the active basin in order to geostrophically balance the interbasin flow. The transfer from the passive to the active basin is fed by diffusive upwelling and Ekman transport into the passive basin, and therefore the transfer is larger when the passive basin is wider. This simple model does not capture the richness of the horizontal and vertical structure of the ROC velocity field, spanning both the active and the passive basins, which we diagnose from three-dimensional numerical integrations.

These three-dimensional integrations follow the approach of Hughes & Weaver (1994) and Marotzke & Willebrand (1991), that is we use an ocean-only model with drastically

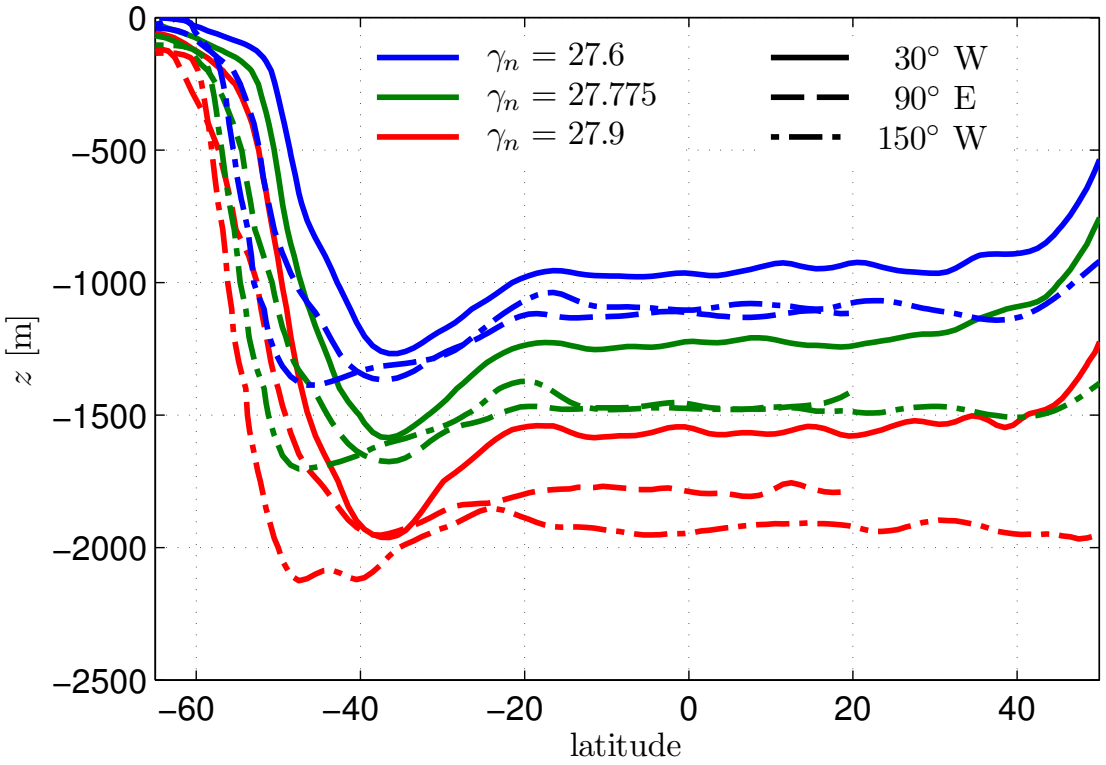

Figure 2.1: Depth of three middepth neutral density γ_n surfaces as a function of latitude at three longitudes corresponding to the Atlantic (30°W), Indian (90°E), and Pacific (150°W) Oceans. Lines that are the same color represent the same value of γ_n , whereas lines that are the same style represent the same longitude. From Wolfe & Cessi (2011).

simplified geometry and forcing. There is a two-basin geometry in which the latitudinal extent of the two basins is the same. In this, we differ from the basic configuration of Hughes & Weaver (1994), who specified that the Atlantic-like basin extends further north than the Pacific-like basin. The purpose of our configuration is to determine the consequences of differences in the longitudinal extent of the Atlantic- and Pacific-like basins. We confine our analysis to the weakly diffusive regime, where the ROC has a substantial adiabatic component associated with the wind-driven upwelling in the circumpolar portion of the domain (Toggweiler & Samuels, 1993; Wolfe & Cessi, 2011).

The partition of the MOC between the Atlantic and Indo-Pacific sector in an idealized domain was also studied by Stocker & Wright (1991), using a zonally averaged model, with a parametrization relating the East-West pressure gradient to the North-South one. They

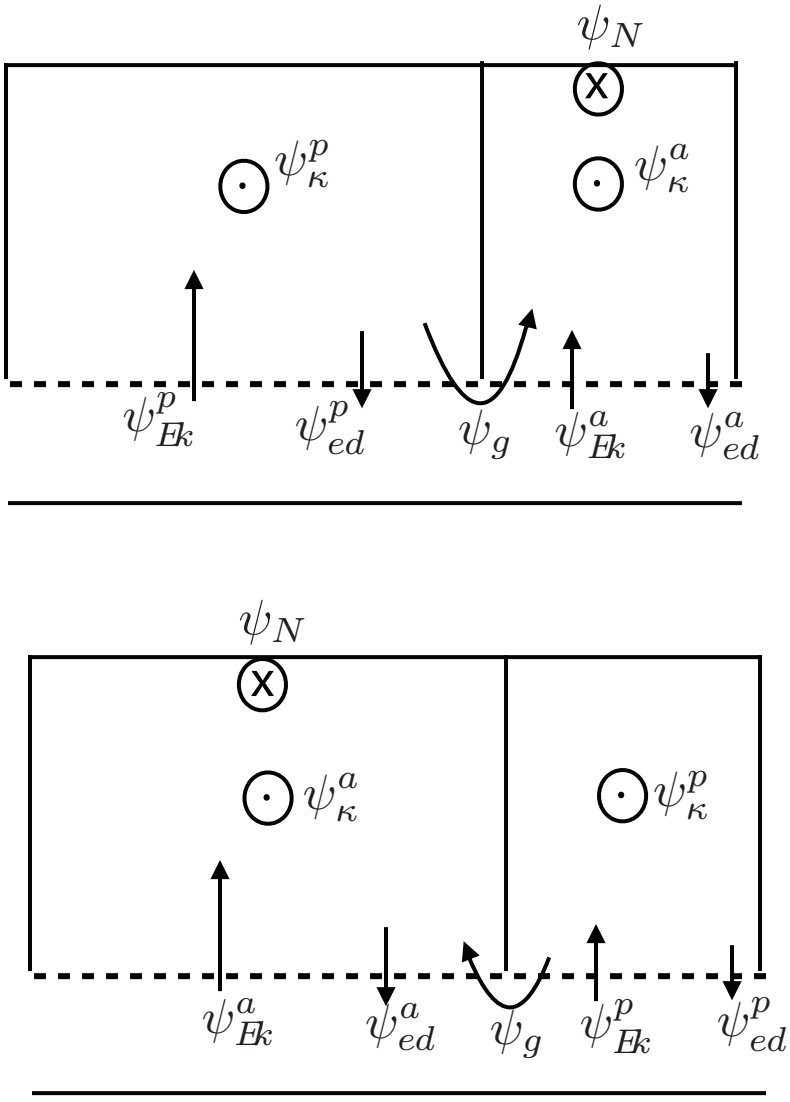

Figure 2.2: Schematic of the two-basin box model, showing the transport budget above the isopycnal bounding the upper branch of the residual overturning circulation (ROC) for sinking in the narrow basin (top) and wide basin (bottom). $\otimes$ denotes sinking (transport from the upper layer into the lower layer) and $\odot$ denotes upwelling (transport from the lower layer into the upper layer). ψ_N represents northern sinking in the active basin, ψ_κ diapycnal upwelling, ψ_{Ek} the Ekman transport at the northern edge of the channel region, ψ_{ed} the eddy-fluxes at the northern edge of the channel region, and ψ_g a geostrophic exchange transport, which flows out of the passive and into the active basin in the upper layer.

found that under zonally symmetric forcing, the system settles into a state with two separate overturning cells with sinking at the northern edge of both the North Atlantic and the North Pacific, and little transfer between the two basins. Some ocean-only studies (Seidov & Haupt, 2005) find that it is necessary to impose an asymmetry in the surface salinity or freshwater flux to achieve a conveyor-like global overturning circulation, while others find that multiple states exist depending on the initial conditions (Huisman *et al.*, 2009). Nilsson *et al.* (2013) find that in a coupled model, conveyor-like states exist (in which sinking in occurs in only one basin) as well as a northern-sinking state (in which sinking occurs in the north of both basins). In the quasi-adiabatic regime, we find that under longitudinally symmetric forcing, stable sinking is obtained only at the northern end of the narrow basin, a state which maximizes the inter-basin exchange of the ROC. No other states exist for symmetric forcing. In order to achieve sinking in the wide basin, the surface forcing is modified to decrease precipitation over the wide basin. The interbasin transport ψ_g in each of these states compares well to the predictions of the two-basin zonally-average model.

Section 2 proposes an idealized zonally average model adapted from Gnanadesikan (1999). The numerical model setup and some of the diagnostics are described in section 3. Section 4 describes the numerical model states and section 5 illustrates the horizontal structure of the flow in the ROC. A summary and concluding remarks are given in section 6.

2.2 A minimal model of two basins exchanging transport

Here, we consider an extension of Gnanadesikan (1999) model of the ROC to two basins coupled by a circumpolar connection, as sketched in figures 2.2 and 2.3. This model is very similar to that developed in Allison (2009); however in that model the lengths of

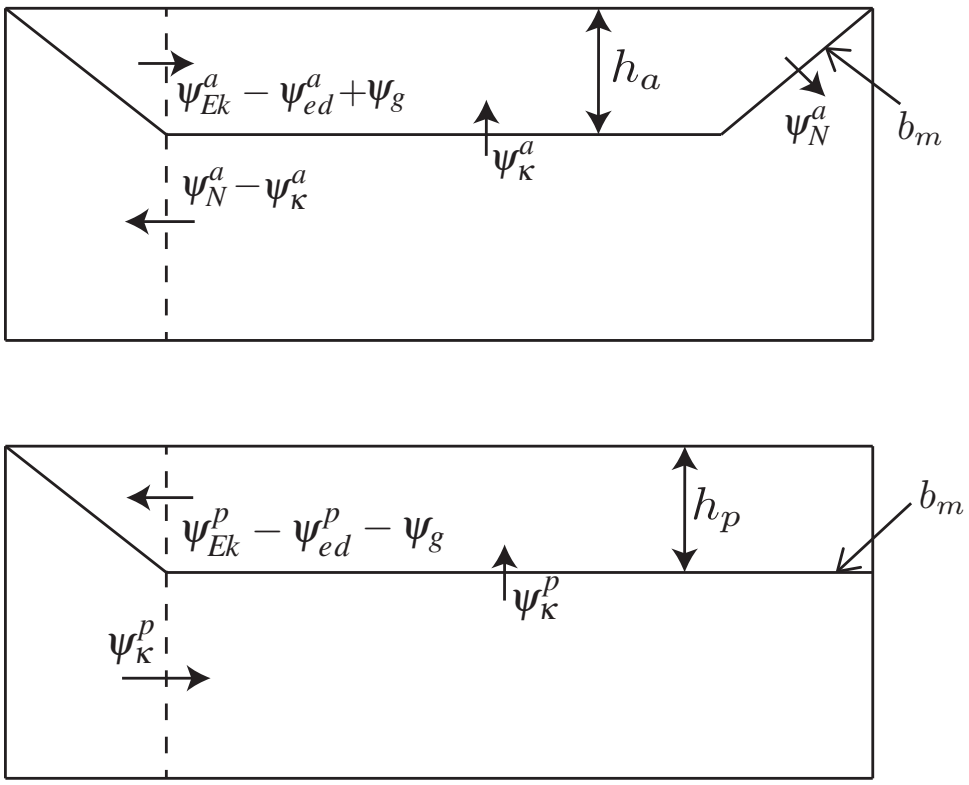

Figure 2.3: Schematic of the two-basin box model, showing the transport budget above the isopycnal bounding the upper branch of the ROC for the active basin (top) and passive basin (bottom). b_m is the isopycnal that divides the upper layer and the lower layer and $h_{a,p}$ denotes the height of the upper layer. The other symbols are defined in figure 2.2.

the boundaries are different. It crudely captures the circulation in the upper branch of the ROC; the upper branch is defined to be the layer above the isopycnal b_m, that divides the intermediate water from the deep water. In the context of this model, the layer above b_m is referred to as the upper layer and the layer below b_m is referred to as the lower layer. Thickness is transferred between the layers through northern sinking, diapycnal upwelling, Ekman and eddy fluxes.

From figure 2.2, we can see that the buoyancy budget of the upper layer for the semienclosed portions of each basin is given by

$$\psi^a_{Ek} - \psi^a_{ed} + \psi^a_\kappa + \psi_g = \psi_N \,, \tag{2.1}$$

$$\psi^p_{Ek} - \psi^p_{ed} + \psi^p_\kappa - \psi_g = 0 \,, \tag{2.2}$$

where ψ_{Ek} denotes the Ekman transport entering the basins from the circumpolar region, ψ_{ed} is the transport of buoyancy by eddy fluxes southward into the channel region (modeled here using the Gent-McWilliams parametrization: see section 2.3), ψ_κ is a diapycnal exchange of buoyancy across the isopycnal b_m, ψ_g is the geostrophically balanced exchange that results from the difference in zonal flow in the two sectors of the circumpolar domain and ψ_N is the transport due to sinking at the northern edge of the domain. We choose to explore the special case in which sinking ψ_N only occurs in one basin or the other. The superscripts "a" and "p" refer to the active and passive basins respectively.

In this model the depth of the isopycnal b_m is given by h_a in the active basin and h_p in the passive basin, as shown in figure 2.3. Following Gnanadesikan (1999), we can substitute standard expressions for Ekman, eddy, diapycnal and geostrophic transports into equations (2.1,2.2), to arrive at the system

$$\underbrace{-\frac{\tau_s L_a}{\rho_0 f_s}}_{\psi^a_{Ek}} - \underbrace{\frac{\kappa_{GM} h_a L_a}{L_c}}_{\psi^a_{ed}} + \underbrace{\frac{\kappa A_a}{h_a}}_{\psi^a_\kappa} - \underbrace{\frac{g'(h_p^2 - h_a^2)}{2 f_s}}_{\psi_g} = \underbrace{g' \frac{h_a^2}{2 f_n}}_{\psi_N}, \tag{2.3}$$

$$\underbrace{-\frac{\tau_s L_p}{\rho_0 f_s}}_{\psi^p_{Ek}} - \underbrace{\frac{\kappa_{GM} h_p L_p}{L_c}}_{\psi^a_{ed}} + \underbrace{\frac{\kappa A_p}{h_p}}_{\psi^p_\kappa} + \underbrace{\frac{g'(h_p^2 - h_a^2)}{2 f_s}}_{\psi_g} = 0\,. \tag{2.4}$$

We have denoted the widths of the basins with $L_{a,p}$, τ_s is the wind-stress that drives Ekman transport out of the re-entrant channel, f_s is the Coriolis parameter at the southern boundary of the semi-enclosed portion of the domain, f_n is the Coriolis parameter at 57.5°N, L_C is the meridional extent of the circumpolar channel, κ_{GM} is the coefficient of Gent-McWilliams eddy-fluxes parametrization, κ is the interior diapycnal diffusivity, $A_{a,p}$ is the area of the semi-enclosed basins, g' is the range of surface buoyancies shared by the sinking and circumpolar regions. τ_s is the average wind-stress along the northern-most closed barotropic streamline in the circumpolar region. This is the most appropriate definition of the northern edge of the re-entrant channel (Marshall *et al.*, 2016). The values of the prescribed parameters are

Table 2.1: The external parameters for the simplified two-basin transport budget, as deduced from the numerical simulations.

Parameter	Value	Notes
κ_{GM}	$500\,\mathrm{m^2\,s^{-1}}$	Value used in the numerical model.
L_p	10000km	Width of the wide basin at the channel edge.
L_a	5000km	Width of the narrow basin at the channel edge.
L_c	2000km	North-South extent of the channel.
A_a	$4 \times 10^{13}\mathrm{m^2}$	Area of the narrow basin north of the channel and south of the equator.
A_p	$8 \times 10^{13}\mathrm{m^2}$	Area of the wide basin north of the channel and south of the equator.
ρ_0	1000kg $\mathrm{m^3}$	The average density.
$f_n = -f_s$	$1.2 \times 10^{-4}\,s^{-1}$	$\lvert f\rvert$ at 57.5°S, the northern edge of the channel.
κ	$2 \times 10^{-5}\,\mathrm{m^2\,s^{-1}}$	Value used in the numerical model.
τ	0.1	Average wind stress along the northernmost barotropic contour in the re-entrant channel
g'	$0.004\ \mathrm{m\,s^{-2}}$	Approximate range of buoyancy shared between the channel and the northern end of the active basin.

given in table 2.1.

The novel term here is the geostrophic transport ψ_g exchanged between the two basins, proportional to the difference between the squared heights of the upper layer at the eastern boundaries of each basin. At the southern edge of the semi-enclosed region, the height of the upper layer at the eastern boundary of one basin must be equal to the height of the upper layer at the western boundary of the other basin, in order to ensure no normal flow into the southern edge of the continent. In the system (2.3,2.4) we identify the characteristic depth of the isopycnal b_m in each basin with its depth at the eastern boundary. Therefore the geostrophic transport ψ_g into the upper layer of the active basin is proportional to the squared height of the upper layer at the eastern edge of the active basin, h_a, minus the squared height of the upper layer at the eastern edge of the passive basin, h_p. The geostrophic transport into the passive basin is $-\psi_g$, because the two heights are switched.

The system (2.3,2.4) can be solved for $h_{a,p}$, given the external parameters for geometry, forcing and diffusion. With the formulation (2.3,2.4), sinking in the narrow basin and

sinking in the wide basin can be studied by simply exchanging the values of L_a, A_a with L_p, A_p.

Taking the sum of (2.3) and (2.4), ψ_g cancels out and we find

$$\psi^a_{Ek} - \psi^a_{ed} + \psi^p_{Ek} - \psi^a_{ed} + \psi^a_\kappa + \psi^p_\kappa = \psi_N \,. \tag{2.5}$$

Assuming that the difference in isopycnal heights is small compared with their total depth, i.e. $h_p = h_a + \epsilon$, with $\epsilon \ll h_a$, it is clear that the total amount of sinking ψ_N is, to leading order in ϵ, the same as that obtained in a single basin whose width is $L_a + L_p$ and whose area is $A_a + A_p$. In the same limit, the difference in isopycnal heights, $\epsilon \equiv h_p - h_a$, is given by

$$\epsilon \left[\frac{\kappa_{GM}}{L_c} + \frac{\kappa L_c}{h_a^2} + \frac{g' h_a (L_a + L_p)}{L_a L_p |f_s|} \right] = g' \frac{h_a^2}{2 f_n L_a} \,. \tag{2.6}$$

This shows that $\epsilon > 0$, i.e. the isopycnal b_m is always deeper in the passive basin, because the term inside the square bracket on the left hand side (lhs) of (2.6) is always positive, as is the right hand side (rhs). In addition (2.6) shows that ϵ and ψ_g are larger when sinking occurs in the narrow basin: if we exchange L_a with L_p, the term inside the square bracket on the lhs remains the same, while the rhs decreases. The resulting depths, $h_{a,p}$, and associated transport for sinking in the narrow or wide basin are given in table 2.2, for the parameters used listed in table 1. We choose the cases $L_a = 2L_p$ and $L_p = 2L_a$. However, it is of interest to note that if $A_a \to 0$, $h_a \sim h_p/\sqrt{2}$ and when $A_p \to 0$, $h_a \sim h_p$.

The essential point is that sinking in the narrow basin leads to a larger inter-basin flow, and a larger residual circulation per unit width, than sinking in the wide basin. The reason for this asymmetry is simple: if sinking occurs in the narrow basin then all of the residual flow entering the upper layer in the wide basin, through Ekman transport (minus the eddy contribution) and diapycnal mixing, must enter the narrow basin to sink, adding

Table 2.2: Results of the simplified two-basin model, based on equations (2.3,2.4), compared to the numerical MITgcm simulations.

	Sinking in the narrow basin	MITgcm in narrow sinking	Sinking in the wide basin	MITgcm wide sinking
ψ_N	11.3Sv	11.8Sv	11.9Sv	11.9Sv
ψ_g	7.2Sv	8.2Sv	3.8Sv	3.1Sv
ψ^p_{Ek}	8.3Sv		4.2Sv	
ψ^a_{Ek}	4.2Sv		8.3Sv	
ψ^p_{ed}	2.6Sv		1.2Sv	
ψ^a_{ed}	1.0Sv		2.1Sv	
ψ^p_κ	1.5Sv		0.8Sv	
ψ^a_κ	1.0Sv		1.8Sv	
h_a	824m	841m	845m	821m
h_p	1055m	1016m	970m	882m

to the Ekman transport directly entering the active basin. Regardless of the location of sinking the residual transport is given by the sum of the Ekman transport at the northern edge of the channel (minus the eddy transport), and the diapycnal upwelling throughout both basins. Thus, the transport *per unit width*, is larger when sinking occurs in the narrow basin.

In the following section the predictions of this simple box model are examined with a three-dimensional primitive equation GCM.

2.3 Model and diagnostics

The numerical model employed is the Massachusetts Institute of Technology general circulation model (MITgcm, Marshall *et al.*, 1997*a*,*b*), which integrates the hydrostatic, Boussinesq primitive equations. The domain is a spherical sector spanning 140° in latitude and 210° in longitude with a 1° horizontal resolution. The geometrical configuration comprises two idealized basins, one twice as wide as the other, joined by a re-entrant channel of latitudinal width 17.5° at the southern edge of the domain as shown in Figure 2.4. The bottom is flat and 4000m deep, except for a sill in the periodic channel, one-grid point wide

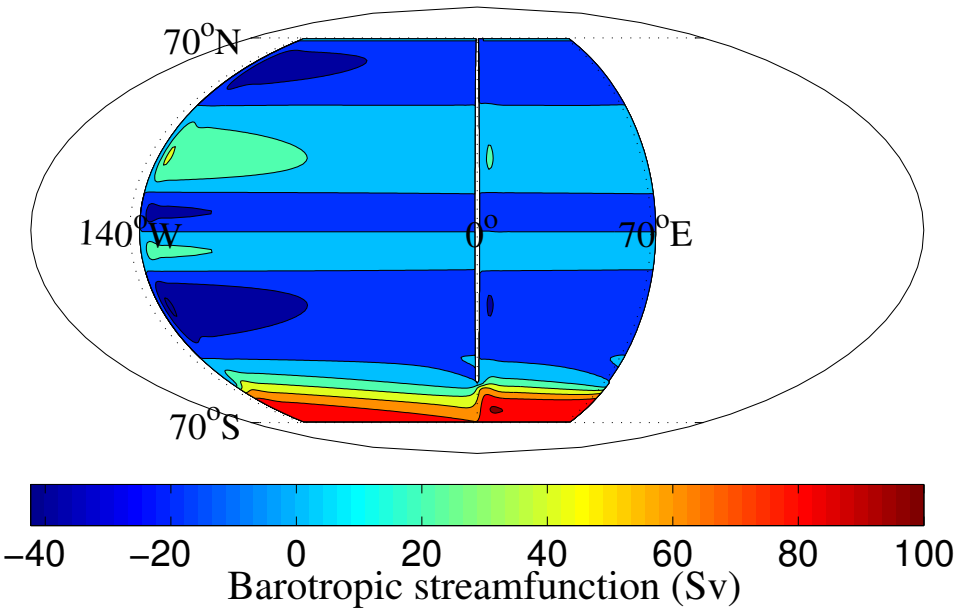

Figure 2.4: Barotropic streamfunction and geometry of the domain used in the computations. The domain is 210°-periodic and 4000m deep.

and 1333m high, located immediately south of the narrow basin's western boundary.[1] There are 32 unequally spaced levels in the vertical, ranging from a minimum spacing of 13.6m at the top to a maximum of 286m at the bottom.

The equation of state is linear, so that the buoyancy is described by

$$b = g[\alpha_T T - \beta_S (S - S_{ref})]\,, \tag{2.7}$$

where $\alpha_T = 2 \times 10^{-4}\,^\circ\mathrm{C}^{-1}$, $\beta_S = 7.4 \times 10^{-4}$ and $S_{ref} = 35$. Salinity is given on the practical salinity scale and therefore it is quoted without units.

[1]The experiments described here have been repeated in a domain with two sills, one at the southern end of each boundary. The qualitative properties of these experiments are the same, confirming that the sill does not cause the preference for narrow basin sinking.

The surface forcings are steady and zonally-uniform: the expressions for the wind stress, τ, freshwater flux, F, and distribution to which the surface temperature is relaxed, T^* are given by

$$\tau = \tau_{Max}\left(-\cos(3\pi\theta/140) + e^{-\theta^2/\sigma^2}\right), \tag{2.8}$$

$$F = F_{s0}\left(\cos(7\pi\theta/8\Theta) - 2e^{-(\theta/\Theta).^2/(2\sigma_F^2)}\right) - F_0\,, \tag{2.9}$$

$$T^* = T_{eq}\left(\cos(\pi\theta/140)^2 + 0.1e^{-(\theta/2\Theta-1)^2}\right). \tag{2.10}$$

We adopt the following notation: θ is latitude in °, $\tau_{Max} = 0.11\,\mathrm{Pa}$, $\sigma = 10°$, $F_{s0} = 2\times 10^{-8}\,\mathrm{m\,s^{-1}}$, $\sigma_F = 0.128$, $\Theta = 60°$ and $T_{eq} = 25°\mathrm{C}$. The relaxation time-scale for the surface temperature is 10 days. The constant F_0 is defined such that the area averaged freshwater flux $\langle F\rangle = 0$. The freshwater flux is then turned into a virtual salt flux by multiplying F by -35. The distributions of τ, F, and T^* as a function of latitude are shown in figure 3.2.

Momentum is dissipated via Laplacian viscosity with horizontal and vertical coefficients $\nu_h = 4\times10^4\ \mathrm{m^2\ s^{-1}}$ and $\nu_v = 1\times10^{-4}\ \mathrm{m^2\ s^{-1}}$, respectively; we employ no-slip sidewalls and a free-slip bottom augmented by a linear bottom drag with coefficient $r = 3.5\times10^{-6}\ \mathrm{s^{-1}}$ applied over the bottom grid cell. Because of the coarse model resolution, baroclinic eddies are parameterized using the advective form of Gent & McWilliams (1990, hereafter GM) and Redi (1982) isopycnal mixing with equal mixing coefficients $K_{GM} = 500\ \mathrm{m^2\ s^{-1}}$. GM is implemented using the boundary value problem scheme of Ferrari *et al.* (2010) with vertical mode number $m = 2$ and minimum wavespeed $c_{\min} = 0.1\ \mathrm{m\ s^{-1}}$. The Redi tensor is tapered exponentially to horizontal diffusion in regions of weak stratification using the method of Danabasoglu & McWilliams (1995).

Tracers are advected using the second-order-moments (SOM) scheme of Prather (1986) and diffused using a vertical diffusivity, κ, which is surface intensified to mimic an

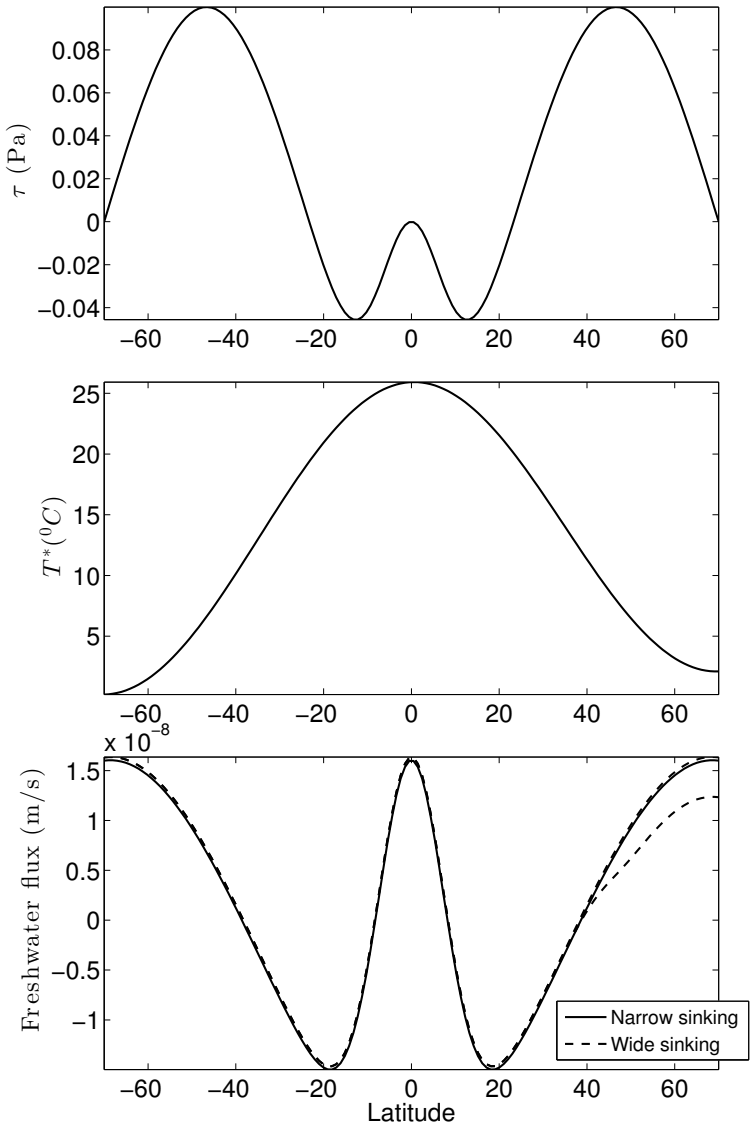

Figure 2.5: Forcing fields as a function of latitude: wind-stress (top), relaxation temperature (middle), freshwater flux (bottom). The dashed lines show the freshwater flux applied to induce a sinking in the wide basin. Where these lines split, the upper dashed line is applied to the narrow basin and the lower is applied to the wide basin.

idealized mixed layer such that

$$\kappa = \kappa_\nu + \kappa_m(1 + \tanh(z + d)/d)/2\,, \tag{2.11}$$

where $\kappa_\nu = 2 \times 10^{-5}\,\mathrm{m^2\,s^{-1}}$ is the diffusivity in the deep ocean, $\kappa_m = 10^{-2}\,\mathrm{m^2\,s^{-1}}$ is the diffusivity at the surface and $d = 20$ m is the characteristic depth of the mixed layer.

2.3.1 Residual overturning streamfunction

The overturning circulation is quantified using the zonally integrated residual overturning streamfunction (cf. Wolfe and Cessi, 2015)

$$\psi(y, \tilde{b}) \equiv \frac{1}{T}\int_0^T\int_0^{L_x}\int_{-H}^0 v^\dagger \mathcal{H}\left[b(x, y, z, t) - \tilde{b}\right]\,\mathrm{d}z\,\mathrm{d}x\,\mathrm{d}t, \tag{2.12}$$

where $T = 100$ years, $v^\dagger = v + v_{\mathrm{GM}}$ is the total meridional velocity (the sum of the resolved velocity v and the eddy velocity from the GM parameterization v_{GM}), and $\mathcal{H}$ is the Heaviside step function. ψ is the zonally integrated transport of water above the isopycnal $b(x, y, z, t) = \tilde{b}$. The "vertical" coordinate $\tilde{b}$ is buoyancy; the tilde distinguishes the coordinate "buoyancy" from the buoyancy field.

For presentation purposes, ψ is remapped into height coordinates using the mean isopycnal height

$$\zeta(y, \tilde{b}) \equiv -\frac{1}{T}\int_0^T \frac{1}{L_x}\int_0^{L_x}\int_{-H}^0 \mathcal{H}\left[b(x, y, z, t) - \tilde{b}\right]\,\mathrm{d}z\,\mathrm{d}x\,\mathrm{d}t. \tag{2.13}$$

In height coordinates, ψ advects a modified buoyancy $b^\sharp(y, z)$ that satisfies $\zeta\left[y, b^\sharp(y, z)\right] = z$; that is, ψ is constant on $b^\sharp$ contours for purely adiabatic flow.

Because of zonal buoyancy gradients, the remapping distorts the vertical extent of the mixed layer. Buoyancies higher than $40 \times 10^{-3}\,\mathrm{m\,s^{-2}}$ are not plotted because the contours

are too close together.

2.4 Pacific and Atlantic overturnings

With the forcing in figure 3.2, the model settles into a narrow-sinking state where sinking occurs at the northern end of the narrow basin. The resulting overturning circulation is shown in Figure 3.3 (colors and gray contours), together with $b^\sharp$ (black contours). The maximum ψ is 15 Sv near the northern end of the narrow basin and the interhemispheric circulation is quasi-adiabatic: the northward flow at intermediate depths follows isopycnals fairly well in the southern hemisphere, while the quasi-adiabatic residual flow in the northern hemisphere is augmented by a diffusively-driven positive cell. The circulation has the same pattern as estimates of observed transport for upper, intermediate and deep water (Talley *et al.*, 2011), but the transports from the model shown here are about 30% smaller than observed transports, because the maximum wind-stress in the southern hemisphere is about half of the value observed in nature, and the domain is only 210° wide. The deep overturning in the wide basin is characterized by two weak diffusively-driven counter-rotating cells each confined to a single hemisphere with maximum residual transport of about 6Sv.

We also force a wide-sinking circulation with sinking in the wide basin and upwelling in the narrow basin. This state is achieved by decreasing the freshwater flux in the Northern Hemisphere of the wide basin by about 0.06Sv, with a corresponding uniform increase elsewhere, until the circulation reverses (figure 2.7). Even though the active basin for wide sinking is twice as big as the active basin for narrow sinking, the amplitude of the ROC is about the same in the two cases, in agreement with the simple model described earlier. Once a new steady state is achieved, the freshwater flux can be brought back to the symmetric profile shown in figure 3.2, and eventually, in about 3000 years, the circulation reverts to sinking in the narrow basin.

In addition to the thickness weighted average fields as a function of latitude and

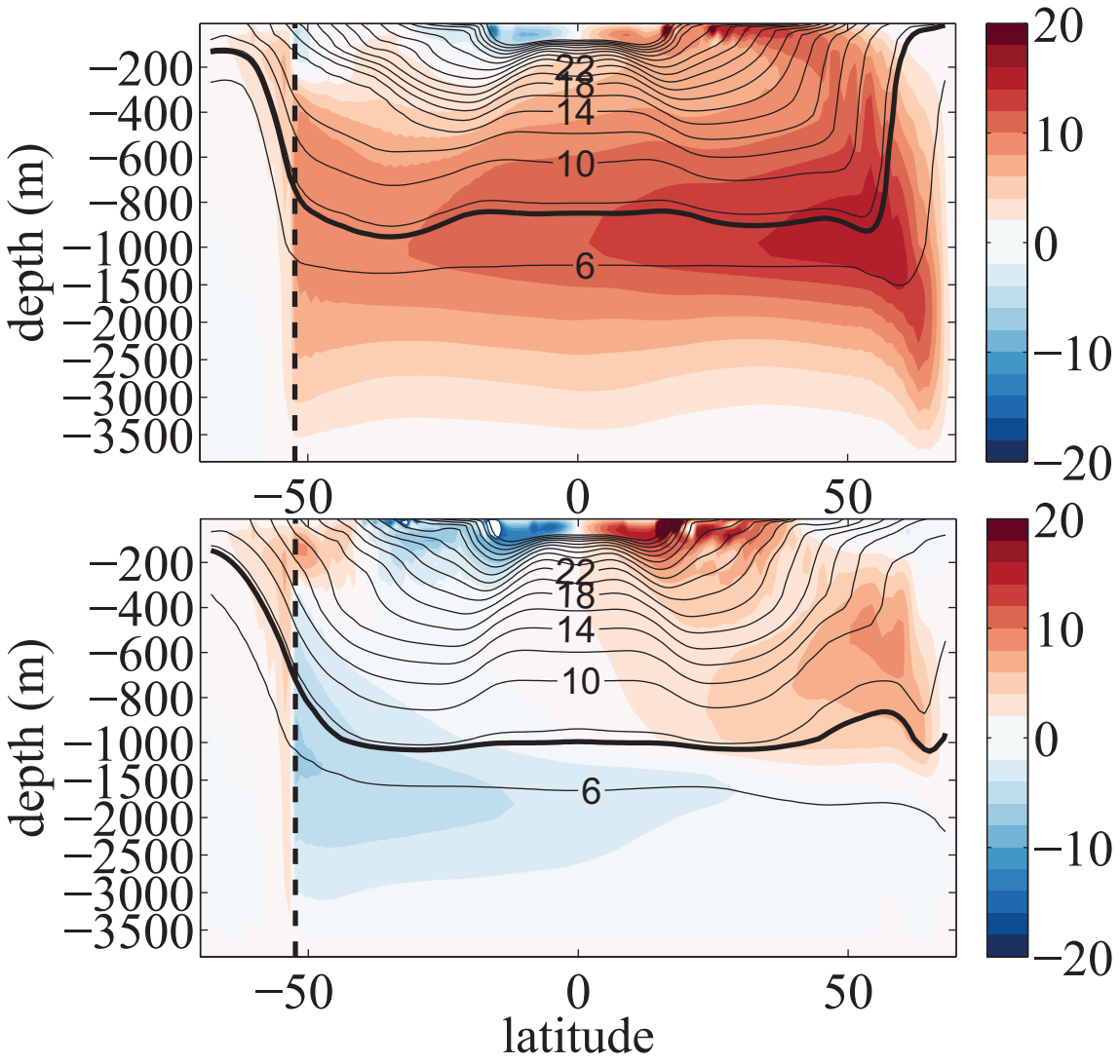

Figure 2.6: Residual overturning streamfunction in Sverdrups (color contours, interval 2Sv), and $b^\sharp \times 10^3\,\mathrm{m\,s^{-2}}$, the buoyancy of the surface whose average depth is z (black contours) in the narrow basin (top) and the wide basin (bottom). Sinking is in the narrow basin. In both plots, the re-entrant channel region (left of the thick black dotted line) shows the total stream function over all longitudes. The thick black contour denotes the isopycnal $b_m = 0.0076\,\mathrm{m\,s^{-2}}$ which bounds the upper branch of the ROC.

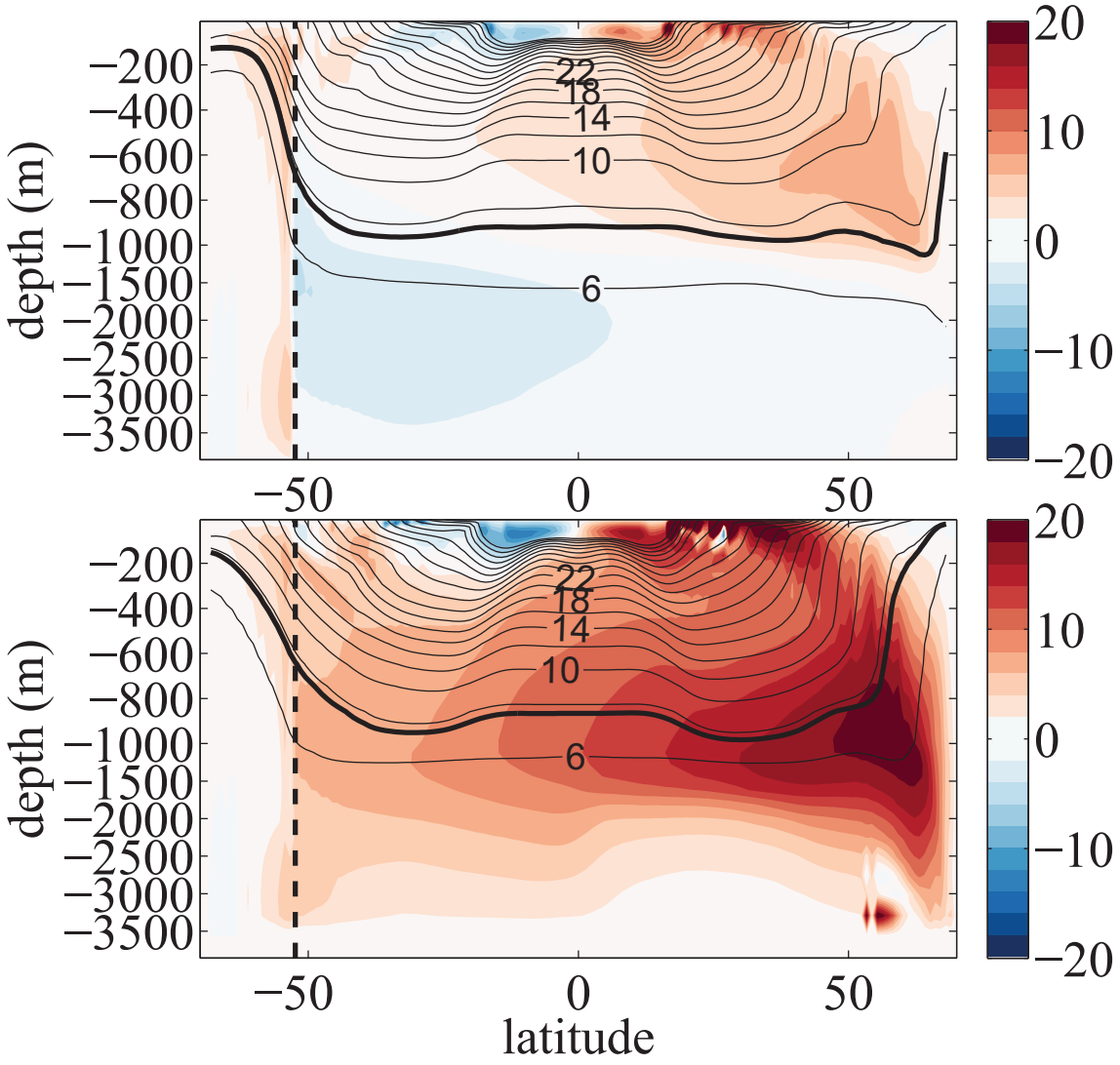

Figure 2.7: Residual overturning streamfunction in Sverdrups (color contours, interval 2Sv), and $b^\sharp \times 10^3\,\mathrm{m\,s^{-2}}$, the buoyancy of the surface whose average depth is z (black contours) in the narrow basin (top) and the wide basin (bottom). Sinking is in the wide basin. In both plots, the re-entrant channel region (left of the thick black dotted line) shows the total stream function over all longitudes. The thick black contour denotes the isopycnal $b_m = 0.0076\,\mathrm{m\,s^{-2}}$ which bounds the upper branch of the ROC.

buoyancy, we consider the cumulative transports above a given buoyancy surface, which are a good measure of the bulk transport by the upper branch of the overturning. The bounding buoyancy surface, b_m, is chosen to be $0.0076\,\mathrm{m\,s^{-2}}$: this choice captures most of the transport of the intermediate water cell, while avoiding the diffusive abyssal cell (which forms only small amounts of bottom water in this model). The zonally averaged position of this surface is shown by the thick black lines in figures 3.3 and 2.7, and its height as a function of latitude and longitude is shown in figure 2.8 for both narrow sinking (top panels) and wide sinking (bottom panels). It is clear that the isopycnals, especially at the eastern boundary, are shallower in the active basin. This is consistent with the results of the simple model (table 2.2), and with observations, which show that neutral density surfaces with maximum depths of around 1000m are deeper in the Indo-Pacific than in the Atlantic (figure 2.1).

In the channel, the barotropic flow has a wave-like structure that is asymmetric between basins. Therefore, to illustrate the transports in the narrow and wide sectors of the southern part of the domain, it is best to use a pseudo-streamwise horizontal coordinate system, which follows the barotropic streamlines, Ψ, near the channel edge and relaxes to latitude circles both near the southern boundary of the domain, and into the basin (32S is the latitude chosen). This tapering is necessary to avoid closed contours in the streamlines of Ψ, which would make the coordinate system unusable. Contours of the pseudo-streamwise coordinate system are shown in figure 2.9. This coordinate system allows us to visualize the across-stream transport in each sector by considering the divergence out of a volume bounded by an isopycnal and the surface in the vertical direction, by the southern boundary and a barotropic streamline in the meridional direction, by the longitudes of the western and eastern boundaries of the narrow and wide sectors in the zonal direction. To calculate the across-stream transport, it is easier and numerically more accurate to integrate the horizontal divergence of the vertically integrated velocity over a surface in the latitude longitude plane

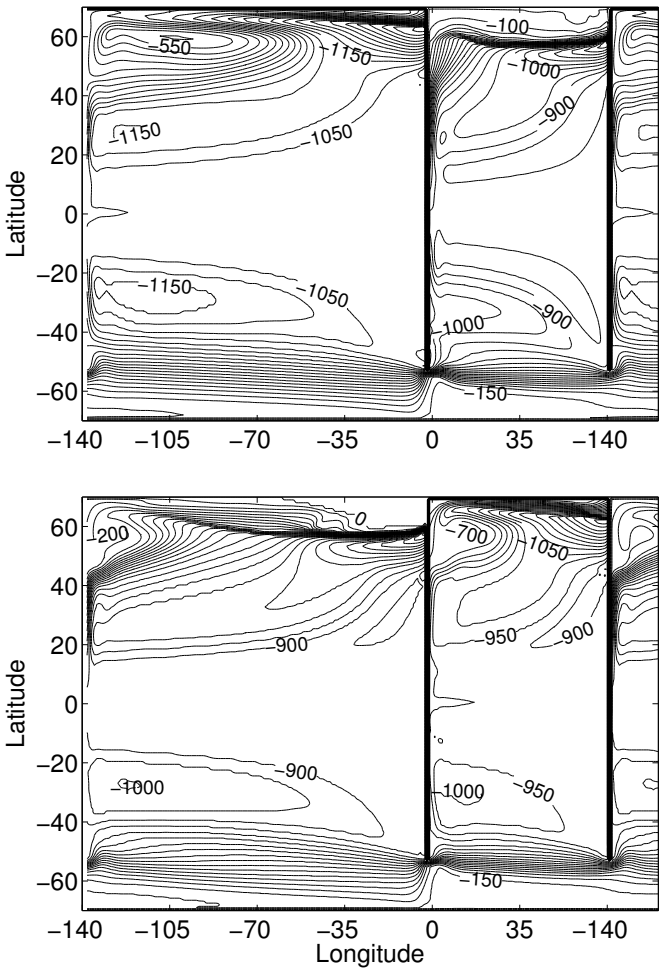

Figure 2.8: Contours of the height (m) of the isopycnal $b_m = 0.0076\,\mathrm{m\,s^{-2}}$ for narrow-basin sinking (top) (the thick black line in figure 3.3) and wide-basin sinking (bottom) (the thick black line in figure 2.7). The domain is 210°-periodic: the western 20° of the wide basin is repeated to the right of the figure. Contour interval is 50 m.

as shown in figure 2.9 and use Gauss's theorem. In order for vector calculus to be valid in this context, it is necessary to introduce a dual set of non-orthogonal unit vectors (Young,

2012) such that

$$\mathbf{e^1} = \hat{\mathbf{i}} \qquad \text{and} \qquad \mathbf{e^2} = \nabla\Psi \tag{2.14}$$

$$\mathbf{e_1} = \frac{\Psi_y\hat{\mathbf{i}} - \Psi_x\hat{\mathbf{j}}}{\Psi_y} \qquad \text{and} \qquad \mathbf{e_2} = \frac{\hat{\mathbf{j}}}{\Psi_y}\,. \tag{2.15}$$

The velocity divergence can then be calculated in the coordinate system most appropriate for the model's output and this gives the result:

$$\int_{A(\Psi)} \nabla\cdot\mathbf{u}\,\mathrm{d}A = \int_{C(\Psi)} \mathbf{u}\cdot\mathbf{e^2}\,dl - \int_{-L}^{y(\Psi)} \mathbf{u}\cdot\mathbf{e^1}\,dy\bigg|_{left} + \int_{-L}^{y(\Psi)} \mathbf{u}\cdot\mathbf{e^1}\,dy\bigg|_{right}\,. \tag{2.16}$$

where $\mathbf{u} = u^1\mathbf{e_1} + v^1\mathbf{e_2} = u\mathbf{i} + v\mathbf{j}$. The northward transport across the barotropic streamline segment $C(\Psi)$ is balanced by the zonal transport of the *east-west* velocity (and not the along-stream velocity), as well as the small diapycnal velocity associated with the area-integrated horizontal divergence.

The cross-stream transport is then taken to be the first term on the right hand side of (2.16) and is shown in figure 2.10, where the equivalent latitude is defined to span the same area enclosed by $A(\Psi)$ within each sector. North of 32S the meridional transport is plotted instead.

The transports shown in figure 2.10 can be interpreted in the context of the simple model. There is more diffusive upwelling in the wide basin than in the narrow basin and by volume conservation, $\left(\int\int_{-h}^{0} v\,dz\,dx\right)_y = \int w\,dx$, so the gradient of the lines in figure 2.10 is bigger for the wide basin than for the narrow basin. In the simple model, it is assumed that in the northern hemisphere of each basin, the diffusive upwelling north of the equator is balanced by buoyancy-driven sinking at the northern end of the basin. Therefore ψ_N for the MITgcm simulations should be measured at the equator. About 12Sv of transport crosses the equator in the active basin of both the narrow-sinking and wide-sinking states. Table 2.2 compares the results of the numerical study to the simple model described in section 2.

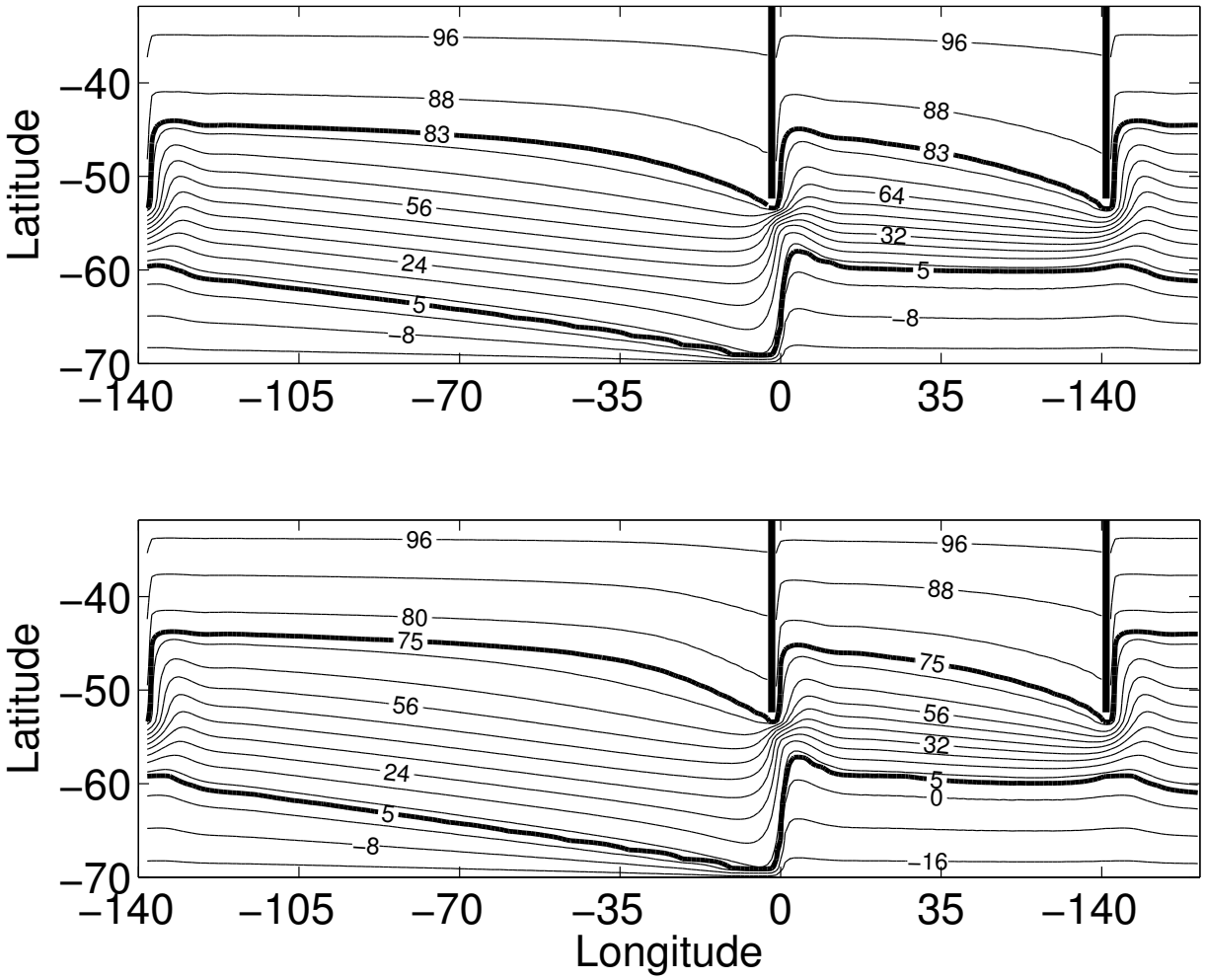

Figure 2.9: Contours of the pseudo-streamwise coordinate (Sv) used to evaluate the divergence of the residual velocity for narrow-basin sinking (top) and wide-basin sinking (bottom). The contours are constructed using the barotropic streamfunction between the thick contours, and tapered to latitude circles to the north and south of the displayed area. The domain is 210°-periodic: the western 20° of the wide basin is repeated to the right of the figure.

South of the edge of the semi-enclosed basin, the pressure and buoyancy is continuous in longitude. The difference in eastern boundary isopycnal heights at the southern edge of the basins leads to an east-west height difference within each basin. This difference is associated with the geostrophically balanced meridional transport ψ_g at the northern edge of the channel, which is out of the passive basin and into the active basin. At the latitude

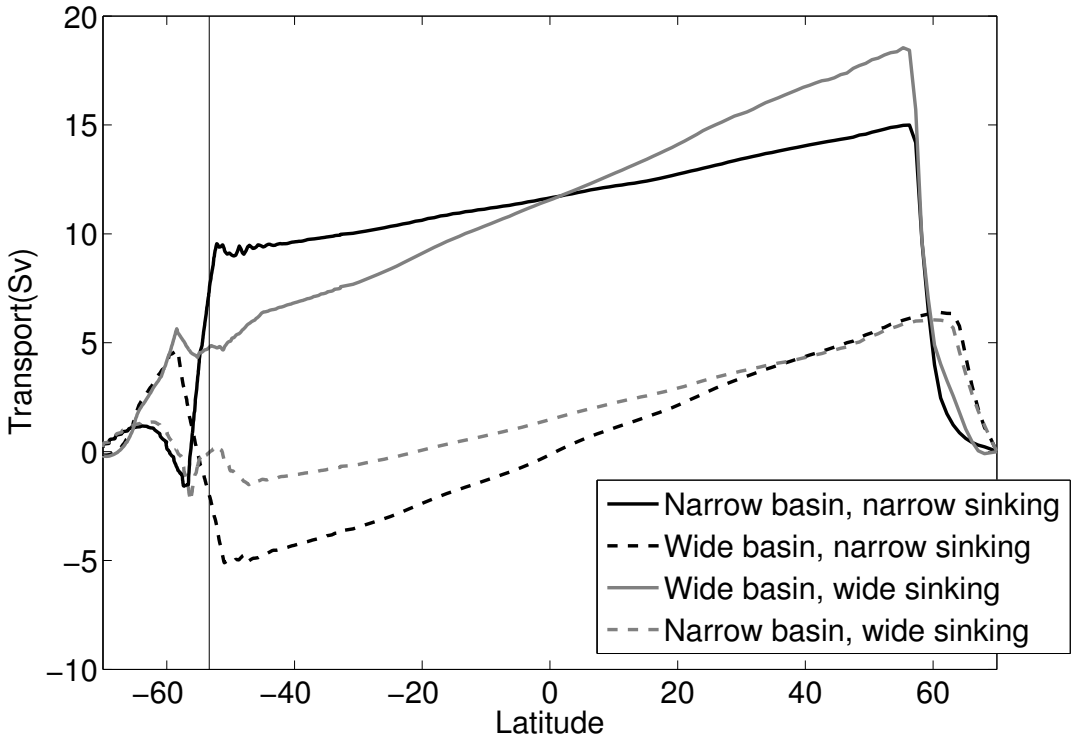

Figure 2.10: The zonally average thickness weighted meridional transports integrated above the isopycnal $b = 0.0076\,\mathrm{m\,s^{-2}}$ for narrow basin sinking (black lines) and wide basin sinking (grey lines). The thin vertical line denotes the northern edge of the circumpolar region.

where the continental boundaries terminate, the meridional exchange velocity turns from meridional to zonal in a narrow quasi-zonal jet connecting the two basins. The transport through 0E and 70E/140W is shown in figure 2.11. In both the narrow-sinking and wide-sinking states, the flow in the channel is westward, but there is a difference in transport between the eastern and western sides of the active basin, due to this quasi-zonal jet. The exchange flow ψ_g causes the transport on the western side of the active basin to be larger by 8.2Sv in the case of narrow sinking, but only 3.1Sv in the case of wide sinking.

There are three important differences between the narrow-sinking and wide-sinking states illustrated here: 1) Although the width of the wide basin is twice that of the narrow basin, the wide-sinking ROC is only slightly bigger than the narrow-sinking ROC (figure 2.10); 2) The net zonal inflow in the circumpolar region is from the wide to the narrow

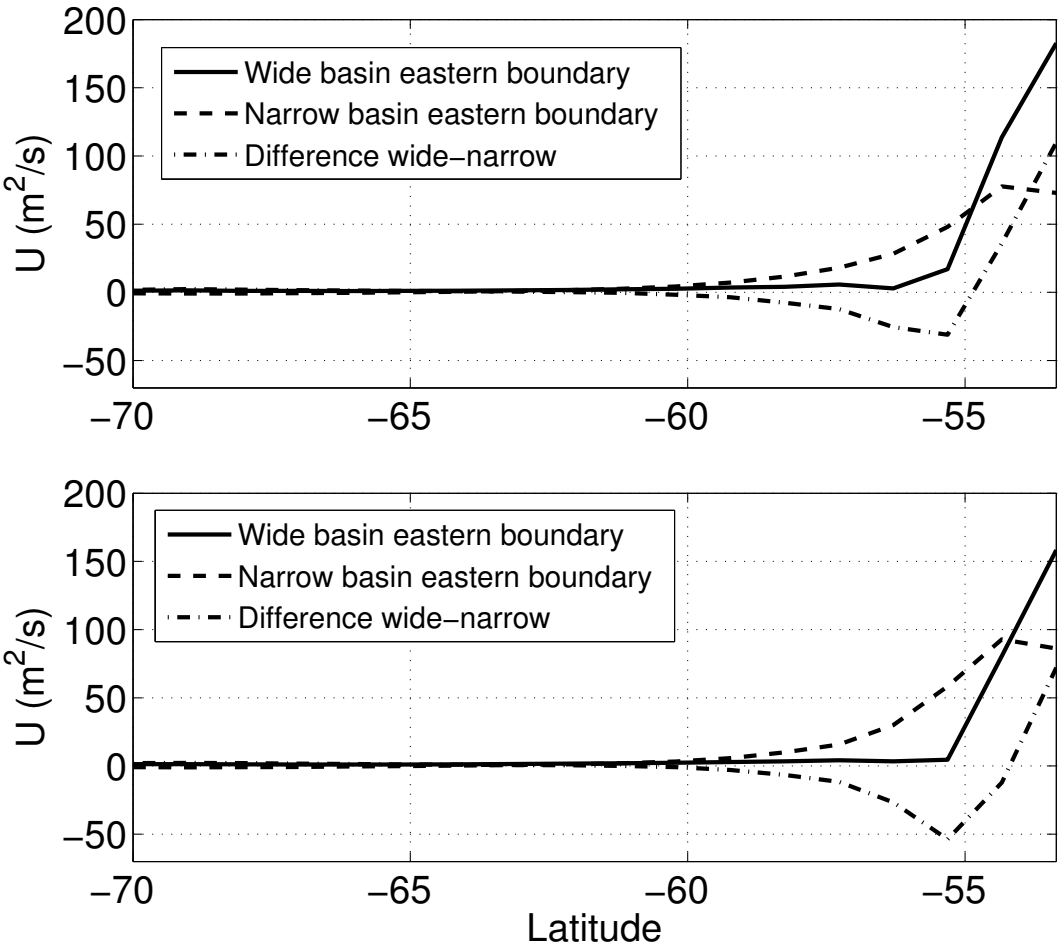

Figure 2.11: Zonal transport, U, integrated above the isopycnal $b = 0.0076\,\mathrm{m\,s^{-2}}$ at the eastern boundaries of the wide basin (solid line) and the narrow basin (dashed line) and their difference (dashed-dotted line) for narrow sinking (top) and wide sinking (bottom). The differenceintegrated across the whole channel in the Atlantic sinking case is 8.2Sv (top) and in the Pacific sinking case it is -3.1Sv (bottom).

basin in the narrow-sinking ROC and opposite in the wide-sinking ROC (cf. the difference between the zonal transport entering at the western boundary and the flow exiting at the eastern boundary in figure 2.11); 3) The net zonal flow exchanged between the two basins is *larger* for the narrow-sinking ROC. The difference in the zonal flows at the southern edges of the basins is associated with a change in the depths of isopycnals at the eastern boundaries: an example of this difference in depths is shown in figure 2.8.

2.5 Horizontal structure of the flow

The zonally averaged view of the upper branch of the ROC hides the rich zonal structure of the flow, which is strongly shaped by the wind-driven gyres. In figure 2.12, to visualize the horizontal distribution of the ROC, we contour the streamfunction associated with the zonal transport above the isopycnal b_m (shown by a thick line in figures 3.3 and 2.7). The streamfunction is obtained by integrating the vertically integrated zonal transport northward starting from the southern boundary of the domain. The flow is horizontally divergent due to diapycnal flow in the interior and in the outcrop regions, so not all of the ROC transport is captured. This view of the ROC clearly shows the exchange flow between the two basins, highlighted by thick contours in figure 2.12. The exchange flow exits the passive basin on the western boundary, immediately turns east in a narrow zonal jet and enters the active basin on the western boundary. From there, the wind-driven gyres induce large-scale meanders, modulating the meridional transport into alternating broad flows around the anti-clockwise gyres and narrow western boundary currents to the west of clockwise gyres. Finally the exchange flow sinks in the north-east sector of the active basin. Comparing narrow-basin sinking with wide-basin sinking is it clear that the exchange flow is less in the latter case, but the pathways are qualitatively similar.

To visualize all of the transport, including the horizontally divergent portion, figure 2.13 shows the contours of a pseudo-streamline, ϕ_d, constructed by adding the diapycnal contribution to the integrated zonal transport, that is

$$\phi_d = -\int_{-L}^{y} d\hat{y} \left[U(x,\hat{y}) - \int_0^x d\hat{x}\, \varpi(\hat{x},\hat{y}) \right] , \tag{2.17}$$

where U is the zonal transport above the isopycnal b_m, and ϖ is the diapycnal velocity across the same isopycnal. This construction gives some apparent flow through the solid boundaries, but it has the advantage of illustrating the contribution of all the components of

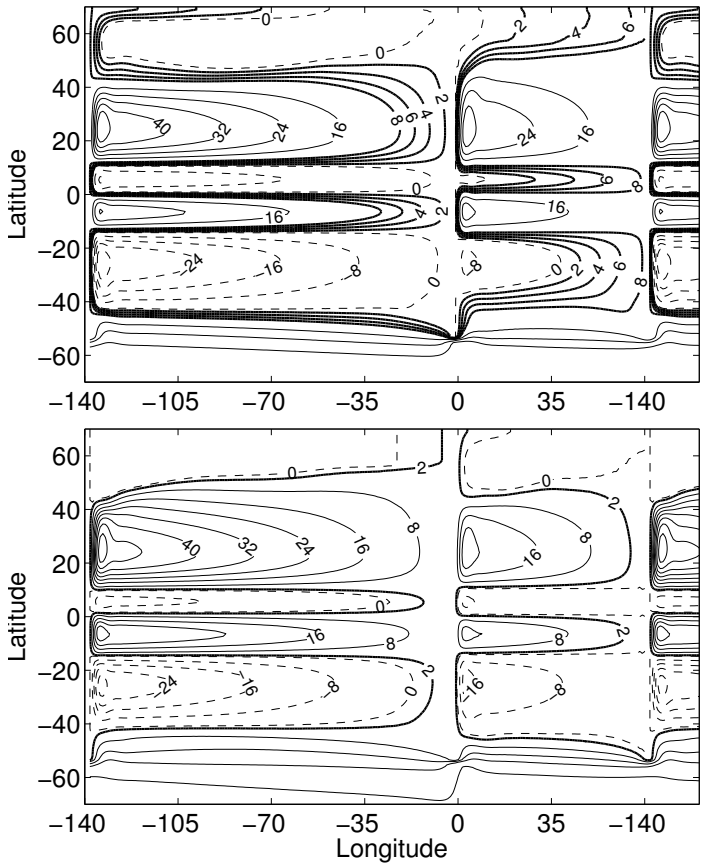

Figure 2.12: Streamlines of the transport (Sv) above $b_m = 0.0076\,\mathrm{m\,s^{-2}}$ for narrow-basin sinking (top) and wide-basin sinking (bottom). The streamlines are constructed by integrating the thickness weighted zonal flow in latitude. The contour interval is 8Sv for the thin lines and 2Sv for the thick lines, which denote the interbasin exchange flow. Negative streamlines are dashed. The domain is 210°-periodic: the western 20° of the wide basin is repeated to the right of the figure.

the ROC. In particular it shows that the ROC in the active basin is primarily connected to the diffusive overturning in the southern hemisphere of the active basin, while the northern hemisphere of the passive basin does not participate in the upper branch, in accordance with the zonally averaged view of figures 3.3 and 2.7. In both views of the flow, the meridional "throughflow" velocity in the regions of anti-clockwise circulation is larger for narrow-basin sinking.

To characterize the lower branch of the ROC, a streamfunction is constructed by integrating the zonal transport between b_m and the bottom. The streamlines thus obtained

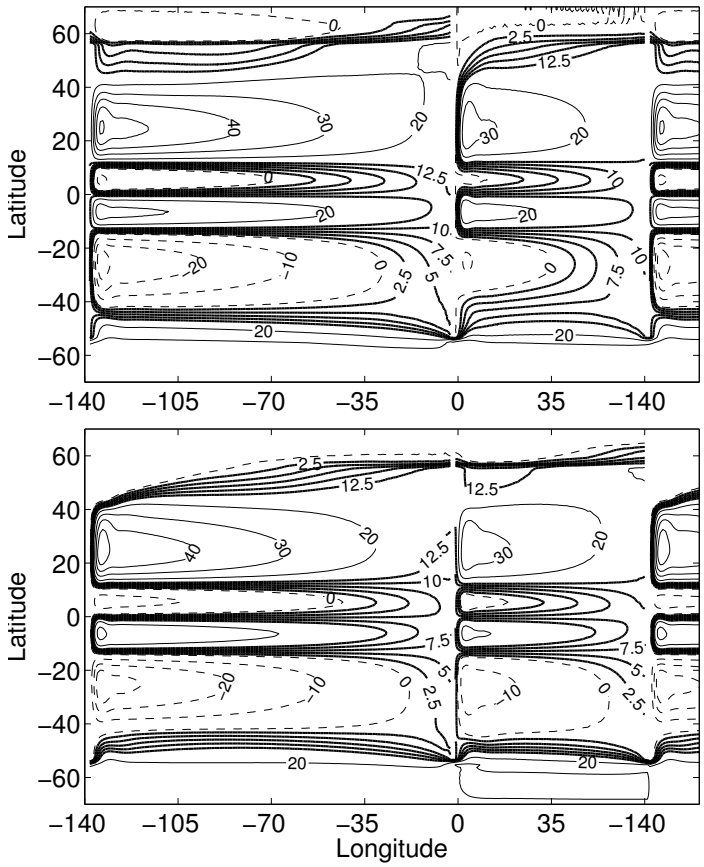

Figure 2.13: Isolines of ϕ_d defined in (2.17) (Sv) for narrow-basin sinking (top) and wide-basin sinking (bottom). The contour interval is 10 Sv for the thin lines and 2.5Sv for the thick lines, which denote the interbasin exchange flow. Negative values of ϕ_d are dashed. The domain is 210°-periodic: the western 20° of the wide basin is repeated to the right of the figure.

are shown in figure 2.14. In the active basin the exchange flow is almost entirely confined to the western boundary, except at the southern boundary of the basin, where it turns into a quasi-zonal flow before entering the passive basin at the eastern boundary, and at the boundary between the subpolar and subtropical gyres, where excursions in the interior occur, as observed by Bower *et al.* (2009). The interior flow in the active basin is a mixture of the classical Stommel-Arons poleward flow, modified by the wind-driven gyres, more prominently so in the wide basin, where the wind-gyres are stronger. The view of the return flow of the ROC offered by ϕ_d (not shown), defined in (2.17), shows that the meridional connection

between the two basins does not extend to the northern hemisphere of the passive basin, as already seen in figures 3.3, 2.7 and 2.13.

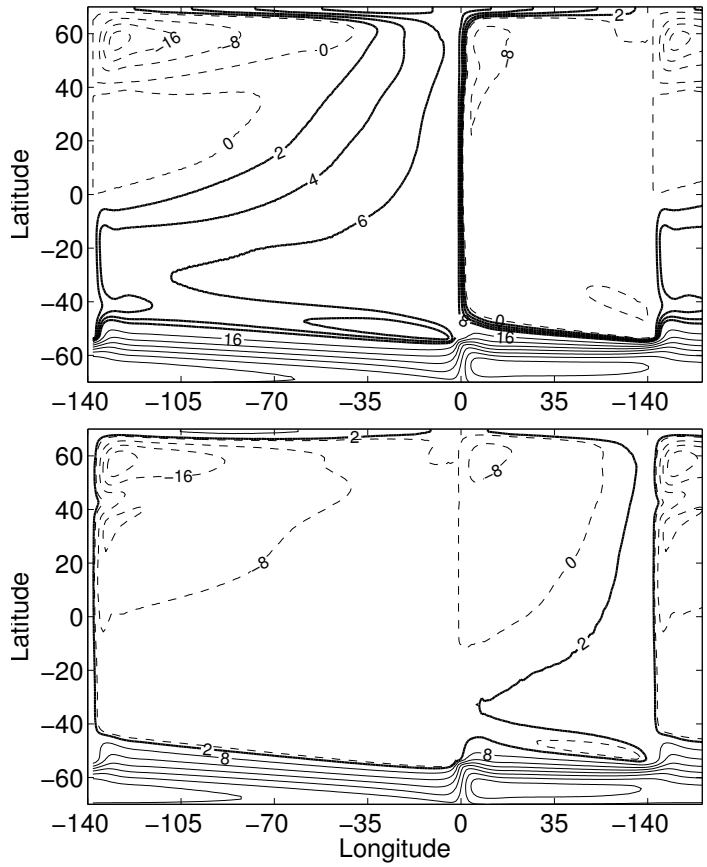

Figure 2.14: Streamlines of the transport (Sv) between $b = 0.0076\,\mathrm{m\,s^{-2}}$ and the bottom for narrow-basin sinking (top) and wide-basin sinking (bottom). The streamline are constructed by integrating the thickness weighted zonal flow in latitude. The contour interval is 8 Sv for the thin lines and 2Sv for the thick lines, which denote the interbasin exchange flow. Negative streamlines are dashed.

Finally, the three dimensional structure of the ROC can be partially visualized using particle trajectories. Figure 2.15 shows the paths of particles that are initialized at the surface at the northern edge of the channel in the passive sector. The particle trajectories shown are chosen to highlight the path of the Ekman transport ψ^p_{Ek} as it enters the passive basin, turns, and becomes the interbasin flow ψ_g which flows around the continental boundary and into the active basin. The particles initially move northward in the Ekman layer, then are subducted

in the passive basin, getting caught in both the tropical and subtropical gyres. The particles do not cross the equator in the passive basin, but move approximately adiabatically into the active basin. There, they go northward until they sink in the north-east part of the sub polar gyre. The transit-time from entering the active basin to the sinking location is highly dependent on particle initialization: particle transit-time varies with the depth of the particle and with the number of times it goes around in the gyres. In figure 2.15, the transit-time from the channel to the sinking location is 125yrs for the narrow sinking case and about 175yrs for the wide sinking case.

2.6 Conclusions

In a two-basin simplified configuration of the world ocean, with one wide and one narrow basin connected by a re-entrant channel, the meridional overturning circulation prefers a state with sinking at the northern edge of the narrow basin balanced by upwelling elsewhere. The salt-advection feedback reinforces this preference. A wide-sinking circulation with sinking at the northern edge of the wide basin can be coerced by imposing reduced freshwater flux in this region, but this state is unstable to forcing that is zonally symmetric. The exchange flow between the basins is maximized in the narrow-basin sinking state, leading to a larger average depth of intermediate isopycnals in the passive versus the active basin. This difference in isopycnal depths between basins results in a higher sea surface height in the passive basin compared to the active basin.

The total residual transport is essentially fixed by the strength of the wind-stress and the eddies in the ACC, and by the diapycnal upwelling into the upper branch of the ROC. These quantities are approximately independent of the location of the sinking: if sinking were to occur in the North Pacific rather than the North Atlantic, the strength of the ROC transport would be about the same, even though the Indo-Pacific is much larger than the Atlantic. Consequently, the transport per unit width, or the typical meridional

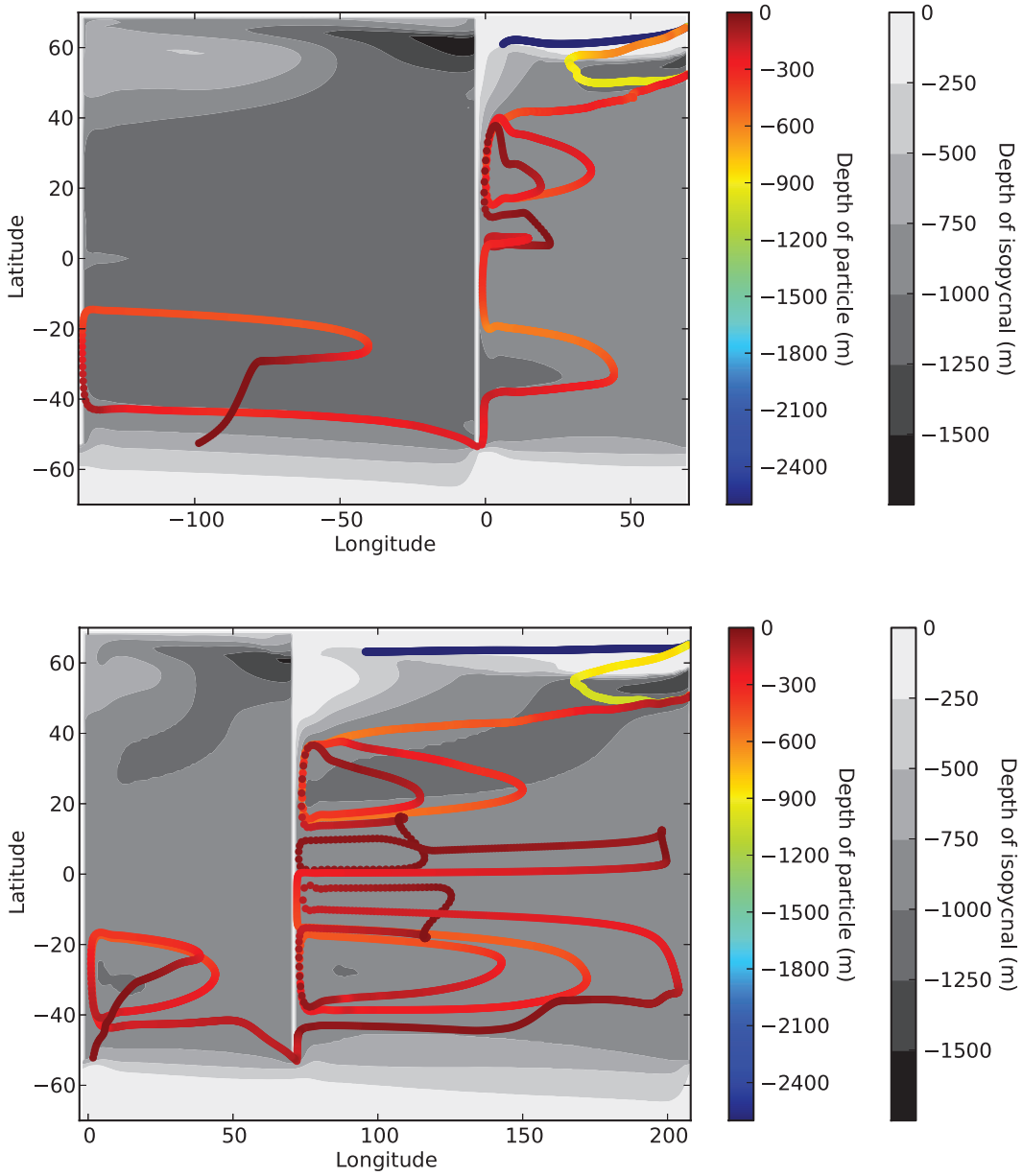

Figure 2.15: The depth (m) of the isopycnal $b_m = 0.0076\,\mathrm{m^2\,s^{-1}}$ is plotted in greyscale for narrow sinking (top) and wide sinking (bottom). This isopycnal divides the upper branch of the ROC from the lower branch. The location of the trajectory of a particle is shown in rainbow colors, with one point plotted every 14 days, and the color indicates particle depth (m). The active basin is plotted on the left in both cases, so that a continuous particle track is visible. The particles are initialized at the surface and at the northern edge of the channel in the passive sector. Trajectories that pass first into the passive basin and then into the active basin are chosen. The domain is 210°-periodic.

velocity associated with the upper (and lower) branch of the ROC would be smaller for North Pacific sinking compared to North Atlantic sinking, unless the meridional transport is all concentrated in a narrow boundary current.

The approximate independence of the ROC transport on the sinking location implies that the through-flow velocity is faster when sinking occurs in the narrow basin. In addition, a plan view of the upper branch of the overturning circulation reveals that the northward path of the ROC "snakes" around the gyres. When passing clockwise gyres, the overturning streamlines follow the western boundary, and so the velocity on these streamlines is high and there is little time for exchange of salinity with the atmosphere. When passing anti-clockwise gyres, the streamlines move to the eastern side of the gyre and the flow is slower so there is more time for exchange of salinity with the atmosphere. The complexities of the three dimensional circulation may be important in setting the distribution of tracers, especially salinity, which strongly controls the range of surface buoyancy shared between the sinking region and the upwelling region in the circumpolar current. Maximizing this range of shared buoyancies allows efficient adiabatic transport along the isopycnals connecting the two hemispheres. Further analysis of the implications of this flow field to tracer transport is deferred to a subsequent study.

Acknowledgements

CSJ and PC are supported by the National Science Foundation under Grant No. OCE-1258887 and the Office of Science (BER), U.S. Department of Energy, under Grant No. DE-SC0005100. Computational resources were provided by XSEDE consortium, which is supported by National Science Foundation Grant ACI-1053575. Thanks go to Jinbo Wang, who contributed the particle trajectory code, and to David Marshall and Johan Nilsson for their helpful reviews.

Chapter 2, in full, is a reprint of the material as it appears in the Journal of Physical

Oceanography 2016. Jones, C. S.; Cessi, Paola, American Meteorological Society, 2016.

Chapter 3

Size matters: another reason why the Atlantic is saltier than the Pacific

3.1 Introduction

In the current climate system, deep water is formed in the North Atlantic, but not in the North Pacific, resulting in a meridional overturning circulation (MOC) that transports heat northward everywhere in the Atlantic. Deep-water formation in the North Pacific is prevented by fresh, buoyant surface waters, much fresher than surface waters at comparable latitudes in the Atlantic (Warren, 1983; Broecker, 1991), with the salinity component dominating over the temperature component (the colder and fresher North Pacific surface water is lighter than the warmer and saltier North Atlantic surface water). Several reasons have been advanced for the salinity difference between the Atlantic and the Pacific [see Weaver *et al.* (1999) for a review].

The flux of fresh water into the atmosphere from the ocean may be expressed as the evaporation-minus-precipitation rate per unit area ($E - P$). Craig *et al.* (2016) show that $E - P$, integrated over each basin north of 35S, is greater in the Atlantic than in the Pacific by 0.4 Sv: the net $E - P$ out of the Atlantic is about 0.4 Sv and approximately zero out of

the Pacific. Several mechanisms contribute to the difference in $E - P$ between oceans, some involving the atmosphere alone, and others involving the ocean circulation. The North Pacific experiences slightly higher precipitation because of the more effective orographic blockage of moist air in the Pacific sector (Broecker *et al.*, 1990; Schmittner *et al.*, 2011). However, Kamphuis *et al.* (2011) show that Atlantic sinking still occurs on a retrograde-rotating earth, where the direction of the winds across the American continent are reversed. This implies that the orographic blockage of moisture transport by the American continent alone does not set the location of deep-water formation. The northward transport of moisture by the Asian monsoon (Geay *et al.*, 2003) in the Pacific sector may contribute to the higher precipitation in the north of that basin, suppressing local sinking. The precipitation footprint of water evaporating from the narrow Atlantic basin extends into the wider Pacific basin, while most of the water evaporating from the Pacific precipitates in the same sector (Ferreira *et al.*, 2010; Wills & Schneider, 2015). In addition, a larger fraction of the area of the Atlantic is exposed to dry air coming off the continents, which may also increase evaporation over the Atlantic (Schmitt *et al.*, 1989).

Some of the geographical differences between the two ocean basins are thought to favor deep water formation in the North Atlantic. Most obviously, the Atlantic extends farther north than the Pacific, and it is more connected to the Arctic, where cold dense water is formed during winter (Warren, 1983). Mixing with the outflow from the Mediterranean Sea(a semi-enclosed basin with net evaporation) may increase the salinity of the northward branch of the MOC (Reid, 1979; Warren, 1981), although the importance of this process has been questioned (McCartney & Mauritzen, 2001; Talley, 2008). The larger width of the Pacific, and associated stronger wind-driven circulation and east-west temperature contrasts, may produce a larger poleward heat transport by the gyres in the Pacific relative to the Atlantic, removing the need for a MOC-mediated heat transport (Wang *et al.*, 1995). The lower-latitude position of the tip of South Africa relative to the tip of South America is a

favorable configuration for transporting high-salinity water from the Indo-Pacific sector into the Atlantic (Reid, 1961; Gordon *et al.*, 1987; Cessi & Jones, 2017). Finally, the surface branch of the MOC advects higher salinity waters from the subtropics to the high latitudes, further enhancing the salinity in the North Atlantic relative to the North Pacific. This process is termed "the salt-advection feedback" (Stommel, 1961).

At least some of the explanations for a saltier Atlantic rely on the Atlantic meridional overturning circulation (AMOC), which is itself enabled by increased salinity in the North Atlantic. Salt- (and heat-) advection feedbacks act to maintain the MOC and higher salinity (and temperature) in the region where the deep-water formation takes place. Higher temperatures decrease the surface density and thus tend to reduce the overturning rate, i.e. a negative feedback. Higher salinities increase the surface density and thus directly increase the overturning rate, while higher temperature tends to decrease the overturning rate. In principle, the salt-advection feedback could act to produce deep overturning in the Pacific (PMOC), rather than in the Atlantic. However, both coupled (Ferreira *et al.*, 2010; Nilsson *et al.*, 2013) and ocean-only idealized models (Stocker *et al.*, 1992; Hughes & Weaver, 1994) show a preference for sinking in the narrower basin. Huisman *et al.* (2012) even find that Atlantic sinking occurs when $E - P$ is higher in the Pacific than in the Atlantic, indicating that the oceanic transport of salt controls the location of sinking.

It is important to understand the reasons why the Atlantic is saltier than the Pacific, in order to predict the fate of the MOC under global climate change. The Atlantic salinity is determined by the transport of fresh water both by the atmosphere (through $E - P$) and by the ocean, and the relative importance of each is unclear. Even if atmospheric transport were the most important factor today, this may change in the future due to greenhouse gas forcing (Seager *et al.*, 2010, 2014). Our work will be useful in understanding future climates, and may elucidate the role of the MOC in past climates, when the distribution of $E - P$ was different from today (Hewitt *et al.*, 2003).

In this study, we focus on one of the more obvious asymmetries between the Atlantic and the Pacific: the difference in basin widths. Specifically, we examine the consequences of this geometrical asymmetry on the oceanic flow and its repercussions on the salinity distribution. The impacts of atmosphere-only processes or atmosphere-ocean feedbacks on the asymmetry in salinity distribution between the basins have been examined using ocean-atmosphere models (e.g. Ferreira *et al.* (2010); Nilsson *et al.* (2013)). These processes are excluded here by applying fixed surface forcings.

Few studies on the location of deep-water formation have considered the role of the wind-driven gyres. Warren (1983) attributes low salinities in the North Pacific to the small rate of northward flow between the subtropical and subpolar gyres, but he does not consider a scenario with deep-water formation in the North Pacific. Observations show a salinity increase in the North Atlantic correlated with a decreased strength of the subpolar gyre (SPG) during the period from 1965 to 2003 (Hátún *et al.*, 2005; Häkkinen & Rhines, 2004).

In this study, we advanced an additional mechanism for why the AMOC is preferred to the PMOC, based on the relative strengths of the western boundary currents associated with the MOC and with the SPG in the basin where sinking occurs. An important result relevant for this work is that the transport of the MOC is essentially independent of the sinking location (Jones & Cessi, 2016). This is because the MOC transport is determined by three sources – the northward Ekman transport entering the basins from the Southern Ocean, minus the southward eddy-thickness transport exiting the same region, plus the global diapycnal upwelling into the upper branch of the MOC. All these sources add up to the total sinking, regardless of its location.

Upon entering the sinking basin, the northward flow of the upper branch of the MOC forms a western boundary current, with a velocity that is independent of the sinking location. This western boundary current is superimposed on the western boundary current associated with the wind-driven gyres. Although the Sverdrup interior meridional velocity in the SPG

is the same in both basins, for zonally uniform winds, the western boundary current and the gyre's zonal velocity are faster in a wider basin. In the simplified geometry presented here, the MOC northward velocity is larger than the southward SPG western boundary current in the narrow basin (with width similar to the Atlantic), but not in the wide basin (with width similar to the Pacific). The net result is that salty water from the subtropical gyre is carried into the western portion of the SPG when sinking occurs in the narrow basin, but not when sinking occurs in the wide basin. Instead, in the wide basin, the southward western boundary current in the SPG brings fresh water from the far north, where the freshwater flux is maximum. The resulting fresh pool suppresses local deep-water formation and the faster zonal velocity efficiently spreads the freshwater eastward, causing the water in the SPG of the wide basin to become fresher than the water in the SPG of the narrow basin. This process, diagnosed in the 3-D model experiments, is documented in section 3.2.

In section 3.3, a 2-D advection-diffusion model of the upper branch of the MOC is used to explore the salinity distribution for various flow fields and zonal arrangements of deep water formation. Further idealized experiments with the same 2-D model show that neither the MOC western boundary current alone nor the wind-driven gyres alone can produce different salinity fields based on the basin width. However, salt advection by the combined velocity fields, and the associated feedback on deep water formation, select the narrow basin as the preferred deep water mass formation site. Section 3.4 provides a summary and draws conclusions.

3.2 3-D model and diagnostics

We use a 3-D primitive-equation version of the MITgcm. The domain consists of two boxes of different widths connected by a re-entrant channel occupying the southernmost 17.5° of latitude (figure 3.1). The bottom of the basin is flat and 4000m deep, except for a sill in the periodic channel, one-grid point wide and 1333m high, located immediately south of

the narrow basin's western boundary.[1] The continents that separate the basins are one-grid point wide and have the same length, extending from $-52.5°$ to $70°$. The equation of state is linear, with the buoyancy described by:

$$b = g\left[\alpha_T T - \beta_S (S - S_{ref})\right] , \tag{3.1}$$

where $\alpha_T = 2 \times 10^{-4}\,°\mathrm{C}^{-1}$, $\beta_S = 7.4 \times 10^{-4}$ and $S_{ref} = 35$. Salinity is given on the practical salinity scale and is therefore presented without units. Temperature is in Celsius.

The model is forced at the surface by zonally-uniform wind stress, τ, freshwater flux, F, and temperature relaxation to a profile, T^*, given by

$$\tau = \tau_{Max}\left(-\cos(3\pi\theta/140) + e^{-\theta^2/\sigma^2}\right) , \tag{3.2}$$

$$F = F_s\left(\cos(7\pi\theta/8\Theta) - 2e^{-(\theta/\Theta).^2/(2\sigma_F^2)}\right) - F_0 , \tag{3.3}$$

$$T^* = T_{eq}\left(\cos(\pi\theta/140)^2 + 0.1e^{-(\theta/2\Theta - 1)^2}\right) , \tag{3.4}$$

where θ is latitude in degrees, $\tau_{Max} = 0.1\,\mathrm{N m^{-2}}$, $\sigma = 10°$, $F_s = 2 \times 10^{-8}\,\mathrm{m\,s^{-1}}$, $\sigma_F = 0.128$, $\Theta = 60°$ and $T_{eq} = 25°\mathrm{C}$ (see figure 3.2). The relaxation time-scale for the surface temperature is 10 days. The constant F_0 is chosen so that the net freshwater flux into the ocean is zero. The freshwater flux is multiplied by the negative reference salinity $-S_{ref}$ in order to obtain the salinity flux into the ocean.

Baroclinic eddies are parameterized using the Gent-McWilliams advective form (Gent & McWilliams, 1990) and Redi (1982) isopycnal tracer mixing with equal mixing coefficients $\kappa_{GM} = 500\ \mathrm{m^2\ s^{-1}}$. The Gent-McWilliams scheme (GM henceforth) is implemented using the boundary value problem framework described by Ferrari *et al.* (2010). The Redi tensor is tapered to horizontal diffusion in regions of weak stratification, as described by Danabasoglu

[1]The W2N experiment described here was repeated with sills at the end of both of the continents and this lead to no qualitative changes to the overturning.

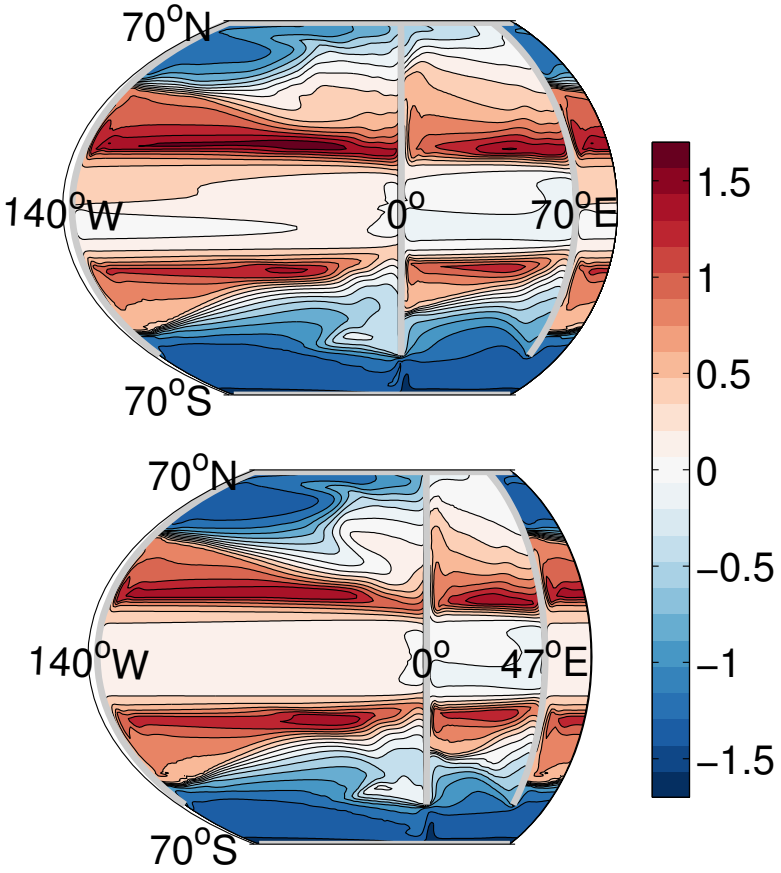

Figure 3.1: Surface salinity anomaly, referenced to 35 PSU, for zonally symmetric surface forcing in the W2N geometry (top) and the W3N geometry (bottom). Thick grey lines represent boundaries. Contours are every 0.2 PSU. The domain is periodic and the western 20 degrees of the domain are repeated to the right of the figure.

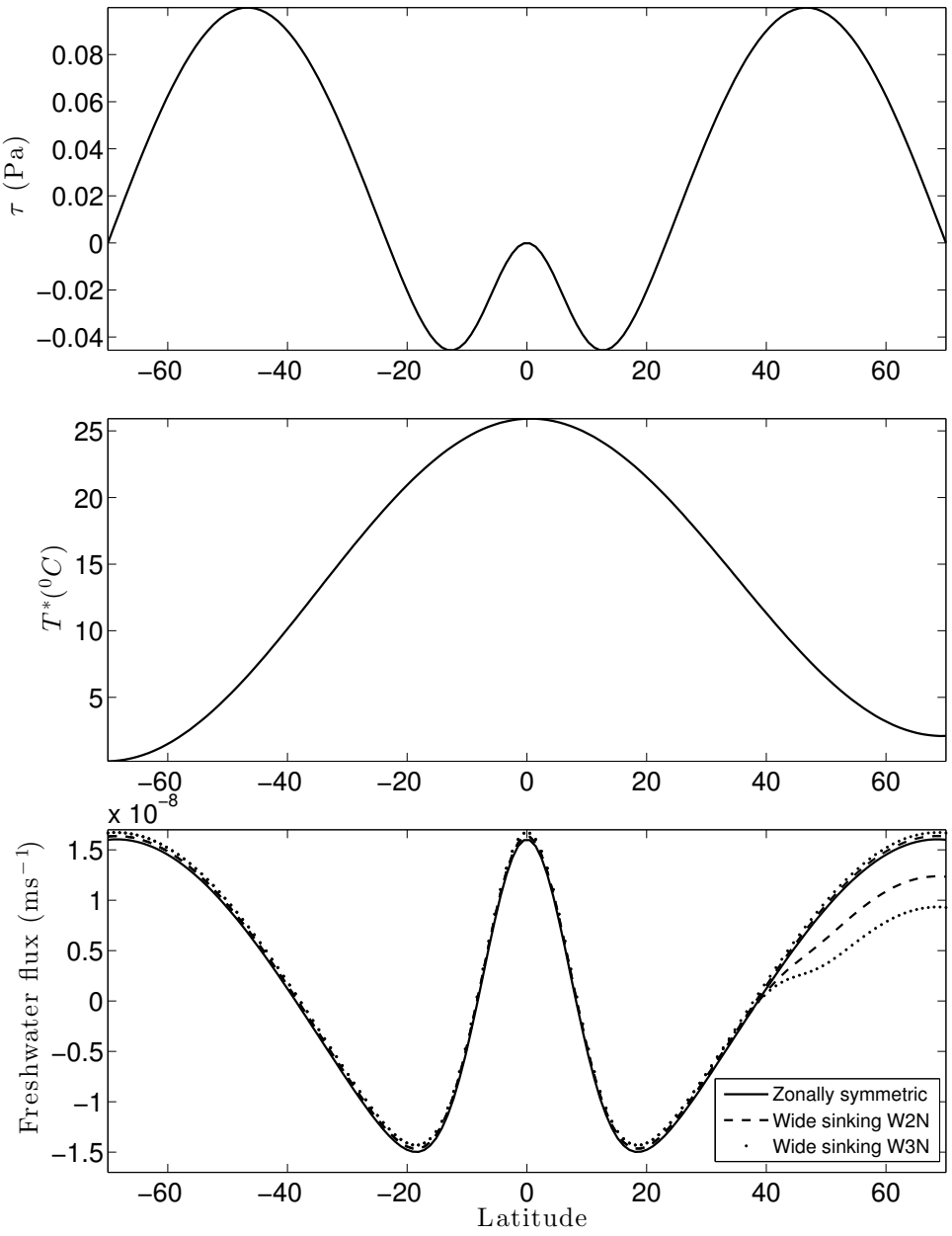

Figure 3.2: Surface wind stress in Pa (top), the profile of temperature used for temperature relaxation in °C (middle) and surface freshwater flux forcing in $\mathrm{m\,s^{-1}}$ (bottom) . The dashed lines show the freshwater flux used to induce sinking in the wide basin in the W2N geometry and the dotted lines show the freshwater flux used to induce sinking in the wide basin in the W3N geometry. Where these lines split, the upper dashed/dotted line is applied to the narrow basin and the lower one is applied to the wide basin. For wide sinking, the wide-basin freshwater flux is reduced by 0.06 Sv in the W2N geometry and by 0.1 Sv in the W3N geometry.

& McWilliams (1995). The vertical diffusivity is set to $2\times10^{-5}\,\mathrm{m^2\,s^{-1}}$ in the interior, tapering to $10^{-2}\,\mathrm{m^2\,s^{-1}}$ at the surface over a depth of 20m to model the mixed layer. Each simulation was run for at least 3000 years, until equilibrium was reached. Additional details of the model configuration are given in Jones & Cessi (2016).

Two configurations are considered in the 3-D model: one in which the wide basin is twice as wide as the narrow basin (W2N), and one in which the wide basin is three times as wide as the narrow basin (W3N). These geometries are shown in figure 2.4, together with the surface salinity obtained under zonally uniform surface forcing: in both geometries, the wide basin is 140° wide, with the narrow basin 70° wide for W2N, and 47° wide for W3N. Under zonally uniform forcing, deep water formation occurs in the narrow basin only, regardless of the initial condition, and the surface salinity in the SPG of the narrow basin is higher for W3N than for W2N.

Sinking in the wide basin can be coerced by reducing the freshwater flux at the northern end of the wide-basin sector, while compensating this reduction by a uniform freshwater flux increase everywhere else. A larger asymmetry in fresh water flux is needed to force wide sinking in the W3N geometry than in the W2N geometry (see the bottom panel of figure 3.2), suggesting that the larger the ratio of basin widths, the greater the preference for narrow sinking. For both W2N and W3N, the wide sinking state reverts to narrow sinking when the forcing is slowly (over 20000 years) returned to zonal symmetry. In summary, wide sinking is unstable under zonally-uniform freshwater forcing.

We frame the discussion of the meridional transport in terms of the residual overturning circulation (ROC), rather than the eulerian circulation. The ROC is defined as the time and zonally-averaged meridional transport *at constant buoyancy*, rather than at fixed depth levels. Thus it measures the transport of buoyancy, rather than the transport of volume. The ROC is more representative of the transport of tracers than the eulerian transport (Andrews

& McIntyre, 1978). The ROC streamfunction is defined as

$$\psi(y,\tilde{b}) \equiv \frac{1}{T}\int_0^T\int_0^{L_x}\int_{-H}^0 v\mathcal{H}\left[b(x,y,z,t)-\tilde{b}\right]\,\mathrm{d}z\,\mathrm{d}x\,\mathrm{d}t\,, \tag{3.5}$$

where v is the Eulerian plus parameterized eddy velocity, H is the total depth, L_x is the width of the basin, T is the averaging timescale (100yrs is chosen here) and $\mathcal{H}$ is the Heaviside function. ψ is the zonally integrated transport of water above $b=\tilde{b}$. In figures 3.3 and 3.4 (filled color contours), the ROC streamfunction is remapped into z-coordinates using the zonal-mean isopycnal height, which is defined as

$$\mathcal{Z}(y,\tilde{b}) \equiv -\frac{1}{T}\int_0^T\frac{1}{L_x}\int_0^{L_x}\int_{-H}^0 \mathcal{H}\left[b(x,y,z,t)-\tilde{b}\right]\,\mathrm{d}z\,\mathrm{d}x\,\mathrm{d}t. \tag{3.6}$$

In z-coordinates, it is useful to define the modified buoyancy $b^\sharp(y,z)$ where $\mathcal{Z}\left[y,b^\sharp(y,z)\right]=z$. The field $b^\sharp$ is advected by the ROC streamfunction ψ, and thus ψ is constant on $b^\sharp$ contours for adiabatic flow. In figures 3.3 and 3.4, contours of $b^\sharp$ show the stratification: isopycnals outcropping in the north of the sinking basin also outcrop in the channel, and flow parallel to these contours is adiabatic below the mixed layer. Because of longitudinal buoyancy gradients, the zonally-averaged remapping (5.7) distorts the vertical extent of the mixed layer. Values of $b^\sharp$ higher than $40\times10^{-3}\,\mathrm{m\,s^{-2}}$ are not plotted because the contours would be too close together.

The buoyancy value $b_m = 0.0085\,\mathrm{m\,s^{-2}}$ (thick black line in figure 3.3 and 3.4) is chosen to divide the upper and lower branches of the overturning. In practice, this isopycnal contour is chosen to pass as close as possible through the maxima of both the deep overturning cell in the sinking basin and the shallow overturning cell in the non-sinking basin. The upwelling across this isopycnal contour is approximately fixed by wind stress in the Southern Ocean (plus eddy transport of buoyancy) and global diapycnal diffusion (Gnanadesikan, 1999; Allison, 2009; Jones & Cessi, 2016), setting the cross-equatorial northward transport of the

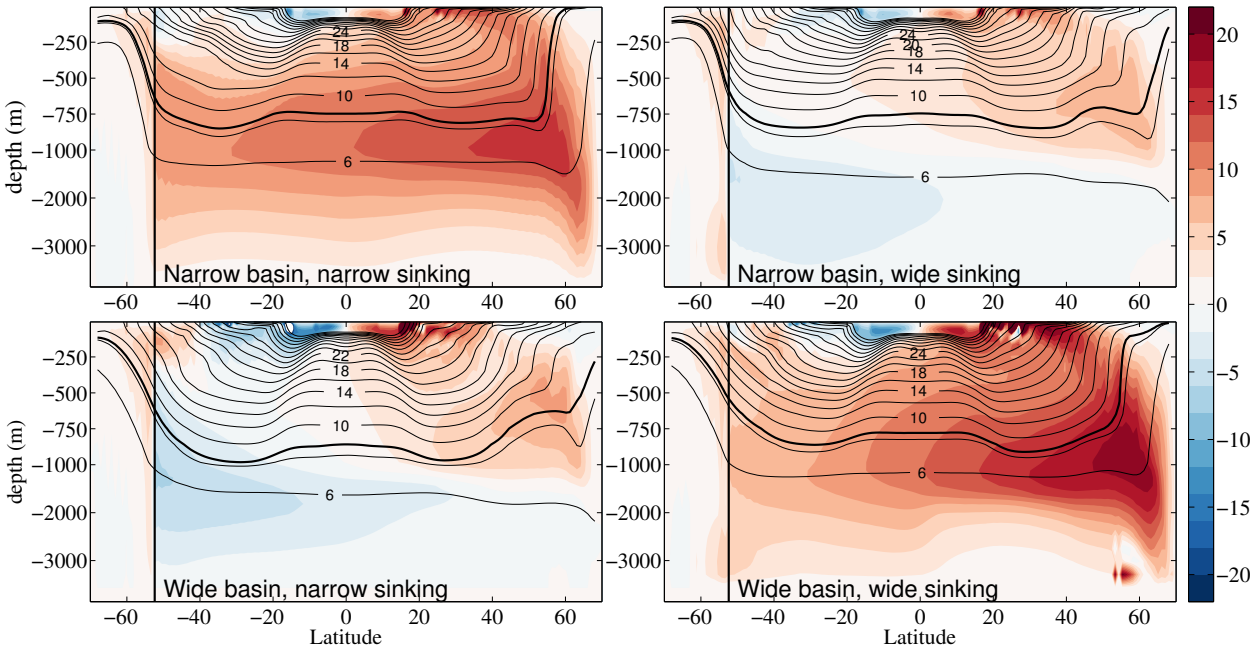

Figure 3.3: Residual overturning streamfunction in Sverdrups (color contours, spacing 2Sv), and $b^\sharp \times 10^3\,\mathrm{m\,s^{-2}}$, the buoyancy of the surface whose average depth is $\mathcal{Z}$ (black contours) in the narrow basin (top) and the wide basin (bottom), of narrow sinking (left) and wide sinking (right) for the W2N geometry. In all plots, the re-entrant channel region (left of the thick black vertical line) shows the total streamfunction integrated over all longitudes. The thick black contour denotes the isopycnal $b_m = 0.0085\,\mathrm{m\,s^{-2}}$ which bounds the upper branch of the MOC from below.

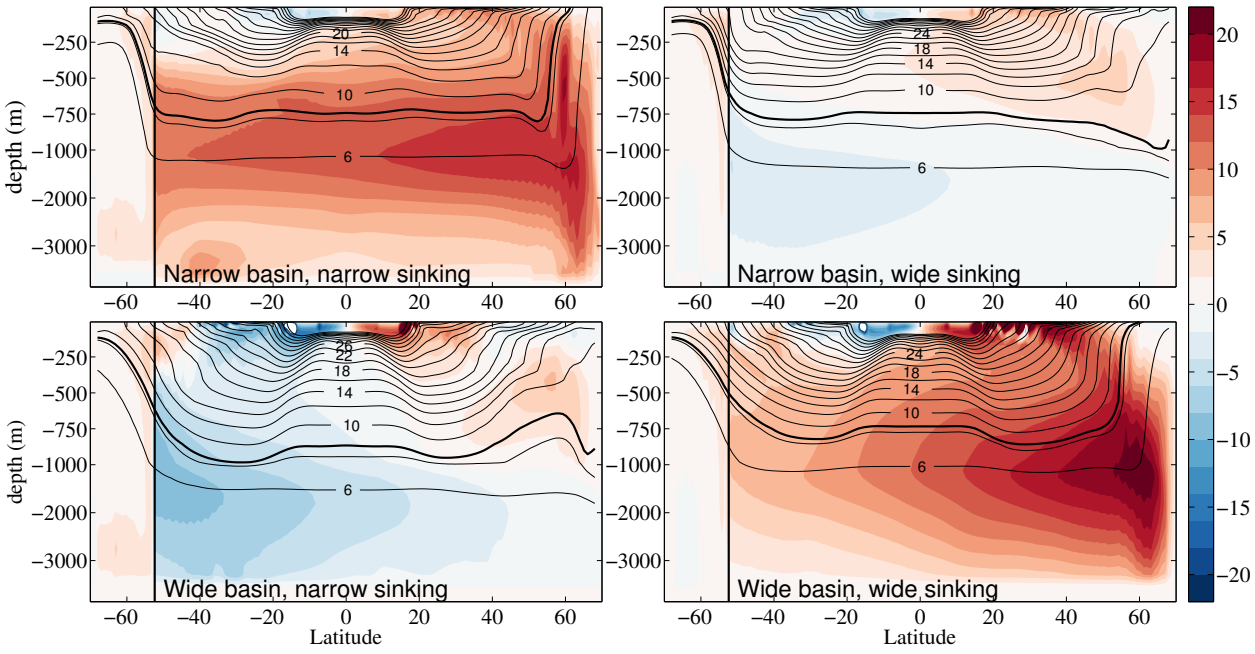

Figure 3.4: Residual overturning streamfunction in Sverdrups (color contours, spacing 2Sv), and $b^\sharp \times 10^3\,\mathrm{m\,s^{-2}}$, the buoyancy of the surface whose average depth is $\mathcal{Z}$ (black contours) in the narrow basin (top) and the wide basin (bottom), of narrow sinking (left) and wide sinking (right) for the W3N geometry. In all plots, the re-entrant channel region (left of the thick black vertical line) shows the total streamfunction integrated over all longitudes. The thick black contour denotes the isopycnal $b_m = 0.0085\,\mathrm{m\,s^{-2}}$ which bounds the upper branch of the MOC from below.

upper branch of the MOC in the sinking basin to approximately 11Sv regardless of the location of sinking (figure 3.5, red lines). This cross-equatorial transport, augmented by the diapycnal upwelling across b_m in the northern hemisphere of the sinking basin, determines the maximum transport of the MOC.

In the non-sinking basin, diffusive upwelling feeds a shallow cell in the northern hemisphere and an abyssal cell (mostly in the southern hemisphere). The upwelled water flows northward, sinking to about 1000m at high northern latitudes, and then returns southward. The meridional transport in the non-sinking basin integrated zonally and above b_m is shown in figure 3.5 (blue lines).

The numerical simulations indicate why wide sinking is unstable when the surface freshwater flux is symmetric: figure 3.6 (top panels) shows the salinity zonally and vertically averaged above b_m. The values in the sinking region of the wide basin (red dashed lines in the grey box of figures 3.6 and 3.7) are only slightly above the values in the narrow, non-sinking basin at the same latitudes (blue dashed lines in the grey box of figures 3.6 and 3.7): this is despite the decreased surface freshwater flux in the wide basin relative to the narrow basin. In other words, it appears that it is the zonal asymmetry in freshwater forcing that keeps the wide basin slightly saltier than the narrow basin. Without this asymmetry, the salinities of the basins reverse and narrow sinking occurs.

In order to quantify how the salinity might be distributed under zonally uniform forcing for wide sinking, we advect and diffuse a passive tracer with the velocity, diffusivity and convective adjustment time series from the wide sinking state. Unlike salt, the tracer is forced with the zonally uniform surface flux given by the solid line in figure 3.2. The resulting tracer field vertically averaged above b_m is shown in the bottom panel of figure 3.8. Compared to the salinity anomaly (middle panel of fig. 3.8), the tracer is lower in the wide basin and higher in the narrow basin, and comparable to the values encountered in the narrow sinking case (top panel of fig. 3.8). To make a more quantitave comparison between the three cases,

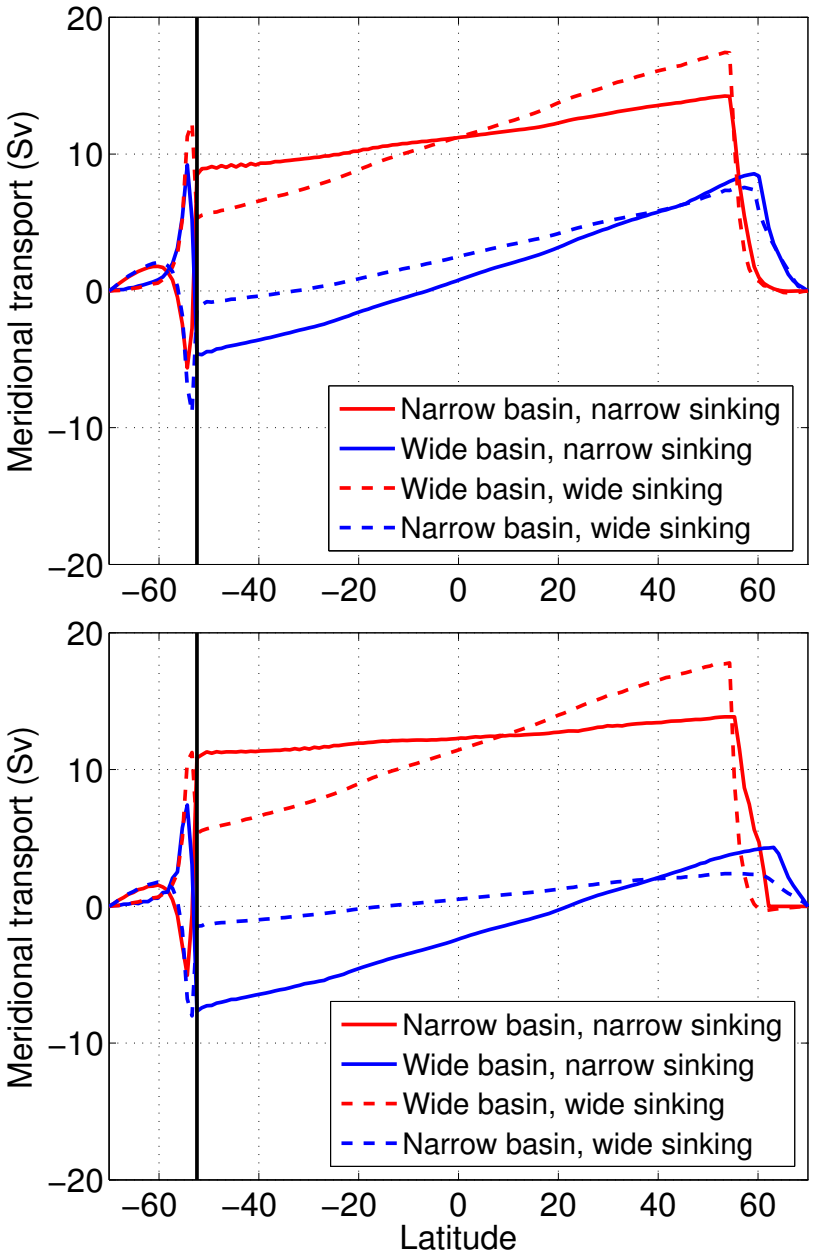

Figure 3.5: Meridional transport, zonally and vertically integrated within each sector above the isopycnal b_m for W2N (top) and W3N (bottom).

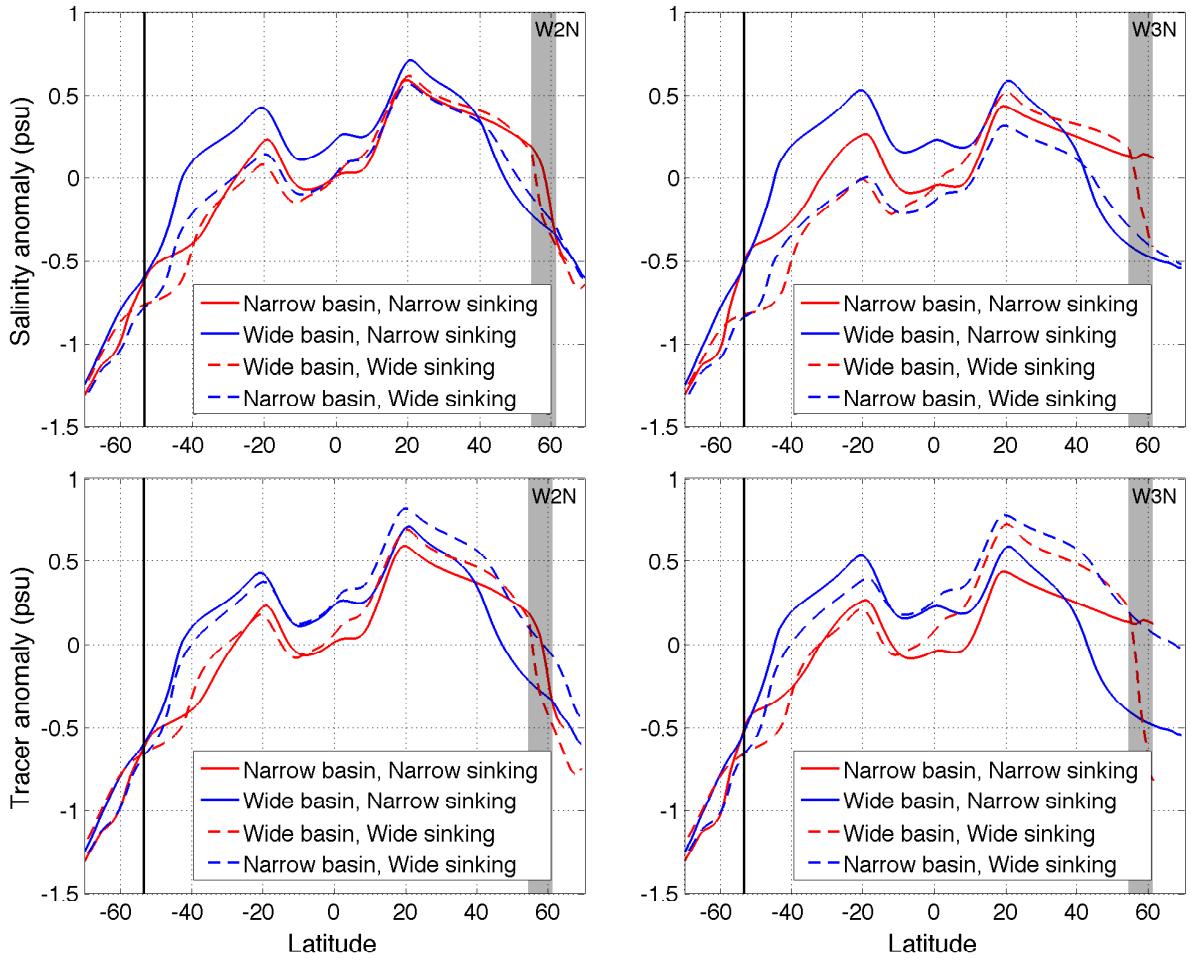

Figure 3.6: The depth and zonally averaged salinity anomaly (referenced to 35 PSU) above $b_m = 0.0085\,\mathrm{m\,s^{-2}}$ (top) and the depth and zonally averaged tracer anomaly above $b_m = 0.0085\,\mathrm{m\,s^{-2}}$ (bottom) for W2N (left) and W3N (right). The solid lines are for narrow sinking and the dashed lines are for wide sinking. The grey box marks the location of sinking.

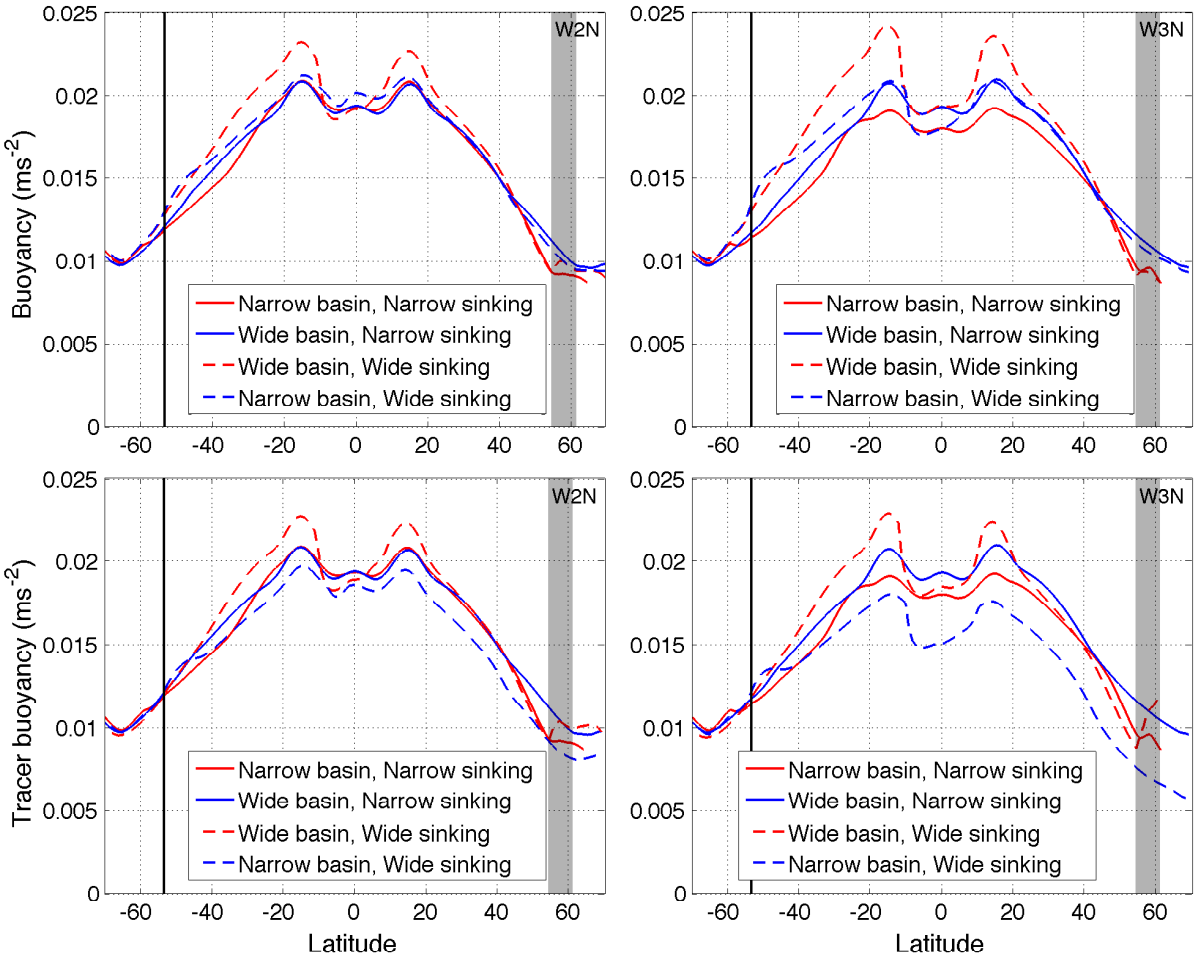

Figure 3.7: The zonally averaged buoyancy averaged above $b_m = 0.0085\,\mathrm{m\,s^{-2}}$ using the salinity (top) and using the passive tracer instead of salinity (bottom) for W2N (left) and W3N (right). For tracer buoyancy, the depth of b_m is still calculated using the salinity. The solid lines are for narrow sinking and the dashed lines are for wide sinking. The grey box marks the location of sinking.

it is useful to examine the salinity and tracer concentrations averaged above b_m, and then zonally averaged. Figure 3.6 shows that, for wide sinking, the tracer concentration anomaly at the latitudes of sinking is larger in the narrow basin than in the wide basin (compare the dashed lines in the gray box in the bottom panels of figure 3.6).

At high latitudes, the temperature is approximately independent of the location of sinking, and thus does not contribute directly to the preference for narrow over wide sinking. However, at the sinking latitudes, the temperature of the sinking basin is slightly higher than the temperature of the non-sinking basin, so it partially counteracts the effects of salinity on the buoyancy. Consequently, when the salinity in the sinking region is only marginally larger than the salinity in the non-sinking basin, the negative temperature advection feedback destabilizes the wide sinking state.

The buoyancy is displayed in the top panels of figure 3.7, vertically averaged above the isopycnal b_m, and then zonally averaged. For wide sinking, the buoyancy in the sinking region is lower than at the same latitudes of the narrow basin (compare the dashed lines in the gray box in the top panels of figure 3.7): wide sinking is obtained under zonally asymmetric forcing. In the bottom panels of figure 3.7, the symmetrically forced tracer is used instead of the salinity to find "tracer-buoyancy", i.e. the hypothetical buoyancy obtained if wide sinking occurred with zonally uniform salinity forcing. For wide sinking, the "tracer-buoyancy" at high latitudes is indeed lower in the narrow basin than in the wide basin (compare the dashed lines in the gray box in the bottom panels of figure 3.7). This confirms that the wide sinking solution is unstable under zonally uniform surface salt-flux forcing.

Salinity in turn affects the distribution of convective adjustment[2], which is rather different for narrow and wide sinking. Convective adjustment is the main process determining the diapycnal velocity across the buoyancy b_m. Thus, we use the diapcynal velocity, denoted

[2]In this 3-D model, convection is parameterized by convective adjustment: when the stratification is unstable, the vertical diffusivity is increased to $\kappa_v = 10\,\mathrm{m^2\,s^{-1}}$ until the buoyancy profile becomes stable.

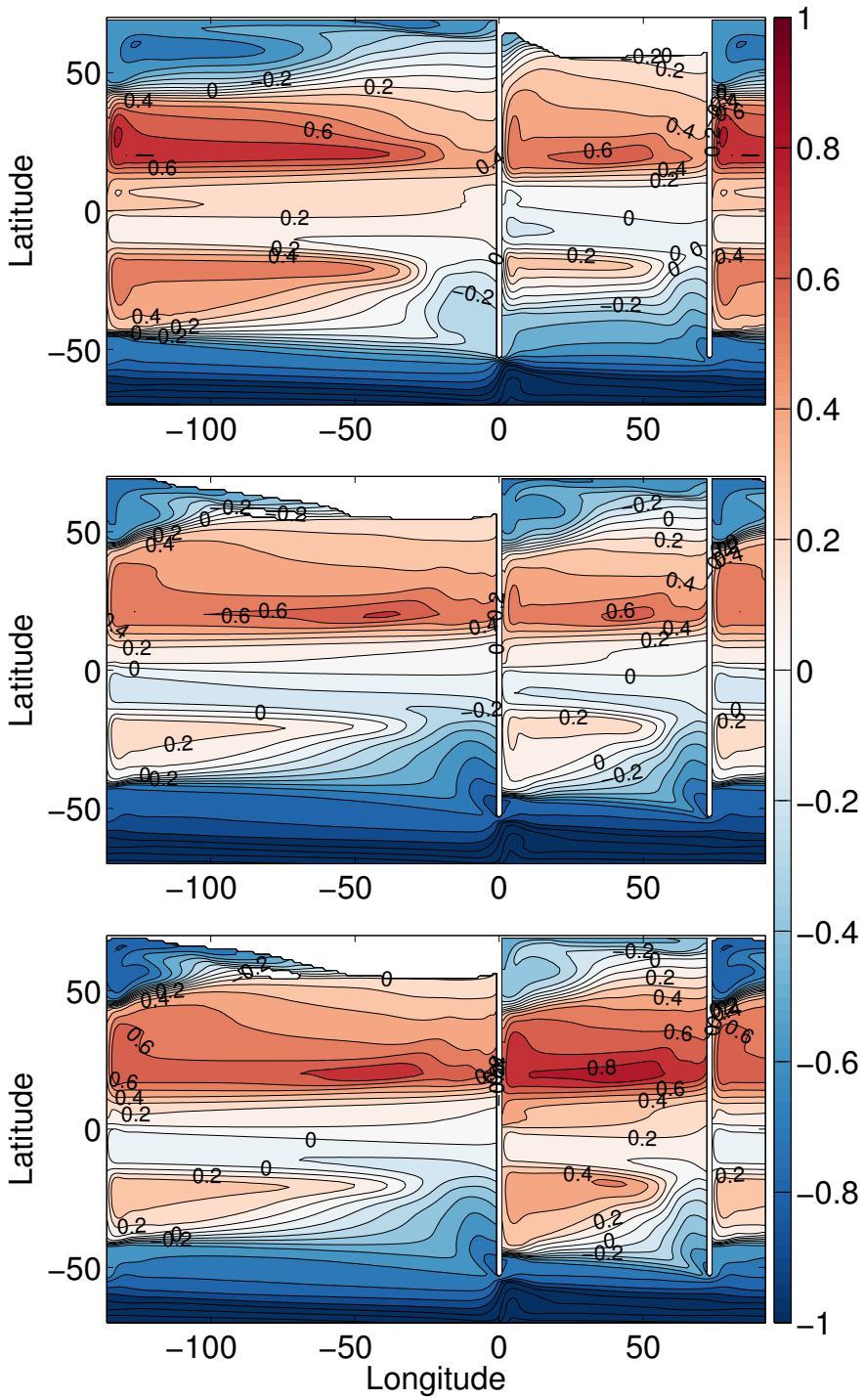

Figure 3.8: Salinity anomaly, referenced to 35 PSU, vertically averaged above the isopycnal $b_m = 0.0085\,\mathrm{m\,s^{-2}}$ for narrow sinking (top) and for wide sinking (middle) in the W2N geometry. Anomaly of the tracer advected and diffused as for wide sinking, vertically averaged over the same depth range as the middle panel (bottom). The isopycnal b_m outcrops in the white area.

with ϖ/b_z following the notation of Young (2012) (henceforth referred to as WRY12), as a measure of deep water formation. As illustrated in figure 3.9, ϖ/b_z occurs predominantly at the northern end of the sinking basin. For wide sinking, ϖ/b_z is confined to the eastern two thirds of the domain, whereas for narrow sinking, it is spread throughout the whole width of the basin. This pattern reflects the zonal distribution of salinity (cf. figures 3.9 and 3.8). In the western third of the wide sinking basin, the surface is especially fresh, while it is relatively salty almost everywhere in the narrow sinking basin.

We now demonstrate that the contrast in the zonal distribution of salinity results from differences in the velocities near the western boundary of the sinking basin. As shown in figure 3.10, for narrow sinking, the western boundary current is northward in the narrow basin south of about 57°. North of 57° the velocity is near zero. For wide sinking, the velocity on the western boundary of the wide basin is southward north of 45°, and northward south of 45°, i.e. the change of sign of the western boundary current coincides with the boundary between the subtropical gyre and the SPG. Therefore, salinity is transported farther north into the western portion of the SPG for narrow sinking. The resulting high salinity in the narrow basin enables deep convection (figure 3.9, top panel). In the north of the wide basin, deep water formation is suppressed on the western side of the SPG by the low salinities carried southward by the western boundary current, and the isopycnal b_m does not outcrop there (figure 3.9, bottom panel).

The western boundary velocity in the sinking basin is the sum of the northward flow of the MOC plus the western boundary current associated with the locally wind-driven, Sverdrupian gyre, which is northward in the subtropical gyre and southward in the SPG. For the W2N geometry, the Sverdrup transport of the SPG at 58° (halfway between the zero-wind-stress-curl line and 70°) is about 30 Sv in the wide basin and about 15 Sv in the narrow basin, as shown in figure 3.12. This interior transport produces a southward western boundary current in the SPG which is twice as fast in the wide basin than in the narrow

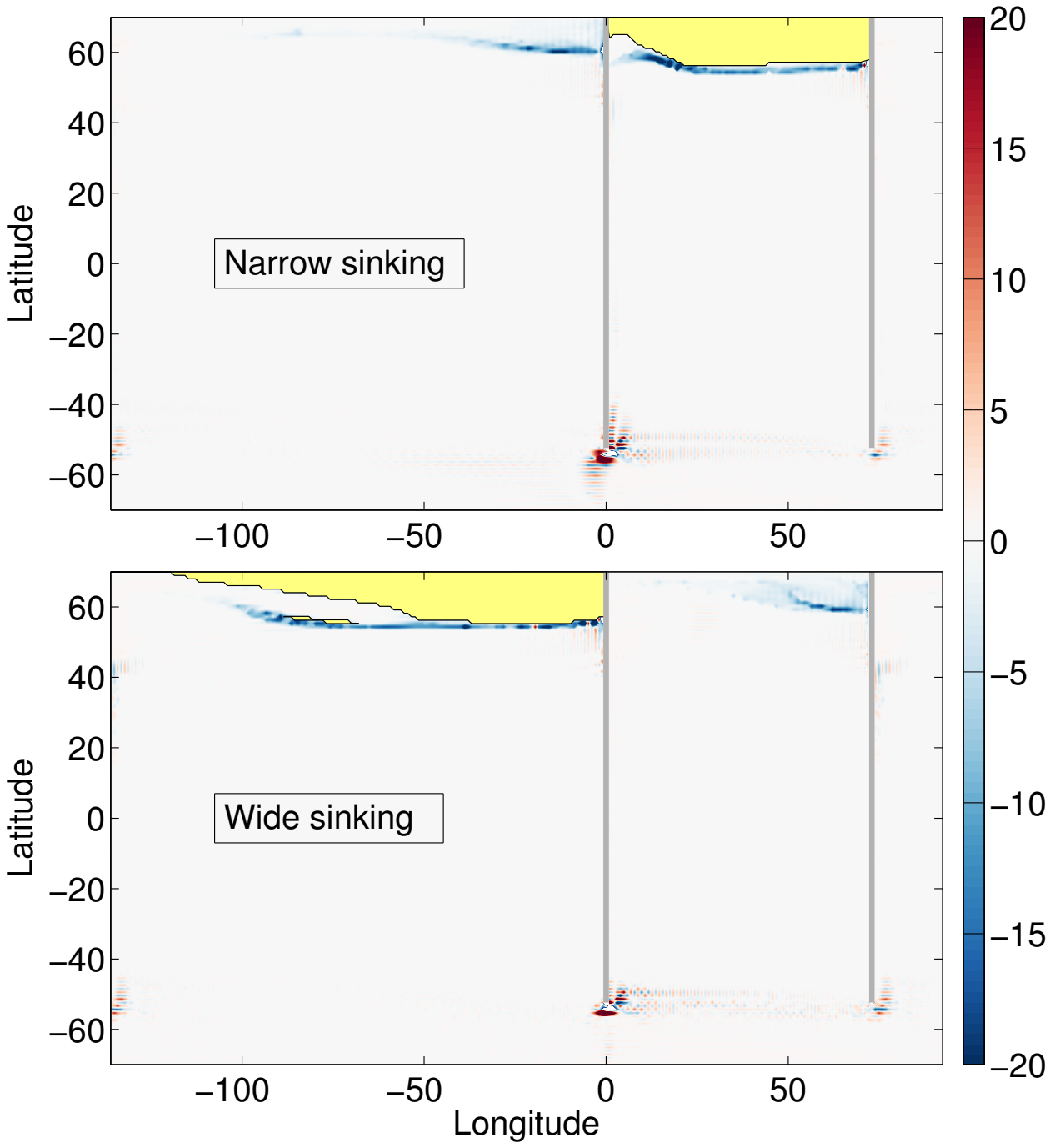

Figure 3.9: The diapycnal velocity $\varpi/b_z \times 10^6\,\mathrm{m\,s^{-1}}$ at isopycnal $b_m = 0.0085\,\mathrm{m\,s^{-2}}$ from the 3-D model for narrow sinking (top) and for wide sinking (bottom) in the W2N geometry. The isopycnal b_m outcrops in the yellow area.

basin. The zonal velocity associated with the Sverdrup gyre is also faster in the wide basin. However, the MOC transport, largely confined to a western boundary current within each basin, is about 15 Sv, independent of the width of the sinking basin. The total flow above b_m is approximately a linear combination of the gyres and the MOC western boundary current (Stommel, 1957). The MOC velocity is of similar amplitude to the SPG western boundary current in the narrow basin and in the opposite direction, but it is half of the velocity of the SPG western boundary current in the wide basin. As a result, the western boundary current is strong and southward in all the SPG of the wide basin but not in the narrow basin (as shown in figure 3.10). The difference in velocities on the western side of the basins leads to different salinity distributions in the SPG region: fresher in the wide sinking basin than in the narrow sinking basin. The halocline that forms on the western side of the wide basin suppresses deep water formation, localizing the diapycnal velocity to the eastern side of the wide basin. This localization, given a zonally uniform freshwater flux, reduces the efficiency of the salt feedback on water mass formation in the wide basin, giving a preference to narrow-basin sinking. To further demonstrate this process, in the following section we examine the salinity distribution obtained with zonally uniform fresh-water fluxes and velocities that are simplified relative to the full 3-D field.

3.3 2-D model and diagnostics

To understand the role of the epipcynal and diapycnal velocity in the salinity distribution we simplify the salinity equation in three dimensions. The MITgcm solves the three dimensional advection-diffusion equation[3]

$$\frac{\partial S}{\partial t} + (uS)_x + (vS)_y + (wS)_z = \boldsymbol{\nabla} \cdot (\mathbf{K}\boldsymbol{\nabla} S) + (\kappa_v S_z)_z \,, \tag{3.7}$$

[3]In this section we use Cartesian coordinates, but the actual computations are in the spherical coordinates appropriate for the sector shown in figure 2.4.

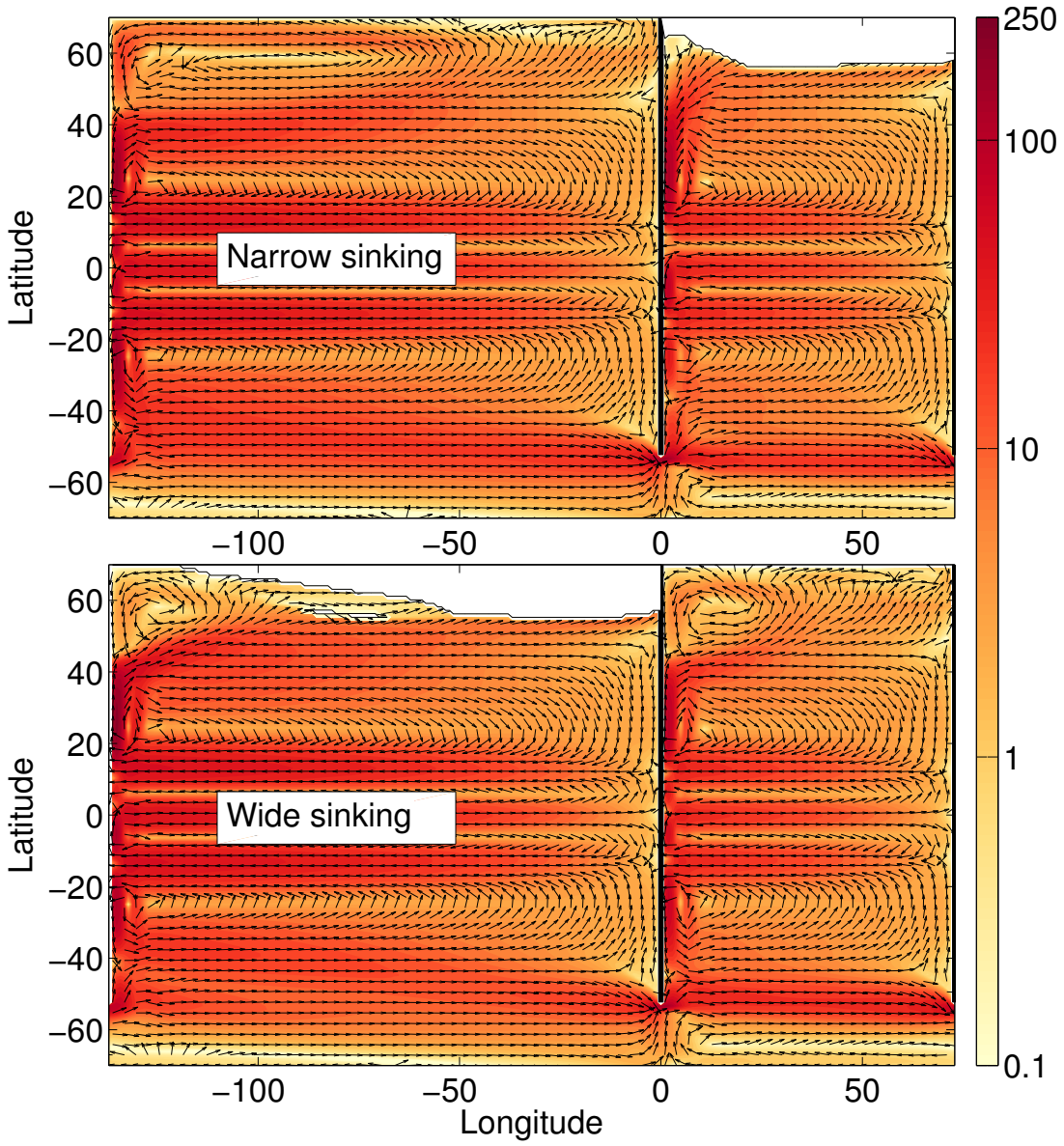

Figure 3.10: Magnitude (color) and direction (arrows) of the mean plus GM velocity vertically integrated above isopycnal $b_m = 0.0085\,\mathrm{m\,s^{-2}}$ for narrow sinking (top) and for wide sinking (bottom). Each arrow represents the mean direction over a $3° \times 3°$ box, while the magnitude is on the model's grid. The contour color scale is in $\mathrm{m^2\,s^{-1}}$ and is spaced logarithmically to visualize both boundary and interior currents. The isopycnal b_m outcrops in the white area.

where S is the salinity and (u, v, w) is the eulerian plus GM velocity in the (x, y, z)-direction respectively. $\mathbf{K}$ is the Redi (1982) tensor defined in (5.9) and κ_v is the vertical diffusivity.

A reduced description is obtained by integrating (3.7) vertically from the buoyancy surface b_m to the sea surface and changing to buoyancy coordinates, $(\tilde{x}, \tilde{y}, \tilde{b}, \tilde{t})$, following WRY12 (details are in appendix A1). Making the further assumption that S is vertically homogeneous above b_m we obtain

$$(-\zeta\overline{S})_{\tilde{t}} + (U\overline{S})_{\tilde{x}} + (V\overline{S})_{\tilde{y}} - \frac{\varpi}{b_z} S\Big|_{\zeta} = -\left(\zeta\kappa_{GM}\overline{S}_{\tilde{x}}\right)_{\tilde{x}} - \left(\zeta\kappa_{GM}\overline{S}_{\tilde{y}}\right)_{\tilde{y}} - FS_{ref} - \kappa_v S_z|_{\zeta}\,, \quad (3.8)$$

where κ_{GM} is the Redi diffusion coefficient (here taken equal to the GM eddy-diffusivity), $U = \int_{\zeta}^{0} u\, dz$ and $V = \int_{\zeta}^{0} v\, dz$ are the sum of eulerian plus GM velocities depth-integrated above b_m, $\overline{S}$ is the salinity depth-averaged above b_m, and $\zeta(\tilde{x}, \tilde{y})$ is the time-averaged depth of the isopycnal b_m. We further assume

$$S|_{\zeta} = \overline{S}, \quad S_z|_{\zeta} = \frac{\overline{S}}{-\zeta}\,. \quad (3.9)$$

The 2-D model is now exploited to more deeply understand the mechanisms that determine the salinity distribution, using the vertically integrated velocity field, which satisfies the incompressibility condition in buoyancy coordinates (ζ is assumed to be independent of time):

$$U_{\tilde{x}} + V_{\tilde{y}} = \frac{\varpi}{b_z}\,. \quad (3.10)$$

3.3.1 Vertically integrated velocities from in the 3-D model

We obtain U and V by integrating the residual velocities in the 3-D W2N geometry vertically above $b = b_m$. ζ is the associated time-mean depth of the isopycnal b_m and ϖ/b_z is obtained from (3.10). Unlike the 3-D salinity computations, here the freshwater flux is zonally uniform for both narrow and wide sinking, just as in the passive tracer experiments described

in the previous section. The goal of this 2-D experiment is to diagnose which components of the velocities are essential to determine the differences in the salinity distribution between narrow- and wide-sinking. The U, V field in the northern hemisphere is shown in figure 3.10, and ϖ/b_z is shown in figure 3.9.

Despite ignoring the baroclinic terms, the 2-D salinity obtained with (3.8) reproduces fairly well some aspects of the 3-D computations and in particular the salinity vertically averaged above b_m (compare the bottom left panel of figure 3.6 with panel **a** of figure 3.11), indicating that the vertically integrated transport dominates the salinity distribution of the upper branch of the MOC, especially in the subpolar regions. The agreement is less satisfactory in the subtropical regions, where the depth of b_m is largest: here the vertical correlation of the baroclinic components dominates the salinity transport (diagnostic not shown). The resulting salinities are higher at the northern end of the SPG in the narrow basin for both narrow and wide sinking velocities (red solid and blue dashed lines in the gray box of figure 3.11, panel **a**), i.e. the 2-D model confirms the prediction of the passive tracer 3-D computations that narrow sinking is preferred when the freshwater flux is zonally symmetric.

Because the 2-D advection/diffusion model (3.8) treats $\overline{S}$ as a passive scalar, it does not incorporate the salt feedback controlling the onset of convective adjustment in the sinking region and the associated large diapycnal velocity ϖ/b_z. To demonstrate that the spatial distribution of ϖ/b_z is important, we conduct an experiment where this spatial distribution is varied.

In the 2-D experiment reported in the left panels of figure 3.11, the term ϖ/b_z extends over the whole width of the basin for narrow sinking, but it is confined to the eastern two-thirds of the basin for wide sinking (as shown in figure 3.9). An additional experiment is carried out where ϖ/b_z is modified to be zonally uniform in the sinking basin north of 46°, keeping the meridional velocity, V, unchanged. The changes in ϖ/b_z are accommodated

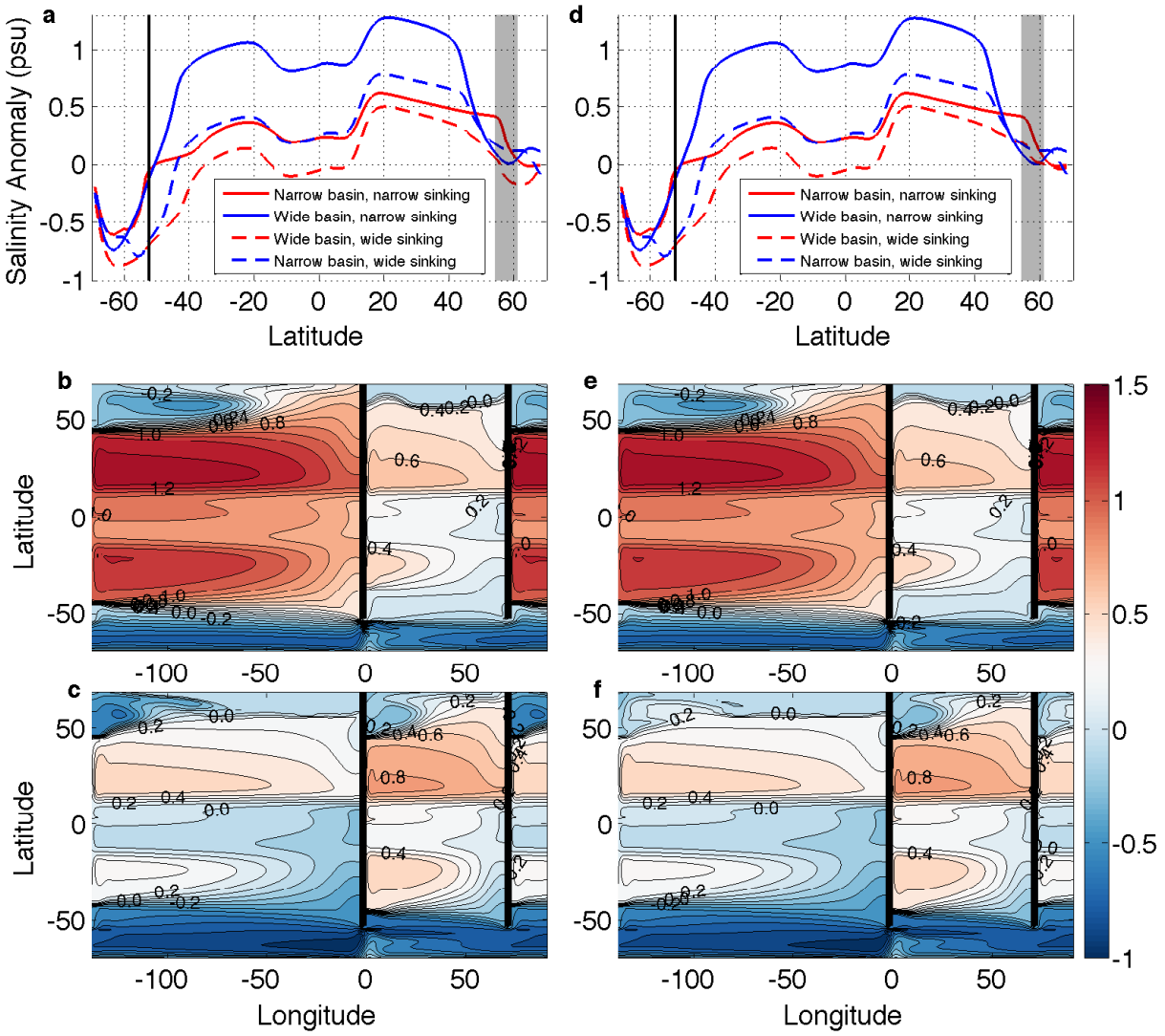

Figure 3.11: Salinity anomaly solution of (3.8) using $U, V, \varpi/b_z$ and ζ from the W2N computation a) zonally averaged and plotted as a function of latitude and longitude for b) narrow sinking and c) wide sinking. d)-f), as in a)-c), but where U and ϖ/b_z are modified such that ϖ/b_z is zonally homogenized in the subpolar gyre of the sinking basin. The depth of the layer, $-\zeta$, is capped so that the minimum depth is 70 m. Contours are every 0.1 PSU. The grey box in figures a) and d) marks the location of sinking.

by changing the zonal velocity, U, so that (3.10) is satisfied. The zonal integral of ϖ/b_z is conserved at every latitude in this process, and the velocities outside the SPG of the sinking basin remain unchanged. With advection by this modified velocity field the sinking wide basin gets saltier (compare the red dashed lines in panels **a** and **d** of figure 3.11), because the fresh water flowing south in the western boundary sinks rather than being advected eastward into the SPG. The salinity remains essentially unchanged for narrow sinking (compare the solid lines in panels **a** and **d** of figure 3.11), because ϖ/b_z is already approximately homogenous for narrow sinking. Therefore the preference for narrow sinking is reduced when the suppression of convective adjustment by freshening, i.e. the salt-advection feedback, is removed.

In summary, the salinity in the upper branch of the MOC is controlled by the velocity vertically averaged above the isopycnal b_m and by the pattern of strong diapycnal velocity due to convective adjustment. The associated deep water mass formation is suppressed by a halocline on the western side of the wide basin. This latter feedback is not captured by (3.8), which treats salinity as a passive scalar, but the contrast between the two experiments with the localized versus homogenized ϖ/b_z illustrates this effect. Both experiments reveal that the velocity field in the SPG is responsible for the halocline formation on the western side of the wide sinking region.

To strengthen our argument that it is the *superposition* of the SPG velocity plus the MOC's western boundary current that controls the formation of the halocline in the western part of the SPG, we perform two additional experiments with idealized velocities representing either the gyral circulation alone, or the MOC circulation alone. Neither of these patterns in isolation leads to the observed differences in SPG salinities.

3.3.2 2-D advection/diffusion of salinity with idealized velocities

In the following, we show that, in isolation, neither the gyral velocities alone nor the MOC velocity alone can lead to a halocline in the wide basin SPG.

We first show the salinity distribution with advection by idealized vertically integrated velocities U_{gyre} and V_{gyre} representing the gyres in the 2-D model. The fields U_{gyre} and V_{gyre} are found by solving the 2-D primitive equations in a domain with W2N geometry, uniform buoyancy, depth 700m and wind forcing, τ. Two ridges, one south of the continent at $0°E$ with height 280m and one south of the continent at $70°E$ with height 140m, are included in order to keep the circumpolar transport comparable to that in the 3-D simulation. The resulting horizontally non-divergent transport is described by a single streamfunction shown in figure 3.12, and there is neither a diapycnal velocity, nor a zonally averaged meridional transport. Figure 3.13 shows the distribution of the resulting tracer solution of (3.8), forced by the zonally uniform freshwater flux of figure 3.2. In the along-streamlines direction, the dominant balance is between the isopycnal advection terms and the surface salinity flux. In the across-streamlines direction, the dominant balance is between the isopycnal diffusion terms and the surface salinity flux.

Although the gyres in the wide basin have twice the western boundary current transport compared to the narrow basin, the interbasin salinity difference is minimal: the minimum salinity in the wide basin's SPG is 0.07 PSU fresher than the minimum salinity in the narrow basin's SPG (bottom panel of figure 3.13) and the zonally averaged salinities differ very little between basins (top panel of figure 3.13). These differences are too small to explain the preference for narrow sinking seen in the 3-D model, and a scale analysis in appendix A2 confirms that the salinity in this configuration is independent of basin width.

We now examine the salinity distribution with a velocity field characterized by sinking and a western boundary current associated with the MOC *without* wind-driven gyres. The velocities U, V and ϖ/b_z in (3.8) are defined analytically. They are confined to a western

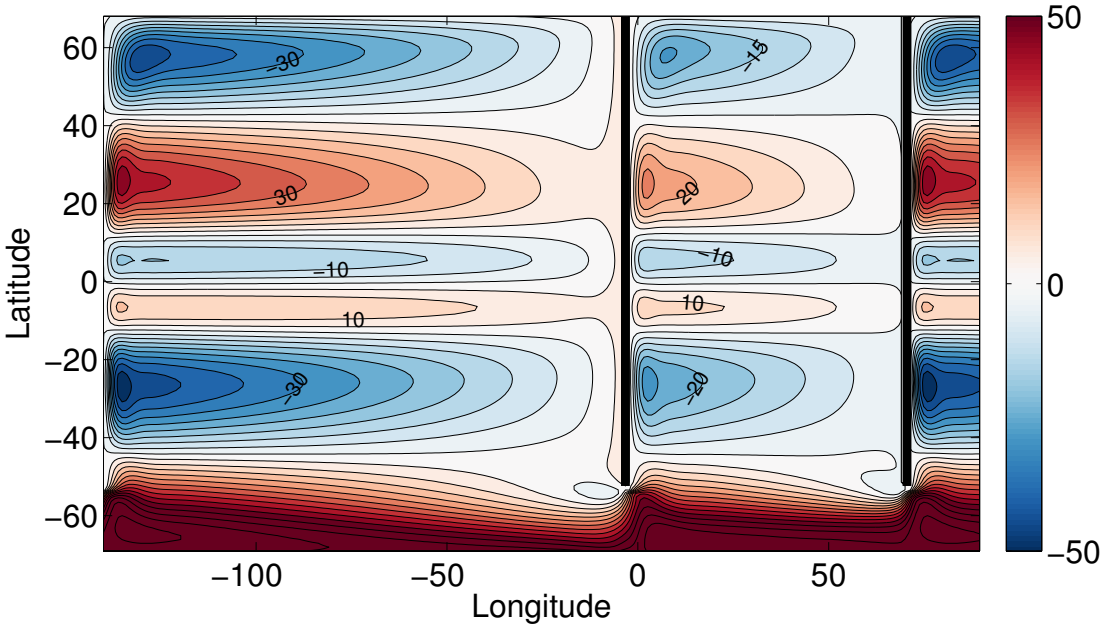

Figure 3.12: Streamfunction in Sverdrups associated with U_{gyre} and V_{gyre}. Contours are every 5Sv.

boundary current in a single basin fed by upwelling in the periodic channel. In the western boundary current and most of the channel, the dominant balance in (3.8) is between isopycnal salinity advection and the surface salinity flux. Elsewhere, velocities are very small, so the dominant balance is between isopycnal diffusion and the surface salinity flux. The idealized velocity fields for both narrow- and wide-sinking are shown in figures 3.14 and 3.15 (panels **c** and **d**), with ζ shown in figure 15 (panel **b**). The resulting zonally averaged salinities are shown in figure 3.15 (panel **a**): this configuration illustrates that the main effect of the MOC's velocity is to reduce the latitudinal salinity gradients in the sinking basin relative to the non-sinking basin, without privileging narrow versus wide sinking.

3.4 Conclusions

In a configuration with two basins of different widths connected by a re-entrant channel, sinking occurs in the narrow basin under zonally uniform forcing. Deep-water formation in the wide basin can be coerced by reducing the freshwater flux over the north of the wide

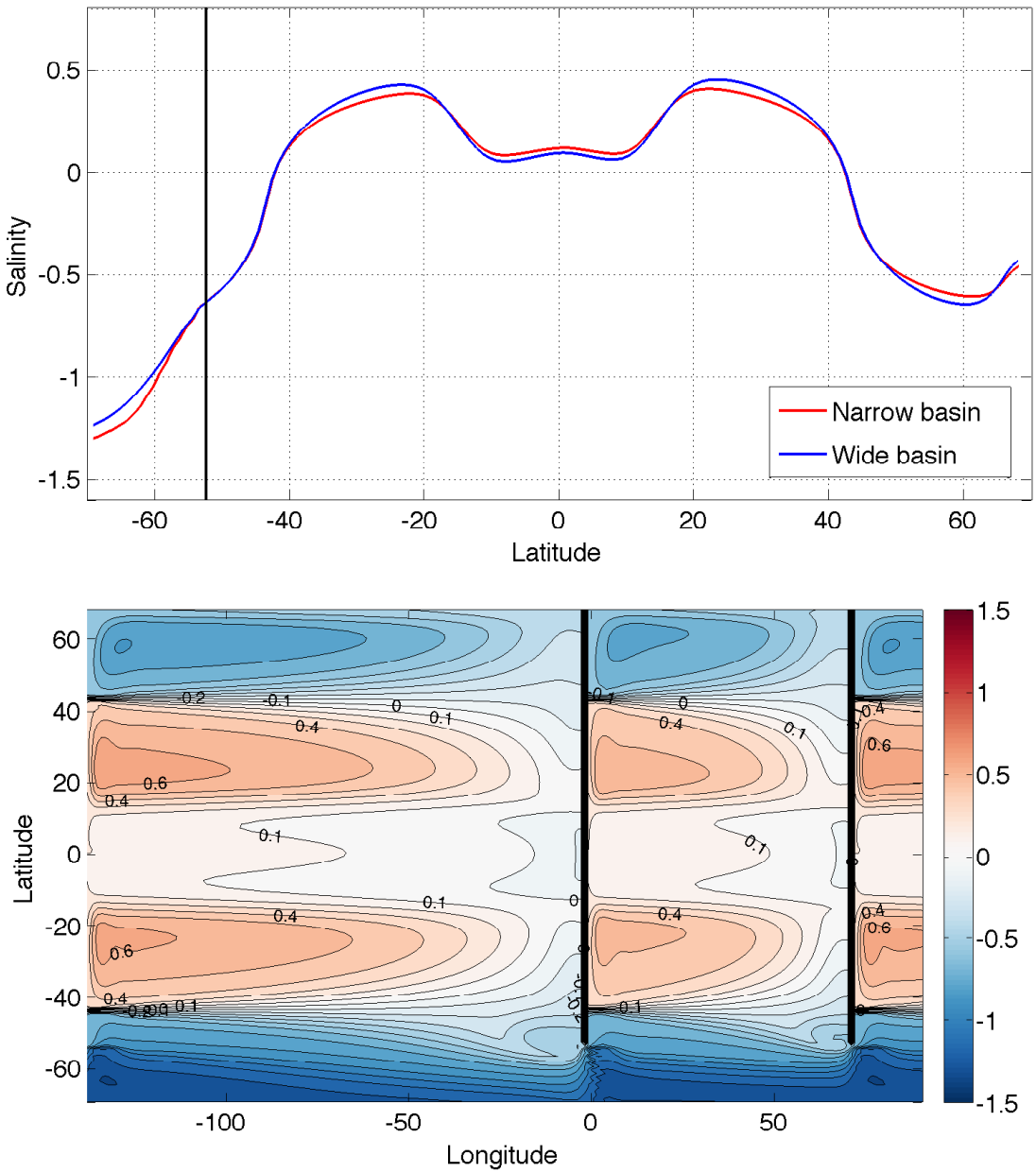

Figure 3.13: Zonally average salinity anomaly (top) and salinity anomaly (bottom) when (3.8) uses the velocity associated with the streamfunction in figure 3.12 and $\zeta = -700$m with contours every 0.1 PSU.

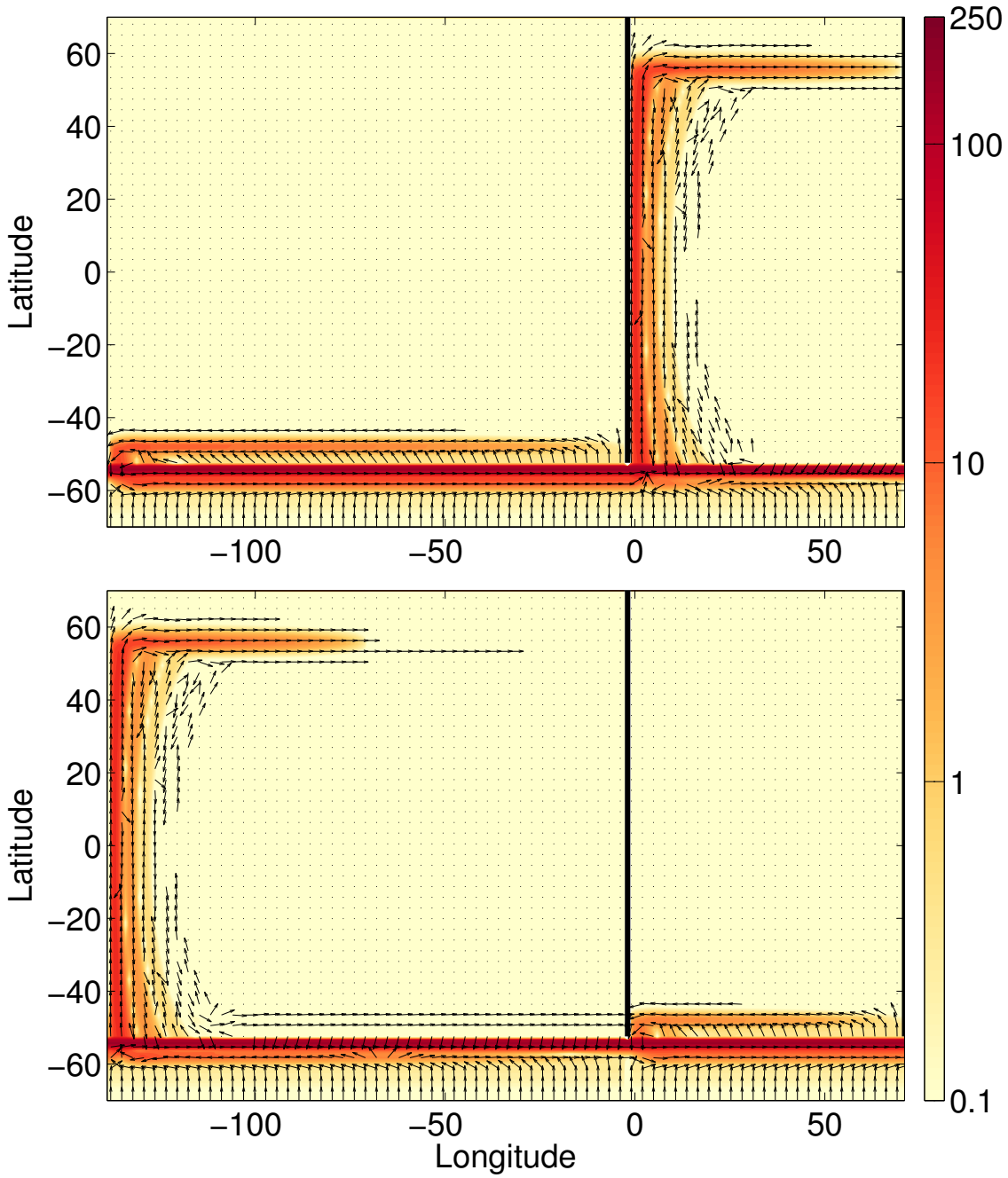

Figure 3.14: Magnitude (colors) and direction (arrows) of depth-integrated velocity ($\mathrm{m^2\,s^{-1}}$) in the idealized 2-D model for narrow sinking (top) and wide sinking (bottom). Arrows are not plotted if the magnitude of the depth-integrated velocity is less than $0.01\,\mathrm{m^2\,s^{-1}}$. Each arrow represents the mean direction over a $3^\circ \times 3^\circ$ box while the magnitude is on the models grid.

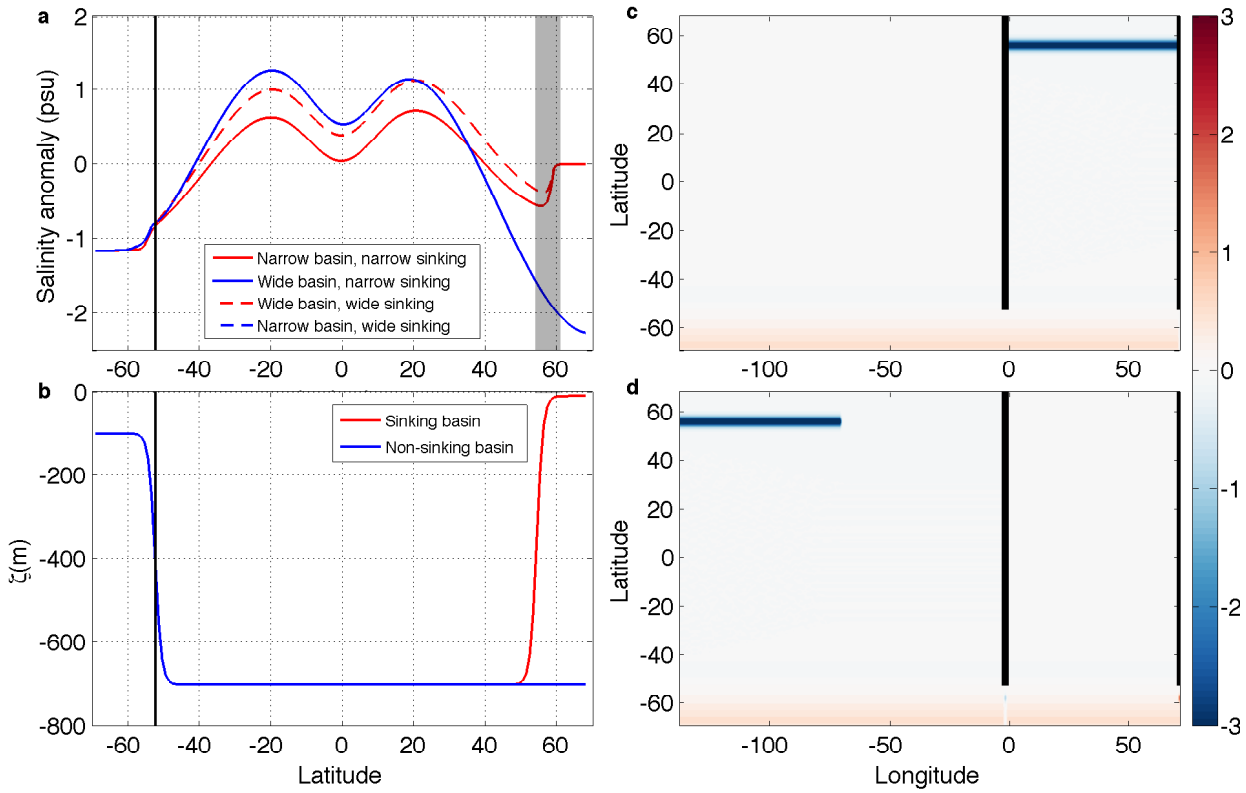

Figure 3.15: a) Zonally averaged salinity anomaly from the idealized 2-D model using the velocity fields shown in figure 14, b) the depth of the layer $\zeta(m)$, and the diapycnal velocity $\varpi \times 10^6\,\mathrm{m\,s^{-1}}$ c) for narrow sinking and d) for wide sinking. In a), the blue solid line and the blue dashed line are on top of each other.

basin, and then we find that a stronger reduction is needed for larger ratios of basin-widths. Despite the reduction in freshwater flux for wide-sinking, the salinity difference between the sinking basin and the non-sinking basin is smaller when sinking occurs in the wide basin.

High salinity in the north of the sinking basin is always reinforced by a large cross-equatorial overturning cell, which transports salt northward across the equator: this is the salt-advection positive feedback (Stommel, 1961). However, this feedback is less effective for wide-sinking. In particular, for zonally uniform salinity flux, we show that the wide sinking state is unstable. This is because higher salinity (and therefore lower buoyancy) is found at the surface in the north of the narrow basin, and fresh water is more efficiently advected southward by the subpolar wind-driven gyre in the wide basin. The temperature-advection negative feedback also plays a small role. When the width of the narrow basin is reduced further, keeping the width of the wide basin constant, the salinity difference between the basins increases, as does the preference for narrow sinking.

A 2-D advection-diffusion model shows that the advection of salinity in the upper branch of the 3-D overturning is well represented by the velocity vertically integrated above the isopycnal that divides the upper and lower branch of the MOC. The vertically integrated velocities show that there is a crucial difference in the sense of circulation on the western side of the SPG between the wide- and narrow-sinking basins. For narrow sinking the western boundary current in the SPG is very weak and for wide sinking it is strong and southward, advecting fresh water from the north, forming a halocline which is absent in the narrow-sinking basin. This halocline is advected eastward by the southern branch of the SPG, suppressing deep water mass formation.

We rationalize the difference between narrow and wide sinking by invoking linear superposition of the western boundary velocities associated with the wind-driven SPG and with the MOC. The latter is independent of the basin size, while the former is larger for a wide basin, and it prevails over the MOC in the wide-sinking basin. This is consistent

with Warren (1983)'s suggestion that the small flow rate between the subtropical gyre and the SPG in the Pacific leads to lower salinities in the North Pacific when sinking is in the Atlantic, and with the observations of Hátún *et al.* (2005); Häkkinen & Rhines (2004) that salinity in the North Atlantic increases with decreasing SPG's strength. We extend Warren's idea by showing that even when sinking is induced in the Pacific, the salt-advection feedback is less effective there because of the stronger Sverdrupian SPG circulation.

We further emphasize the interaction of the gyral velocities with the MOC by contrasting the effect of the two velocity components in isolation. Advection by gyres-only velocities or MOC-only velocities leads to no preference for narrow-sinking.

Our arguments work well in the idealized context of our model, with simple coastlines, flat bottom and zonally uniform steady forcing. There is evidence that topographic steering alters the position of the inter-gyre boundary (Zhang & Vallis, 2007), as does time-dependence due to well-resolved eddies, even in idealized geometries (Lévy *et al.*, 2010). Thus, it is not clear how robust the narrow-sinking preference is in more complex settings.

Models with realistic geometry and forcing find that the transport of the SPG in the North Atlantic is about 20 Sv (Bryan *et al.*, 1995; Eden & Willebrand, 2001), which is only slightly larger than the 18 Sv observational estimate of the transport of the MOC in the North Atlantic (Talley, 2013). The strength of the Pacific SPG western boundary current in the CCSM4 model (Gent *et al.*, 2011) is resolution dependent, but in CCSM4 T31 (a high-resolution run), the transport of the Pacific SPG is about 30 Sv, which would be sufficient to overwhelm the 18 Sv MOC transport. It is difficult to compare observations of the SPG transport between the Atlantic and Pacific, because most long-term observations are limited to 2000m depth and hence include the upper branch of the MOC. Deep water formation largely occurs in marginal seas, rather than in the open ocean, as it does in our model. Despite these caveats, our results indicate that the Atlantic's narrowness is a favorable asymmetry for sinking, which adds to the freshwater flux asymmetry.

Acknowledgements

CSJ and PC are supported by the National Science Foundation under Grants 446 No. OCE-1258887 and OCE-1634128. Computational resources were provided by XSEDE consortium, which is supported by National Science Foundation Grant ACI-1053575. CSJ thanks Ian Eisenman and Eric Chassignet for valuable conversations and both CSJ and PC thank the two anonymous reviewers for their helpful comments on this work.

Chapter 3, in full, is a reprint of the material as it appears in the Journal of Physical Oceanography 2017. Jones, C. S.; Cessi, Paola, American Meteorological Society, 2017.

3.A The 2-D advection-diffusion equation

In order to simplify the advection-diffusion equation, we integrate (3.7) vertically from the depth $\zeta(\tilde{t}, \tilde{x}, \tilde{y}, \tilde{b} = b_m)$ to the surface, where b_m is a constant. This gives

$$\int_\zeta^0 S_t \, dz + \int_\zeta^0 (uS)_x \, dz + \int_\zeta^0 (vS)_y \, dz - wS|_\zeta = \int_\zeta^0 \nabla \cdot (\mathbf{K} \nabla S) \, dz - F S_{ref} - \kappa_v S_z|_\zeta \,, \tag{3.11}$$

where the Redi tensor is defined as

$$\mathbf{K} \equiv \kappa_{GM} \begin{pmatrix} 1 & 0 & -\frac{b_x}{b_z} \\ 0 & 1 & -\frac{b_y}{b_z} \\ -\frac{b_x}{b_z} & -\frac{b_y}{b_z} & \left| \frac{\nabla_h b}{b_z} \right|^2 \end{pmatrix} , \tag{3.12}$$

and κ_{GM} is the Gent-McWilliams diffusion coefficient. Substituting $\mathbf{K}$ into (3.11) and expanding the Redi matrix yields

$$\int_\zeta^0 S_t \, dz + \int_\zeta^0 (uS)_x \, dz + \int_\zeta^0 (vS)_y \, dz - wS|_\zeta = \begin{matrix} \text{Redi} \\ \text{terms} \end{matrix} - F S_{ref} - \kappa_v S_z|_\zeta \,, \tag{3.13}$$

where

$$\begin{matrix} \text{Redi} \\ \text{terms} \end{matrix} = \int_\zeta^0 \left[\kappa_{GM} \left(S_x - \frac{b_x}{b_z} S_z \right) \right]_x + \left[\kappa_{GM} \left(S_y - \frac{b_y}{b_z} S_z \right) \right]_y + \left[\kappa_{GM} \left(-\frac{b_x}{b_z} S_x - \frac{b_y}{b_z} S_y + \left| \frac{\nabla_h b}{b_z} \right|^2 S_z \right) \right]_z dz \tag{3.14}$$

A substantial simplification of (3.13) and (3.14) is obtained by moving from eulerian coordinates (x, y, z, t) to buoyancy coordinates $(\tilde{x}, \tilde{y}, \tilde{b}, \tilde{t})$, using the rules (21) to (24) in WRY12. Because $\zeta_x = \zeta_y = \zeta_t = 0$, the horizontal derivatives can be moved outside the vertical integral giving

$$\left(\int_\zeta^0 S \, dz \right)_t + \left(\int_\zeta^0 uS \, dz \right)_x + \left(\int_\zeta^0 vS \, dz \right)_y - wS|_\zeta = \begin{matrix} \text{Redi} \\ \text{terms} \end{matrix} - F S_{ref} - \kappa_v S_z|_\zeta \,, \tag{3.15}$$

where

$$\underset{\text{terms}}{\text{Redi}} = \left(\int_\zeta^0 \kappa_{GM} S_{\tilde{x}}\, dz\right)_x + \left(\int_\zeta^0 \kappa_{GM} S_{\tilde{y}}\, dz\right)_y + \kappa_{GM}\left(\frac{b_x}{b_z} S_{\tilde{x}} + \frac{b_y}{b_z} S_{\tilde{y}}\right)\Big|_\zeta . \tag{3.16}$$

Noice that so far there are derivatives with respect to both buoyancy and eulerian coordinates. Changing all derivatives from eulerian coordinates (x, y, z, t) to buoyancy coordinates $(\tilde{x}, \tilde{y}, \tilde{b}, \tilde{t})$ and using (28) in WRY12, we obtain

$$\begin{aligned}\left(\int_\zeta^0 S\, dz\right)_{\tilde{t}} + \left(\int_\zeta^0 uS\, dz\right)_{\tilde{x}} + \left(\int_\zeta^0 vS\, dz\right)_{\tilde{y}} + \left(\zeta_{\tilde{t}} + u\zeta_{\tilde{x}} + v\zeta_{\tilde{y}} - w\right) S|_\zeta = \\ \left(\int_\zeta^0 \kappa_{GM} S_{\tilde{x}}\, dz\right)_{\tilde{x}} + \left(\int_\zeta^0 \kappa_{GM} S_{\tilde{y}}\, dz\right)_{\tilde{y}} - F S_{ref} - \kappa_v S_z|_\zeta .\end{aligned} \tag{3.17}$$

We separate velocity and salinity into a vertical average from ζ to the surface, denoted by overbar, and a departure from this average, denoted by prime, i.e. $u = \overline{u} + u'$, $v = \overline{v} + v'$ and $S = \overline{S} + S'$ and neglect quadratic terms in u', v' or S'. Using relation (33) in WRY12, i.e.

$$w = \zeta_{\tilde{t}} + u\zeta_{\tilde{x}} + v\zeta_{\tilde{y}} + \frac{\varpi}{b_z} , \tag{3.18}$$

where ϖ/b_z is the diapycnal term, we finally obtain

$$\left(-\zeta\overline{S}\right)_{\tilde{t}} + \left(U\overline{S}\right)_{\tilde{x}} + \left(V\overline{S}\right)_{\tilde{y}} - \frac{\varpi}{b_z} S\Big|_\zeta = -\left(\zeta\kappa_{GM}\overline{S}_{\tilde{x}}\right)_{\tilde{x}} - \left(\zeta\kappa_{GM}\overline{S}_{\tilde{y}}\right)_{\tilde{y}} - F S_{ref} - \kappa_v S_z|_\zeta . \tag{3.19}$$

3.B Salinity scaling for advection by gyres-only velocity

Here we illustrate how the difference in salinity between the SPG and the subtropical gyre scales with the external parameters, assuming that the gyral velocities are horizontally

non-divergent. With no diapcynal velocity (3.8) becomes

$$U_{gyre}\overline{S}_x + V_{gyre}\overline{S}_y \approx -FS_{ref} + \boldsymbol{\nabla}\cdot(-\zeta\kappa_{GM}\boldsymbol{\nabla}\overline{S})\,, \tag{3.20}$$

where we have neglected time dependence, diapycnal and Redi diffusion. Integrating over the area, A, enclosed by the outermost closed streamline of the SPG, we have

$$\int_A FS_{ref}\,da = -\oint_C \zeta\,\kappa_{GM}\boldsymbol{\nabla}\overline{S}\cdot\boldsymbol{n}\,dl\,, \tag{3.21}$$

where C is the arclength along the boundaries between gyres and $\mathbf{n}$ is a unit vector perpendicular to that boundary. The solid boundaries have no diffusive flux, so the difference in salinity between the subtropical and subpolar gyre, ΔS, is dominated by the diffusion at the intergyre boundary on the RHS of (3.21). Thus, ΔS scales as

$$\Delta S \sim \frac{FS_{ref}A\delta}{L_x\zeta\,\kappa_{GM}}\,, \tag{3.22}$$

where δ is the north-south thickness of the diffusive boundary layer. δ can be determined by the local advective-diffusive balance along the intergyre boundary:

$$U_{gyre}\overline{S}_x \approx -(\zeta\,\kappa_{GM}\overline{S}_y)_y\,, \tag{3.23}$$

which gives the scaling $\delta \sim \sqrt{\zeta\kappa_{GM}L_x/U_{gyre}}$. Using Sverdrup balance and continuity to determine U_{gyre}, we finally get

$$\Delta S \sim FS_{ref}L_y\sqrt{\frac{\beta\rho}{\zeta\kappa_{GM}\tau_{yy}}}\,, \tag{3.24}$$

where $\beta \equiv df/dy$ is the derivative of the Coriolis parameter, ρ is the mean density and τ is the windstress at the intergyre boundary. Notice that the resulting ΔS is independent of

the basin width, L_x.

Chapter 4

Components of upper-ocean salt transport by the gyres and the meridional overturning circulation

4.1 Introduction

The global meridional overturning circulation (MOC) is a key component of Earth's climate system, transporting heat northward at all latitudes in the Atlantic basin and regulating ocean uptake of CO_2. In the current regime, Antarctic Intermediate Water (AAIW) is transported northward out of the Southern Ocean in the upper ocean. This AAIW contributes to deep water formation in the North Atlantic, which is enabled by the high salinity (and density) there. North Atlantic Deep Water then spreads southward across the whole ocean and upwells in the Southern Ocean and Indo-Pacific, closing the MOC loop by returning to the North Atlantic as intermediate water (Lumpkin & Speer, 2007). The return flow follows three pathways: the cold route via Drake Passage (Rintoul, 1991), the warm route via the Indonesian Throughflow (ITF) (Gordon, 1985) and the Tasman leakage (Speich

et al., 2002). Water from the Tasman leakage and the ITF flows westward south of Africa, transporting warm salty water into the Atlantic via the Agulhas leakage, and reinforcing Atlantic sinking (Reid, 1961; Gordon, 1986; Nilsson *et al.*, 2013). A supergyre spans the Atlantic, Indian and Pacific oceans, with a western boundary current in the Atlantic sector (Speich *et al.*, 2002; Ridgway & Dunn, 2007). The cold route, the warm route, the Tasman leakage, the supergyre, and the Antarctic Circumpolar Current all exchange salt between the Atlantic and Indo-Pacific sectors. The partition of transport between the warm and cold routes is not well-established, because it is difficult to distinguish the interbasin flow through the Southern Ocean from the large Antarctic Circumpolar Current (ACC) transport (Rintoul, 1991). The goal of this paper is to understand the partition of salt transport among various components of the interbasin salt exchange.

The MOC transports salt northward in the Atlantic, reinforcing deep water formation there (Stommel, 1961). In Cessi & Jones (2017) and Jones & Cessi (2017), we investigated how ocean basin geometry influences the location of deep water formation. As in this paper, we used an ocean-only idealized model in which two narrow continents, running along meridians, divide the domain into two basins of different widths connected by a re-entrant channel south of 52.5°S. At the surface, this model is forced with a zonally uniform wind stress, temperature relaxation and freshwater flux. The basin where deep water is formed (the sinking basin) represents the Atlantic and the other basin (the non-sinking basin) represents the Indo-Pacific. The interbasin transport returns upwelled water from the Indo-Pacific to the Atlantic. In this idealized model, when both continents end south of the zero wind stress curl line (which is at about 42°S), most of the interbasin transport follows the cold route, flowing into the sinking basin from the west. When both continents are the same length, there is a preference for narrow-basin sinking despite zonally uniform surface forcing. This preference is caused by the weaker subpolar gyre in the narrow basin, which allows the MOC's upper branch to transport salt northward more efficiently into the region where deep

water is formed (Jones & Cessi, 2017).

In addition to the preference for narrow-basin sinking, if one continent ends north of the zero wind stress curl line there is a preference for deep water formation in the basin with the short eastern boundary. When the shorter continent ends at 21°S, the effect of continent length overwhelms the effect of basin width. Most of the interbasin transport flows westward south of the shorter continent, proceeding northward into the sinking basin (Cessi & Jones, 2017). The size of this transport is approximately proportional to the width of the non-sinking basin (Jones & Cessi, 2016; Cessi & Jones, 2017). In the work presented here, the size of the interbasin transport is changed by varying the width of the non-sinking basin (which is to the east of the short continent).

This paper seeks to understand the pathway of salt flowing into the north of the sinking basin. Specifically, we wish to quantify the amount of salt transported by the MOC's upper branch versus that transported by the gyres and to understand how this partition depends on the flow configuration. Our approach compares two idealized geometries of an ocean-only general circulation model. Using a pseudostreamfunction for the warm-route interbasin transport flow (described in section 5.2), the domain is broken into a region of open streamlines and a region of closed streamlines (gyres). In section 4.3, it is shown that the salt transport per unit width (p.u.w.) along open streamlines in the sinking basin is larger in the configuration with a larger interbasin transport. The width of the sinking basin also influences the salinity in the sinking region (section 4.4). A summary of our results is provided in section 5.5.

4.2 Methods

The numerical model employed is the Massachusetts Institute of Technology GCM (MITgcm; Marshall *et al.* (1997*b*,*a*)), which integrates the hydrostatic, Boussinesq primitive equations. The domain is a spherical sector, spanning from $-70°$ to $70°$ in latitude and

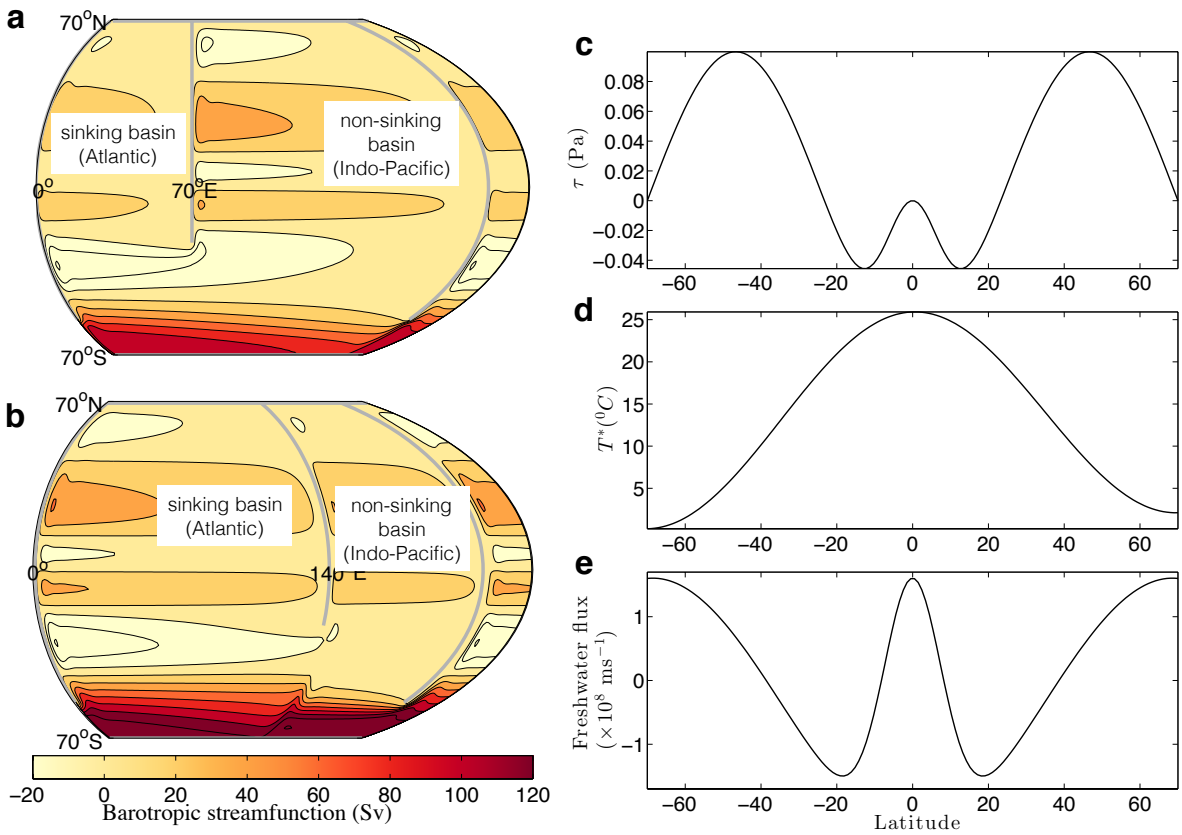

Figure 4.1: The barotropic streamfunction in the geometry of **a** the standard configuration and **b** the exchanged configuration. The grey lines indicate solid boundaries. The domain is 140° in latitude, 210°-periodic in longitude and 4000m deep. The westernmost 20° of the domain is repeated to the right of the figure. In both cases, deep water is formed in the basin to the west of the short continent. **c** Surface wind stress in Pa, **d** the profile of temperature used for temperature relaxation in °C and **e** surface freshwater flux forcing in $\times 10^8\,\mathrm{m\,s^{-1}}$.

covering 210° in longitude, with a horizontal resolution of 1°. The domain consists of two idealized basins of different widths, separated by "continents" one grid point wide aligned along meridians. At the southern edge, a periodic channel of minimum latitudinal width 17.5° connects the basins, as shown in figure 4.1a,b. The bottom is flat and 4000 m deep, except for a sill in the periodic channel, one grid point wide and 1333 m high, located immediately south of the narrow basin's western boundary. There are 32 unequally spaced levels in the vertical, ranging from a minimum spacing of 13.6 m at the top to a maximum of 286 m at the bottom.

The equation of state is linear, with the buoyancy described by:

$$b = g\left[\alpha_T T - \beta_S (S - S_{ref})\right] , \tag{4.1}$$

where $\alpha_T = 2 \times 10^{-4}\,^{\circ}\mathrm{C}^{-1}$, $\beta_S = 7.4 \times 10^{-4}$, and $S_{ref} = 35$. Salinity is given on the practical salinity scale and is therefore presented without units. Temperature is in Celsius.

The model is forced at the surface by zonally-uniform wind stress, τ, freshwater flux, F, and temperature relaxation to a profile, T^*, given by

$$\tau = \tau_{Max}\left(-\cos(3\pi\theta/140) + e^{-\theta^2/\sigma^2}\right) , \tag{4.2}$$

$$F = F_s\left(\cos(7\pi\theta/8\Theta) - 2e^{-(\theta/\Theta).^2/(2\sigma_F^2)}\right) - F_0 , \tag{4.3}$$

$$T^* = T_{eq}\left(\cos(\pi\theta/140)^2 + 0.1e^{-(\theta/2\Theta - 1)^2}\right) , \tag{4.4}$$

where θ is latitude in degrees, $\tau_{Max} = 0.1\,\mathrm{N m^{-2}}$, $\sigma = 10^{\circ}$, $F_s = 2 \times 10^{-8}\,\mathrm{m\,s^{-1}}$, $\sigma_F = 0.128$, $\Theta = 60^{\circ}$, and $T_{eq} = 25^{\circ}\mathrm{C}$ (see figure 4.1c,d,e). The relaxation time-scale for the surface temperature is 10 days. The freshwater flux is multiplied by the negative reference salinity, $-S_{ref}$, in order to obtain the salt flux into the ocean. The constant F_0 is chosen so that the net freshwater flux into the ocean is zero. Thus, the average salinity of the ocean remains constant at $S_{ref} = 35$.

Baroclinic eddies are parameterized using the Gent-McWilliams advective form (Gent & McWilliams, 1990) and the Redi (1982) isopycnal tracer mixing with equal mixing coefficients set to $\kappa_{iso} = 500\ \mathrm{m^2\ s^{-1}}$. The Gent-McWilliams scheme is implemented using the boundary value problem framework described by Ferrari *et al.* (2010). The Redi tensor changes to horizontal diffusion in regions of weak stratification, as described by Danabasoglu & McWilliams (1995). The vertical diffusivity is set to $2 \times 10^{-5}\,\mathrm{m^2\,s^{-1}}$ in the interior, increasing to $10^{-2}\,\mathrm{m^2\,s^{-1}}$ at the surface over a depth of 20m to model the mixed layer. Each simulation was run for at least 3000 years, until equilibrium was reached.

In this paper, we compare two geometries, both with a long continent that extends from 70° to -52.5° and a short continent that extends from 70° to -21°. In the "standard" geometry, the short continent is to the east of the narrow basin and in the "exchanged" geometry the short continent is to the east of the wide basin. The exchanged geometry was initialized with sinking in the basin to the east of the short continent. Nonetheless in both configurations, sinking occurs in the basin to the west of the short continent, which represents the Atlantic. The other basin represents the Indo-Pacific. We choose these geometries because they have the same total MOC transport, but different salinities in the north of the sinking basin despite longitudinally independent forcing.

As a measure of the overturning circulation, we use the zonally integrated residual overturning streamfunction (ROC; cf. Wolfe & Cessi 2015), defined as

$$\psi(y,\tilde{b}) \equiv \frac{1}{T}\int_0^T\int_0^{L_x}\int_{-H}^{0} v^\dagger \mathcal{H}\left[b(x,y,z,t)-\tilde{b}\right]\,\mathrm{d}z\,\mathrm{d}x\,\mathrm{d}t\,, \tag{4.5}$$

where $v^\dagger$ is the Eulerian plus parameterized eddy velocity in the meridional direction, H is the total depth, L_x is the width of the basin, T is the averaging timescale (100yrs is chosen here), and $\mathcal{H}$ is the Heaviside function. The ROC streamfunction, ψ, denotes the zonally integrated transport of water above $b=\tilde{b}$.

The zonally-averaged thickness-weighted salinity anomaly (as described in Young 2012) is defined as

$$\hat{S}(y,\tilde{b}) \equiv \frac{1}{T}\int_0^T\frac{1}{L_x}\int_0^{L_x}\left\{\frac{\int_{-H}^{0}(S-S_{ref})\mathcal{H}\left[b(x,y,z,t)-\tilde{b}\right]\,\mathrm{d}z}{\int_{-H}^{0}\mathcal{H}\left[b(x,y,z,t)-\tilde{b}\right]\,\mathrm{d}z}\right\}\mathrm{d}x\,\mathrm{d}t\,. \tag{4.6}$$

The quantity $\hat{S}$ is zonally averaged at constant buoyancy, so it can be contoured in the same panel as the ROC.

In figure 4.2, ψ (black contours) and $\hat{S}$ (filled color contours) are remapped into

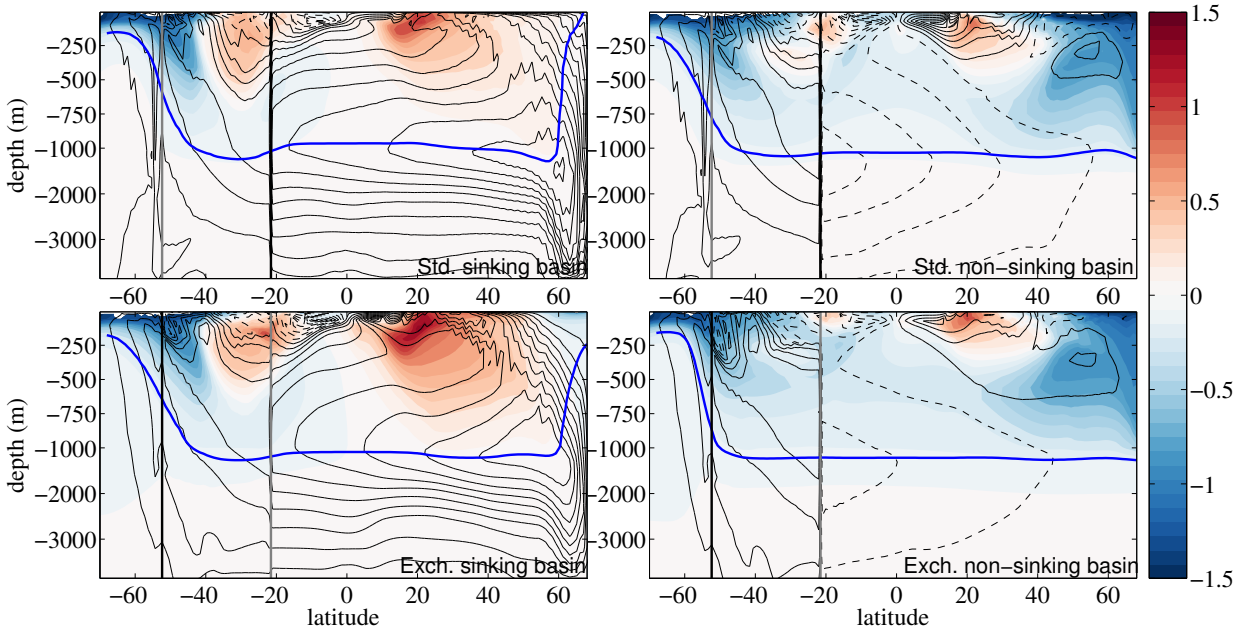

Figure 4.2: The zonally-averaged thickness-weighted salinity, $\hat{S}$, in PSU, (color contours, spacing 0.1PSU) and the ROC, ψ (black contours, spacing 2Sv), in the sinking basin (left) and the non-sinking basin (right), of the standard (top) and exchanged (bottom) geometries. ψ and $\hat{S}$ are defined in (5.6) and (4.6). Dashed lines represent negative values of ψ. The vertical black line denotes the end of the continent to the east of the narrow basin and the vertical grey line denotes the end of the continent to the east of the wide basin. South of $-21°$, the zonal integral of ψ is over the whole width of the domain. The thick blue contour denotes the zonally-averaged height of the isopycnal $b_m = 0.0066\,\mathrm{m\,s^{-2}}$, which bounds the upper branch of the MOC from below.

z-coordinates using the zonal-mean isopycnal height, which is defined as

$$\mathcal{Z}(y,\tilde{b}) \equiv -\frac{1}{T}\int_0^T \frac{1}{L_x}\int_0^{L_x}\int_{-H}^{0} \mathcal{H}\left[b(x,y,z,t)-\tilde{b}\right] \mathrm{d}z\,\mathrm{d}x\,\mathrm{d}t. \tag{4.7}$$

Because of longitudinal buoyancy gradients, the zonally-averaged remapping (5.7) distorts the vertical extent of the mixed layer.

The isopycnal $b_m = 0.0066\,\mathrm{m\,s^{-2}}$ (thick blue lines in figure 4.2) divides the upper and lower branches of the circulation: it passes close to the maximum of the ROC in both geometries. It is well known that heat and salt transports are defined up to a constant (Boccaletti *et al.*, 2005). Here we define the advective component of salt transport as $v^\dagger(S - Sref)$. Below the isopycnal b_m, the salinity is approximately uniform and equal to S_{ref} (see

figure 4.2), so with this definition almost all salt transport occurs above b_m.

In both geometries, some interbasin transport flows eastward south of the long continent (the cold route) and some flows westward south of the short continent (the warm route). It is difficult to separate the components of interbasin exchange flow from the ACC, because the ACC transport is so much larger than the interbasin transport. Hence, in order to find the transport of the cold route and the warm route in each geometry, we remove the rotational component of the flow from the depth integrated velocity above b_m. The vertically integrated velocity is divided into a component associated with velocity potential ϕ and a component associated with streamfunction ξ, giving

$$\begin{aligned} \int_{\zeta(b_m)}^{0} \mathbf{u}^\dagger \, \mathrm{d}z = &\quad \mathbf{U}_\phi + \mathbf{U}_\xi \\ \mathbf{U}_\phi = &\quad \frac{\partial \phi}{\partial x}\hat{\mathbf{i}} + \frac{\partial \phi}{\partial y}\hat{\mathbf{j}}, \\ \mathbf{U}_\xi = &\quad \frac{\partial \xi}{\partial y}\hat{\mathbf{i}} - \frac{\partial \xi}{\partial x}\hat{\mathbf{j}}, \end{aligned} \tag{4.8}$$

where $\mathbf{u}^\dagger$ is the horizontal Eulerian plus parameterized eddy velocity, $\mathbf{U}_\phi$ is the divergent component of the depth-integrated horizontal flow and $\mathbf{U}_\xi$ is the rotational component of the depth-integrated horizontal flow.

The velocity potential, ϕ, is plotted in figure 4.3, together with the transport across various sections, obtained by integrating $\mathbf{U}_\phi$ in the horizontal. The diapycnal upwelling across b_m, indicated by the symbol $\odot$, is calculated by taking the divergence of the horizontal velocity, depth integrated above b_m. Integrating U_ϕ meridionally south of each continent shows that about 70% of the interbasin transport enters the sinking basin via the warm route, with the remainder entering via the cold route.

Because the flow above $b_m = 0.0066\,\mathrm{m\,s^{-2}}$ is horizontally divergent, it is not possible to describe it with a streamfunction. Instead, two pseudostreamfunctions of this flow are

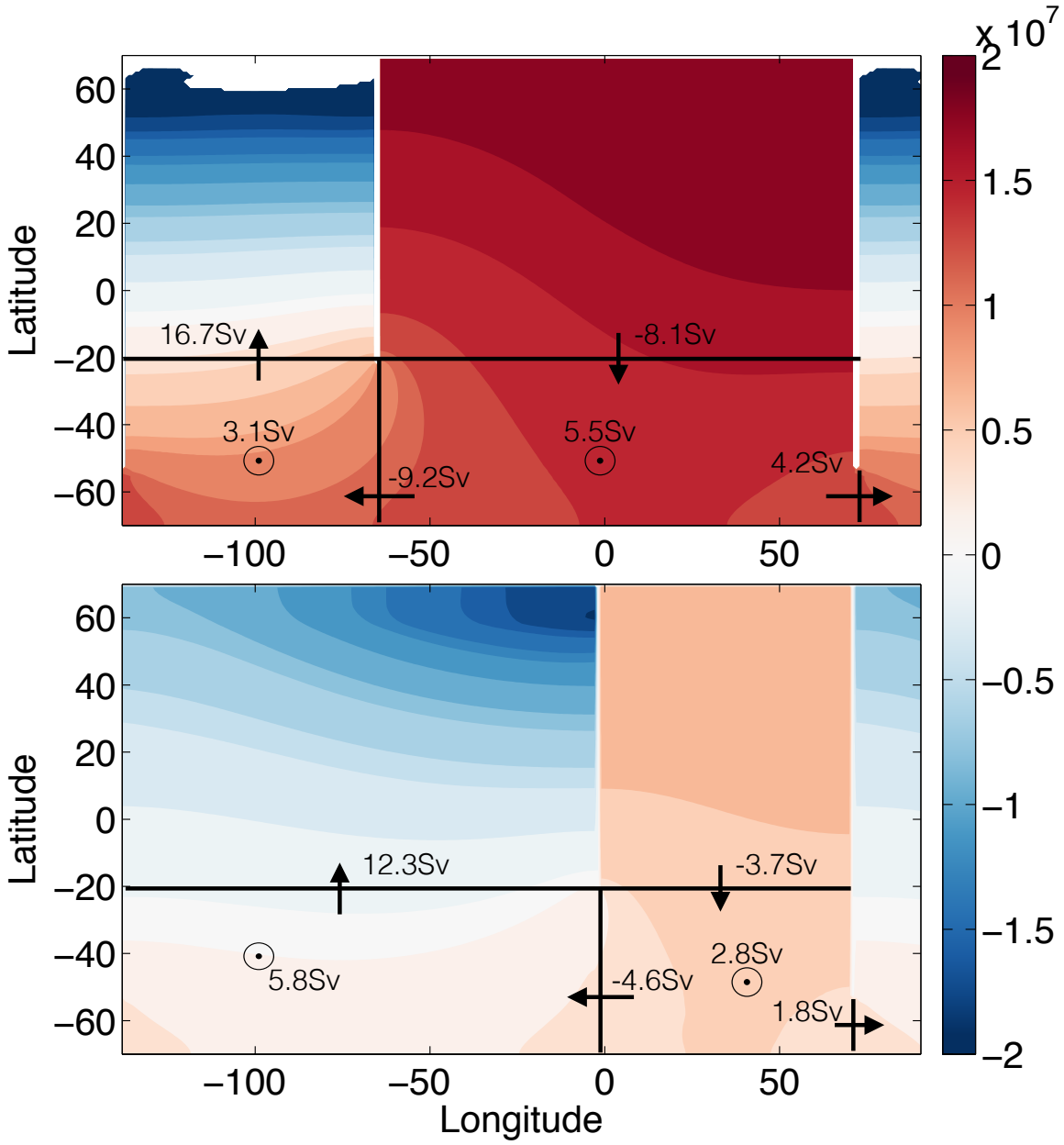

Figure 4.3: Velocity potential ϕ (m^3/s; color contours) for the Eulerian plus parameterized eddy velocity, vertically integrated above $b_m = 0.0066\,m\,s^{-2}$, and the transport of the diapycnal component of the flow across various sections for the standard case (top) and the exchanged case (bottom). $\odot$ indicates upwelling across the isopycnal $b_m = 0.0066\,m\,s^{-2}$. The westernmost 20° of the domain is repeated to the right of the figure.

defined as

$$\chi_i(x,y) = -\frac{1}{T}\int_0^T \int_{-L}^{y} \int_{\zeta(x,\hat{y},b_m)}^{0} u^\dagger(x,\hat{y},z,t)\ \mathrm{d}z\, d\hat{y}\, \mathrm{d}t\,, \tag{4.9}$$

and

$$\chi_v(x,y) = \frac{1}{T}\int_0^T \int_{0}^{x} \int_{\zeta(x,\hat{y},b_m)}^{0} v^\dagger(\hat{x},y,z,t)\ \mathrm{d}z\, d\hat{x}\, \mathrm{d}t + \chi_0(y)\,, \tag{4.10}$$

where $\zeta(x,y,b_m)$ is the depth of isopycnal $b_m = 0.0066\,\mathrm{m\,s^{-2}}$ and, $y = -L$ is the southern boundary of the domain. The function χ_0 is defined as

$$\chi_0(y) = \begin{cases} \chi_i(x=0, y=y_c) & \text{for } y > y_c \\ \chi_i(x=0,y) & \text{for } y < y_c \end{cases} \tag{4.11}$$

where $y = y_c$ is the end of the long continent: this choice of χ_0 allows the pseudostreamfunctions to be easily compared. Speich *et al.* (2001, 2002) use a pseudostreamfunction similar to χ_i (integrated above a depth level rather than a density level) to show the pathways of the warm route, the cold route and the Tasman leakage in realistic-geometry ocean-only models.

Neither pseudostreamfunction describes the two-dimensional transport above b_m completely: in particular, neither pseudostreamfunction shows the cold route. However, each pseudostreamfunction characterizes some aspects of the flow well: χ_i more accurately describes the warm-route interbasin transport (figure 4.4) and χ_v more accurately describes the northward transport of the warm-route interbasin flow plus channel upwelling in the sinking basin (figure 4.5).

4.3 Components of salt transport

The top panel of figure 4.6 shows the salinity anomaly, vertically and zonally averaged above $b_m = 0.0066\,\mathrm{m\,s^{-2}}$. The "sinking region" is defined as the band of latitudes where the zonally integrated diapycnal velocity is negative and larger in magnitude than $5\,\mathrm{m^2\,s^{-1}}$. This

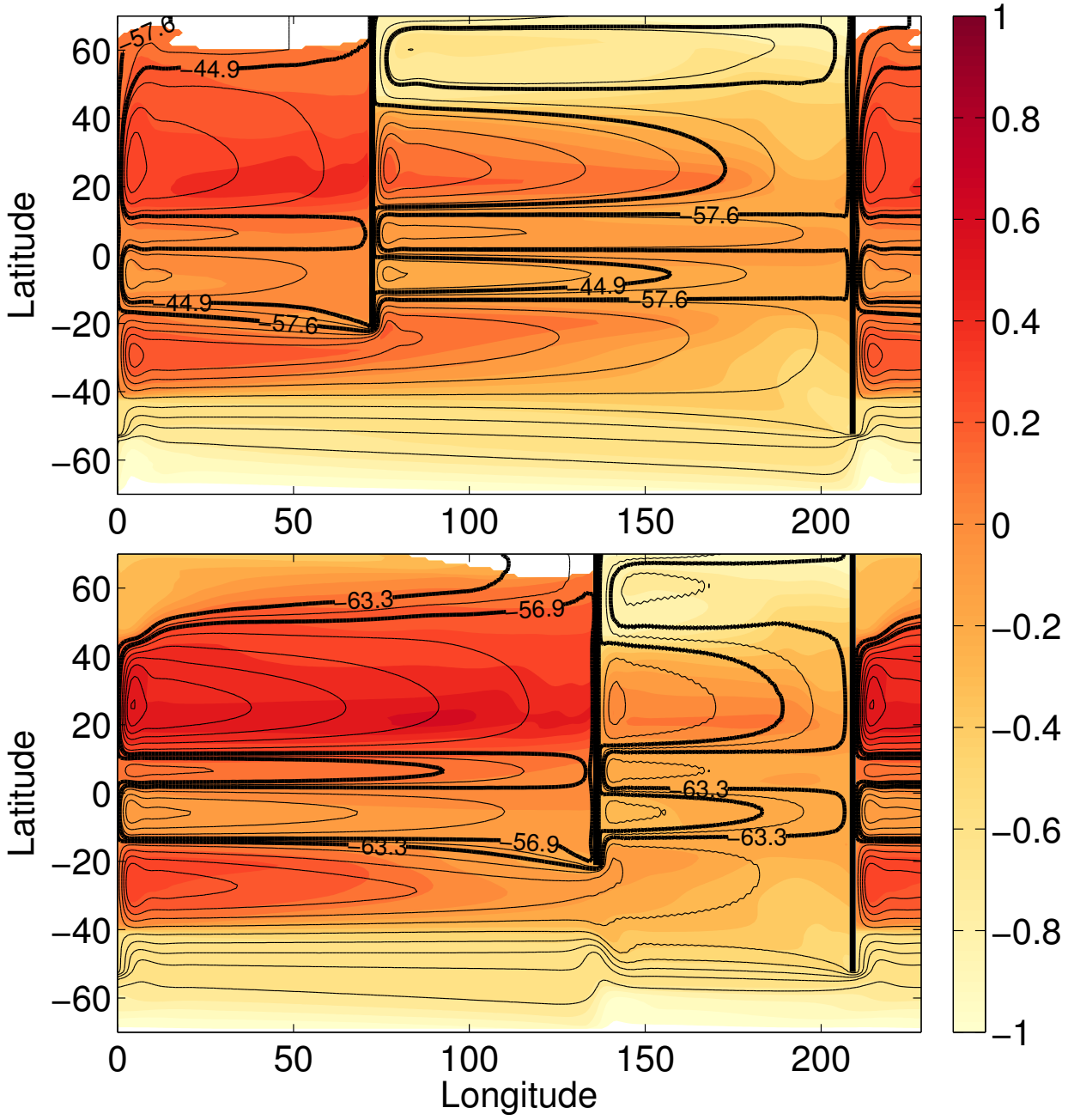

Figure 4.4: Salinity anomaly, referenced to 35PSU, vertically averaged above surface $b_m = 0.0066\,\mathrm{m\,s^{-2}}$ (color) and contours of pseudostreamfunction χ_i, as defined in (4.9) (black contours) for the standard geometry (top) and the exchanged geometry (bottom). The thick black contours bound the region of open streamlines. These streamlines represent the warm-route interbasin flow. The transport along open streamlines is 12.7 Sv in the standard geometry and 6.4 Sv in the exchanged geometry. The isopycnal $b_m = 0.0066\,\mathrm{m\,s^{-2}}$ outcrops in the white area. The westernmost 20° of the domain is repeated to the right of the figure.

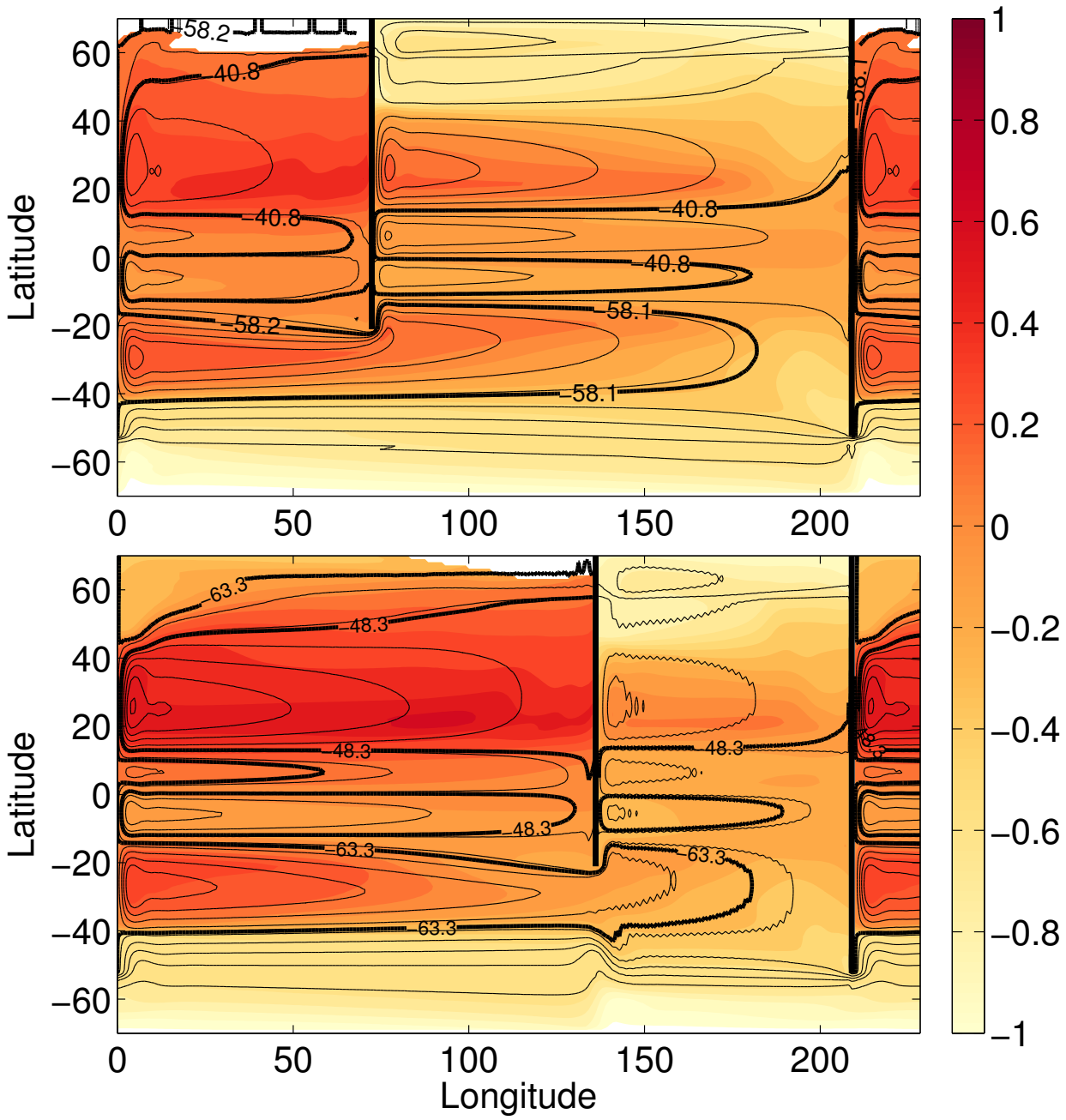

Figure 4.5: Salinity anomaly, referenced to 35PSU, vertically averaged above surface $b_m = 0.0066\,\mathrm{m\,s^{-2}}$ (color) and contours of pseudostreamfunction χ_v, as defined in (4.10) (black contours) for the standard geometry (top) and the exchanged geometry (bottom). The thick black contours bound the region of open streamlines. These streamlines represent the warm-route interbasin transport plus channel upwelling. The residual transport along open streamlines is 17.3 Sv in the standard geometry and 15 Sv in the exchanged geometry. The isopycnal $b_m = 0.0066\,\mathrm{m\,s^{-2}}$ outcrops in the white area. The westernmost 20° of the domain is repeated to the right of the figure.

region lies between 59° and 66° in the standard geometry and about 2° farther south in the exchanged geometry (see yellow and grey boxes in the top panel of figure 4.6).

In the sinking region, the zonally-averaged salinity anomaly is higher for the standard geometry (compare the red lines in the yellow and grey boxes in the top panel of figure 4.6), despite similar ROC transports in the Northern Hemisphere (compare red lines in the bottom panel of figure 4.6). Between the equator and 50°, the zonally-averaged salinity anomaly is higher for the exchanged geometry (compare the red lines in the top panel of figure 4.6). Here, we will address how the components of salt transport produce the zonally-averaged salinity distribution.

The difference in salinity between the two configurations can also be observed in the zonally-averaged thickness-weighted salinity, $\hat{S}$. In the sinking region, the salinity difference between configurations is very surface intensified (compare color contours north of 50° in the top left and bottom left panels of figure 4.2), and north of 60° the ROC streamfunction is much larger near the surface of the standard case (compare black contours in the top left and bottom left panels of figure 4.2). South of 50° in the sinking basin, the difference appears to be spread over the whole depth above b_m (compare color contours in the top left and bottom left panels of figure 4.2). However, at least some of the salinity difference at depth is caused by the deeper subtropical gyre in the sinking basin of the exchanged case, which is simply due to basin width and does not indicate any differences in the depth-integrated meridional salt transport p.u.w above b_m.

We divide the contours of χ_i and χ_v into "open streamlines" and "closed streamlines", a partition that is often performed on 2D flows (c.f. Childress & Gilbert 2008, chap. 5). For χ_i, "open streamlines" are contours beginning in the non-sinking basin and ending in the sinking basin: these contours characterize the warm-route interbasin transport above b_m. The residual transport along these streamlines is 12.7 Sv for the standard geometry and 6.4 Sv for the exchanged geometry. The interbasin transport is smaller for a narrower

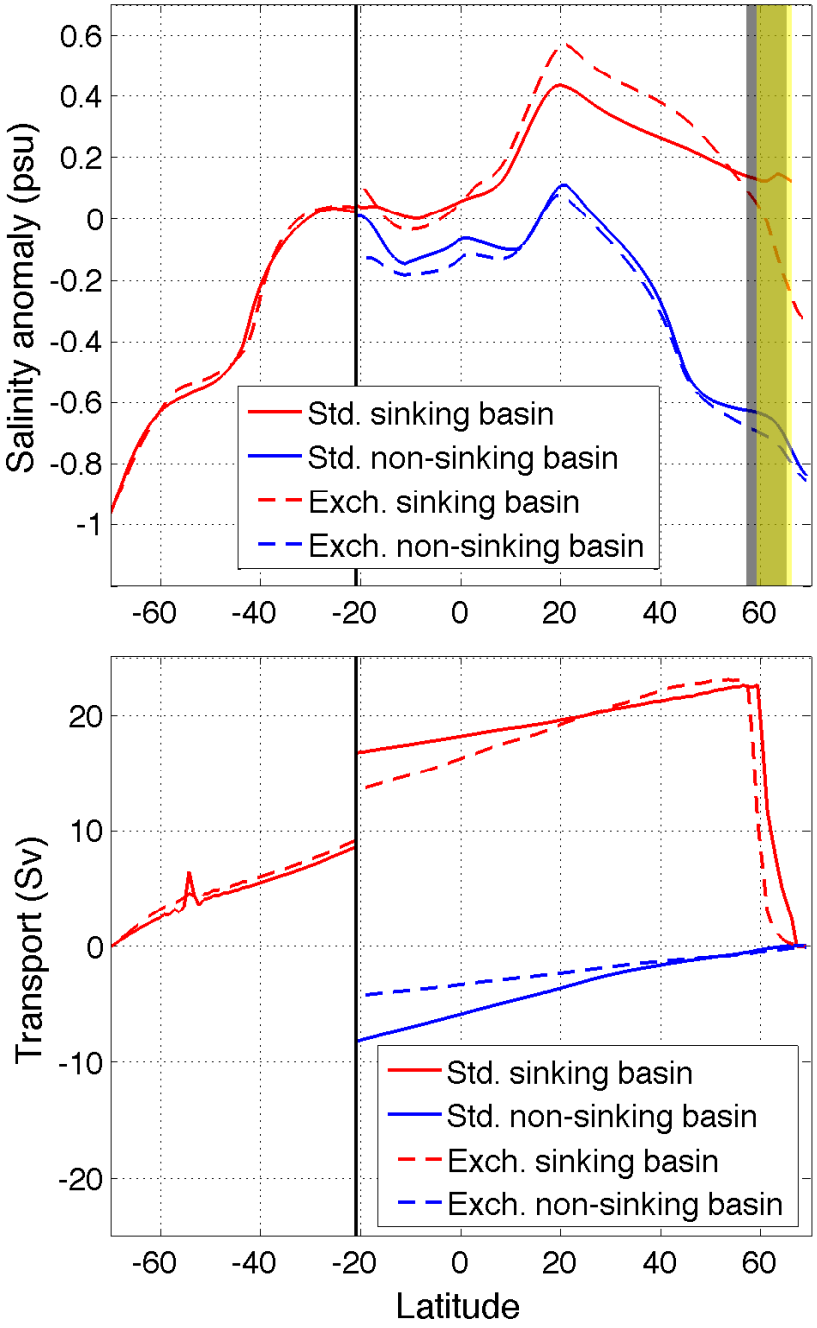

Figure 4.6: Salinity anomaly, referenced to 35PSU, depth and zonally averaged above $b_m = 0.0066\,\mathrm{m\,s^{-2}}$ and across each basin (top) and the residual transport above $b_m = 0.0066\,\mathrm{m\,s^{-2}}$ in each basin (bottom). South of $-21°$, the zonal integral is taken across all longitudes. The yellow box indicates the sinking region for the standard geometry and the grey box indicates the sinking region for the exchanged geometry. The black vertical line denotes the end of the short continent.

non-sinking basin, because there is less upwelling to feed it (Allison, 2009; Jones & Cessi, 2016). The thick black lines in figure 4.4 bound the region of open streamlines of χ_i.

For χ_v, "open streamlines" are contours beginning outside the Northern Hemisphere of the sinking basin and ending in the north of the sinking basin: these contours characterize the residual transport of the warm-route interbasin flow plus channel upwelling. The residual transport along these streamlines is 17.3 Sv for the standard geometry and 15 Sv for the exchanged geometry. The thick black lines in figure 4.5 bound the region of open streamlines of χ_v.

To characterize the salt pathway into the north of the sinking basin, the total meridional salt transport above b_m, G_{tot}, is decomposed into the following components: 1) the meridional advective transport in the area of open streamlines, A_{open}; 2) the meridional diffusive transport in the area of open streamlines, D_{open}; 3) the meridional advective transport in the area of closed streamlines, A_{closed}; and 4) the meridional diffusive transport in the area of closed streamlines D_{closed}. In summary we have

$$G_{tot}(y) = A_{open}(y) + D_{open}(y) + A_{closed}(y) + D_{closed}(y)\,, \tag{4.12}$$

where,

$$A_{open}(y) = \int_{\chi_w}^{\chi_e} \frac{1}{T} \int_0^T \int_{\zeta(b_m)}^0 v^\dagger (S - S_{ref})\, dz\, dt\, dx\,, \tag{4.13}$$

$$D_{open}(y) = \int_{\chi_w}^{\chi_e} \frac{1}{T} \int_0^T \int_{\zeta(b_m)}^0 \kappa_{iso} \left(S_y - \frac{b_y}{b_z} S_z \right) dz\, dt\, dx\,, \tag{4.14}$$

$$A_{closed}(y) = \int_{x_w}^{x_e} \frac{1}{T} \int_0^T \int_{\zeta(b_m)}^0 v^\dagger (S - S_{ref})\, dz\, dt\, dx - A_{open}\,, \tag{4.15}$$

$$D_{closed}(y) = \int_{x_w}^{x_e} \frac{1}{T} \int_0^T \int_{\zeta(b_m)}^0 \kappa_{iso} \left(S_y - \frac{b_y}{b_z} S_z \right) dz\, dt\, dx - D_{open}\,, \tag{4.16}$$

$\chi_{w,e}$ are the westernmost and easternmost open streamlines, $x_{w,e}$ are the western and eastern sides of the sinking basin, and κ_{iso} is the Redi coefficient.

The total salt transport p.u.w. above b_m, G_{tot}/L_x (where L_x is the width of the basin), is more relevant than G_{tot} for determining the salinity in the north of the sinking basin. The total salt transport p.u.w. above b_m is plotted for each basin of both configurations in figure 4.7a. In the sinking basin the salt transport p.u.w. is larger in the standard geometry than in the exchanged geometry (compare the red lines north of $-21°$ in figure 4.7a). North of $40°$, the difference between configurations widens (compare red lines at $50°$ in figure 4.7a). In the exchanged case, the lower salt transport p.u.w. reduces the salinity of the sinking region and increases the salinity at mid-latitudes (compare red lines in the top panel of figure 4.6).

The black line in figure 4.7a represents the total salt transport p.u.w by the whole water column: in equilibrium this transport is determined by the surface freshwater flux. Extra northward salt transport in the upper branch of the MOC is balanced by extra southward salt transport in the lower branch, so in the sinking basin the southward salt transport below b_m is larger in the standard geometry (not shown).

In the non-sinking basin the salt transport p.u.w. in the upper branch is independent of geometry (compare the blue lines in figure 4.7a) and very similar to the salt transport p.u.w. in the whole water column (the black line in figure 4.7a). This leads to similar salinities in the non-sinking basin of both geometries (compare blue lines in the top panel of figure 4.6). Henceforth we will focus on the salt transport in the sinking basin, which is different between configurations.

Figure 4.7b shows the meridional advective salt transport in the area of open streamlines of χ_i, A_{open}/L_x, (black lines) and the meridional salt transport in the area of closed streamlines of χ_i, $(A_{closed} + D_{closed})/L_x$ (green lines) in the sinking basin, both normalized by basin width for ease of comparison. Figure 4.7c shows the same salt transports, but for streamlines of χ_v. The diffusive component in the area of open streamlines, D_{open}, is not shown because it is negligible. Because the streamlines of χ_i and χ_v are depth and time averaged, salt can be advected across them by the baroclinic component of the flow if the

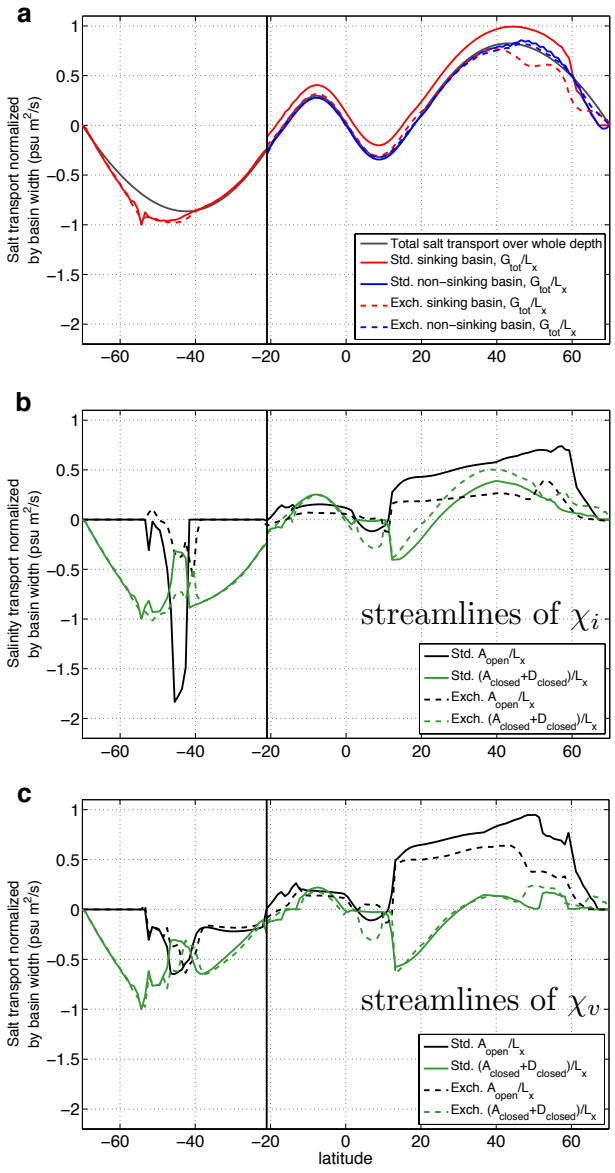

Figure 4.7: **a** Total salt transport, vertically integrated over the whole water column (black line) and vertically integrated above $b_m = 0.0066\,\mathrm{m\,s^{-2}}$ (red and blue lines), zonally averaged across each basin north of $-21°$; south of $-21°$, the zonal integral is taken across all longitudes. **b** A_{open} for χ_i (black lines) and $A_{closed} + D_{closed}$ for streamlines of χ_i (green lines), in the sinking basin north of $-21°$ (normalized by the basin width for ease of comparison) and in the whole domain south of $-21°$ (normalized by the domain width for ease of comparison). **c** A_{open} for streamlines of χ_v (black lines) and $A_{closed} + D_{closed}$ for χ_v (green lines), in the sinking basin north of $-21°$ (normalized by the basin width for ease of comparison) and in the whole domain south of $-21°$ (normalized by the domain width for ease of comparison). The quantities plotted in this figure are defined in (4.12) to (4.16).

velocity and salinity are correlated in the vertical.[1] The meridional salt transport in the area of open streamlines is well-approximated with the meridional salt transport by the vertically and zonally integrated velocity above b_m in the region of open streamlines (see appendix 4.A for details).

At most latitudes north of $-21°$, the salt transport p.u.w. in the area of open streamlines, A_{open}/L_x, is larger in the standard case than in the exchanged case for both χ_i and χ_v (compare black lines in figure 4.7b,c). This indicates that in the standard configuration the higher total salt transport p.u.w. is effected by the larger warm-route interbasin transport (the difference between the red lines in figure 4.7a is similar to the difference between the black lines in figure 4.7b). The larger salt transport p.u.w. north of $-21°$ increases the vertically and zonally-averaged salinity above b_m north of $60°$ (compare red lines in the top panel of figure 4.6). Thus, it is likely that strengthening the warm-route transport would increase the salinity in the north of the sinking basin.

For pseudostreamfunction χ_v, the salt transport p.u.w. in the area of closed streamlines is independent of width (compare green lines in figure 4.7c). This is consistent with the following scaling from appendix A2 of Jones & Cessi 2017:

$$\Delta S \sim F S_{ref} L_y \sqrt{\frac{\beta\rho}{\zeta(b_m)\kappa_{iso}\tau_{yy}}}\,, \tag{4.17}$$

where ΔS is the difference in salinity between two adjacent gyres, $\beta \equiv df/dy$ is the derivative of the Coriolis parameter, ρ is the mean density, L_y is the meridional length scale of the basin, and τ is the windstress at the intergyre boundary. Notice that ΔS is independent of the basin width, L_x.

[1] If the flow were entirely barotropic (i.e. 2-D) above b_m, the advective transport across a closed streamline would be zero.

4.4 Salt budget between $40°$ and $50°$

The salt transport north of $40°$ is particularly important for setting the salinity of the sinking region. For the exchanged case, there is a drop in the northward salt transport p.u.w. in the sinking basin, going from $40°$ to $50°$: this drop is less prominent in the standard case (compare red lines in figure 4.7a). For pseudostreamfunction χ_v,[2] the open-streamline salt transport p.u.w. in the exchanged configuration also shows this drop (compare black lines in figure 4.7c). The aim of this section is to understand why the salt transport p.u.w decreases between $40°$ and $50°$ in the exchanged configuration: in this latitude band salt must be lost from the region of open streamlines more efficiently than in the standard configuration.

The following budget describes the components of the flow into and out of the area of open streamlines between $40°$ and $50°$ (outlined in green in figure 4.8), depth integrated above b_m. The black dashed lines in figure 4.8 represent the easternmost and westernmost open streamlines. Assuming the model is in a steady state, conservation of salt in each region gives

$$\mathcal{F}_{no} + \mathcal{D}_{no} - C_{out} + C_{in} + A_{open}(40°) - A_{open}(50°) = 0\,, \tag{4.18}$$

where $\mathcal{F}_{no}$ is the area-integrated salt transport at the surface, $\mathcal{D}_{no}$ is the area-integrated diapycnal salt transport across b_m, C_{in} is the salt transport into the region across the easternmost open streamline and C_{out} is the salt transport out of the region across the westernmost open streamline. Area integrals are over the region of open streamlines between $40°$ and $50°$. Table 4.1 gives the value of each term in both configurations. All salt transports are normalized by the basin width at $40°$ for ease of comparison.

In the standard case, the cross-streamline salt transports, C_{in} and C_{out}, the area-integrated surface salt flux, $\mathcal{F}_{no}$, and the area-integrated diapycnal flux, $\mathcal{D}_{no}$, are all an

[2]The results in this section are for pseudostreamfunction χ_v. Using the pseudostreamfunction χ_i gives the same qualitative differences between the standard configuration and the exchanged configuration.

Table 4.1: Salt transport budget for the open streamline region of streamfunction χ_v between 40° and 50° in the sinking basin. Figure 4.8 shows a schematic of this region. The salt transports are normalized by the basin width at 40°, $L_x(40°)$.

Parameter	Standard case ($m^2\,s^{-1}$)	Exchanged case ($m^2\,s^{-1}$)
$C_{out}/L_x(40°)$	0.0090	0.032
$\mathcal{F}_{no}/L_x(40°)$	−0.013	−0.038
$\mathcal{D}_{no}/L_x(40°)$	0.018	−0.022
$C_{in}/L_x(40°)$	0.044	−0.23
$A_{open}(40°)/L_x(40°)$	0.84	0.61
$A_{open}(50°)/L_x(40°)$	0.80	0.29

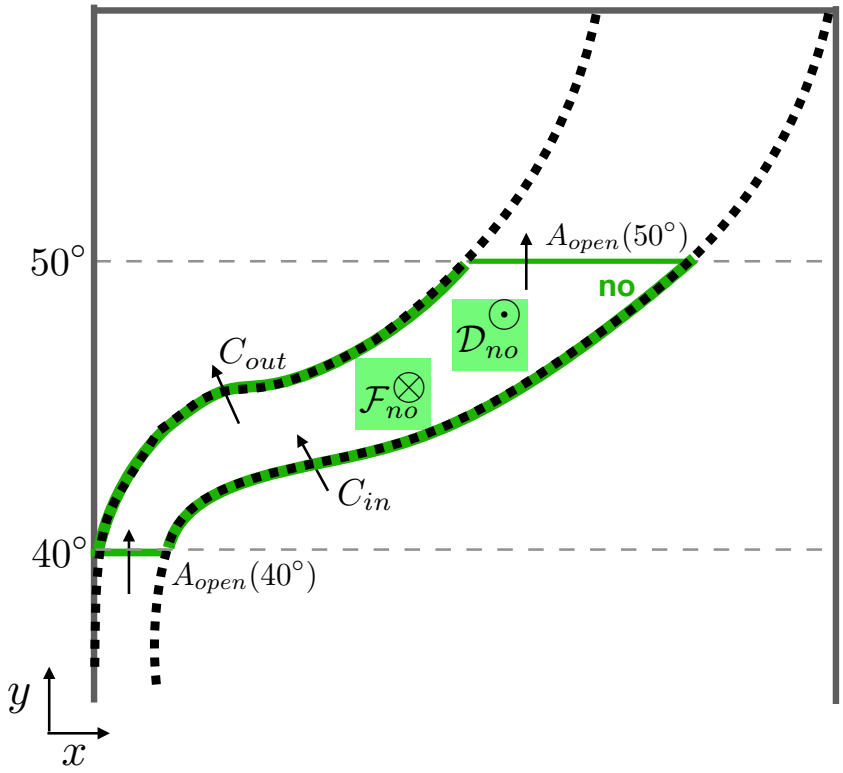

Figure 4.8: Schematic of salt transport into the region of open streamlines between 40° and 50°. The solid grey lines represent the boundaries of the domain and the black dotted lines represent the easternmost and westernmost open streamlines. C_{in} is the horizontal cross-streamline salt transport above the isopycnal b_m into the region of open streamlines (the area bounded by green lines) from the south. $\mathcal{F}_{no}$ is the salt transport into the region of open streamlines at the surface and $\mathcal{D}_{no}$ is the diapycnal salt transport across b_m into the region of open streamlines. C_{out} is the horizontal cross-streamline salt transport above the isopycnal b_m out of the region of open streamlines into the north. A_{open} is the meridional salt transport in the region of open streamlines.

order of magnitude smaller than the along-streamline salt transport as measured by A_{open}. Therefore the advective salt transports at 40° and 50° are very similar (solid black line in figure 4.7c). In the exchanged case, the salt transport across the easternmost open streamline, C_{in}, is more negative, and $A_{open}(50°) \approx A_{open}(40°)+C_{in}$. The meridional salt transport along open streamlines in the exchanged case is smaller at 50° (dashed black line in figure 4.7c), because some salt is transported southward into the subtropical gyre.

The salt transport across the easternmost open streamline, C_{in}, is dominated by southward advection of salt in the Ekman layer. In the exchanged case, the easternmost open streamline turns eastward at a lower latitude than in the standard case (compare the thick black contour marked 40.8 in the top panel of figure 4.5 with the thick black contour marked 48.3 in the bottom panel of figure 4.5). The subpolar gyre western boundary current, which is stronger in a wider basin (Jones & Cessi, 2017), forces the open streamlines to turn away from the boundary earlier in the exchanged case. Between 40° and 50°, the Ekman transport is southward, perpendicular to the easternmost open streamline in the exchanged configuration (thick black contour marked -48.3 in the bottom panel of figure 4.5), but not in the standard configuration (thick black contour marked -40.8 in the top panel of figure 4.5). Thus, between 40° and 50°, the southward cross-streamline Ekman transport of salt is smaller in the standard configuration.

The normalized cross-streamline salt transport, $C_{in}/L_x(40°)$, freshens the open-streamline flow between 40° and 50° in the sinking basin of the exchanged configuration, reducing the northward along-streamline salt transport. This intensifies the gradients of zonally-averaged salinity above b_m (as shown by the red dashed line in the top panel of figure 4.6). North of 60°, the fresher surface in the sinking basin of the exchanged case pushes the ROC stream-function below about 200m depth (black contours in the bottom left panel of figure 4.2).

4.5 Summary and Discussion

In this paper, we study the transport of salt in an idealized global ocean model consisting of two basins of different widths connected by a re-entrant channel. We compare two versions of this model, one with the short continent to the east of the narrow basin (the "standard" geometry) and one with the short continent to the east of the wide basin (the "exchanged" geometry). Deep water is formed in the basin to the west of the short continent in both configurations. 70% of the interbasin transport flows westward south of the short continent (through the warm route) and it has twice the strength in the standard geometry than in the exchanged geometry. We define two different pseudostreamfunctions: one in which the open streamlines represent the warm-route interbasin transport and one in which the open streamlines represent the warm-route interbasin transport plus the channel upwelling. The cold route is not represented in either of these peseudostreamfunctions. We divide the salt transport entering the sinking basin above a mid-depth isopycnal, into the salt transport by flow along open streamlines and the salt transport in the area of closed streamlines. This method gives an approximation of the net salt transport between basins. The salt transport between basins is otherwise difficult to obtain, because it is difficult to separate the interbasin exchange flow (which is order 5Sv) from the ACC (which is order 40Sv above b_m).

In the sinking basin, the northward salt transport per unit width is larger in the standard configuration than in the exchanged configuration. The warm-route interbasin transport carries salt northward more efficiently in the standard configuration, leading to higher salinity in the north of the sinking basin. In the exchanged configuration, the wider sinking basin leads to a larger salt transport out of the region of open streamlines at about 40°, consistent with Jones & Cessi (2017). This salt transport out of the region of open streamlines also reduces salinity in the north of the sinking basin in the exchanged case.

This study suggests that the total salt transport from the Indo-Pacific to the Atlantic

is primarily effected by the interbasin exchange associated with the ITF and the Tasman leakage, rather than by the gyral flow. Increasing the interbasin transport is likely effective at raising the salinity of the North Atlantic. Higher salinity could act to stabilize the MOC, which is enabled by high surface densities in the North Atlantic. The strength of the Agulhas leakage, which is fed by the ITF and Tasman leakage, responds to upstream conditions (van Sebille *et al.*, 2009) and to changes in the Southern Hemisphere Westerlies (Gordon, 1986; Biastoch *et al.*, 2009). If variations in the strength of the Agulhas leakage are associated with variations in salt (and heat) transport, they may drive MOC variability. In particular, climate models predict that Southern Hemisphere Westerlies will move southward and intensify over the next century, leading to an increase in the Agulhas leakage on decadal timescales (Biastoch & Böning, 2013), and to larger northward salt transport by the warm-route.

Acknowledgements

CSJ and PC are supported by the National Science Foundation under Grants 446 No. OCE-1258887 and OCE-1634128. Computational resources were provided by XSEDE consortium, which is supported by National Science Foundation Grant ACI-1053575.

Chapter 4, in full, has been submitted for publication in the Journal of Physical Oceanography 2018. Jones, C. S.; Cessi, Paola, American Meteorological Society, 2018.

4.A Salt advection by the velocity, vertically integrated above b_m and zonally integrated in the area of open streamlines

In this paper, we assume that the vertically and zonally averaged salt transport in the area of open streamlines, A_{open}, is a approximately equal to the vertically and zonally averaged salt transport by the vertically and zonally integrated along-streamline flow. This is equivalent to assuming that the salt transport by the vertically and zonally integrated flow above b_m in the area of open streamlines is much larger than the salt transport by the baroclinic component of the flow above b_m, or by zonal variations of the depth-averaged velocity in this area. In order to confirm our assumption, we decompose A_{open} into: 1) the salt advection by the vertically and zonally averaged meridional velocity above b_m between open streamlines, and 2) a residual due to correlations between salinity and velocity in the vertical and zonal directions. This gives

$$A_{open}(y) = X_{open}(y)S_{open}(y) + A^{(res)}_{open}(y)\,, \tag{4.19}$$

$$= \left[\int_{\chi_w}^{\chi_e}\int_{\zeta(b_m)}^{0} v^\dagger\,dz\,dx\right]\left[\frac{\int_{\chi_w}^{\chi_e}\int_{\zeta(b_m)}^{0}(S-S_{ref})\,dz\,dx}{\int_{\chi_w}^{\chi_e}\int_{\zeta(b_m)}^{0}dz\,dx}\right] + A^{(res)}_{open}\,, \tag{4.20}$$

where X_{open} is the meridional residual transport along open streamlines above b_m, S_{open} is the zonally and vertically averaged salinity in the area of open streamlines above b_m and $A^{(res)}_{open}$ is the remaining meridional salt transport in the area of open streamlines above b_m.

The salt transport, $X_{open}S_{open}$, normalized by the basin width, is shown in figure 4.9. North of $-21°$, most of the salt advection p.u.w. in the region of open streamlines, A_{open}, is explained by the vertically and zonally-averaged meridional velocity above b_m and between open streamlines $X_{open}S_{open}$ (compare black and pink lines in figure 4.9). The salt transport in the region of open streamlines, A_{open}, is well-approximated with the meridional advection

by the vertically and zonally integrated velocity in that region.

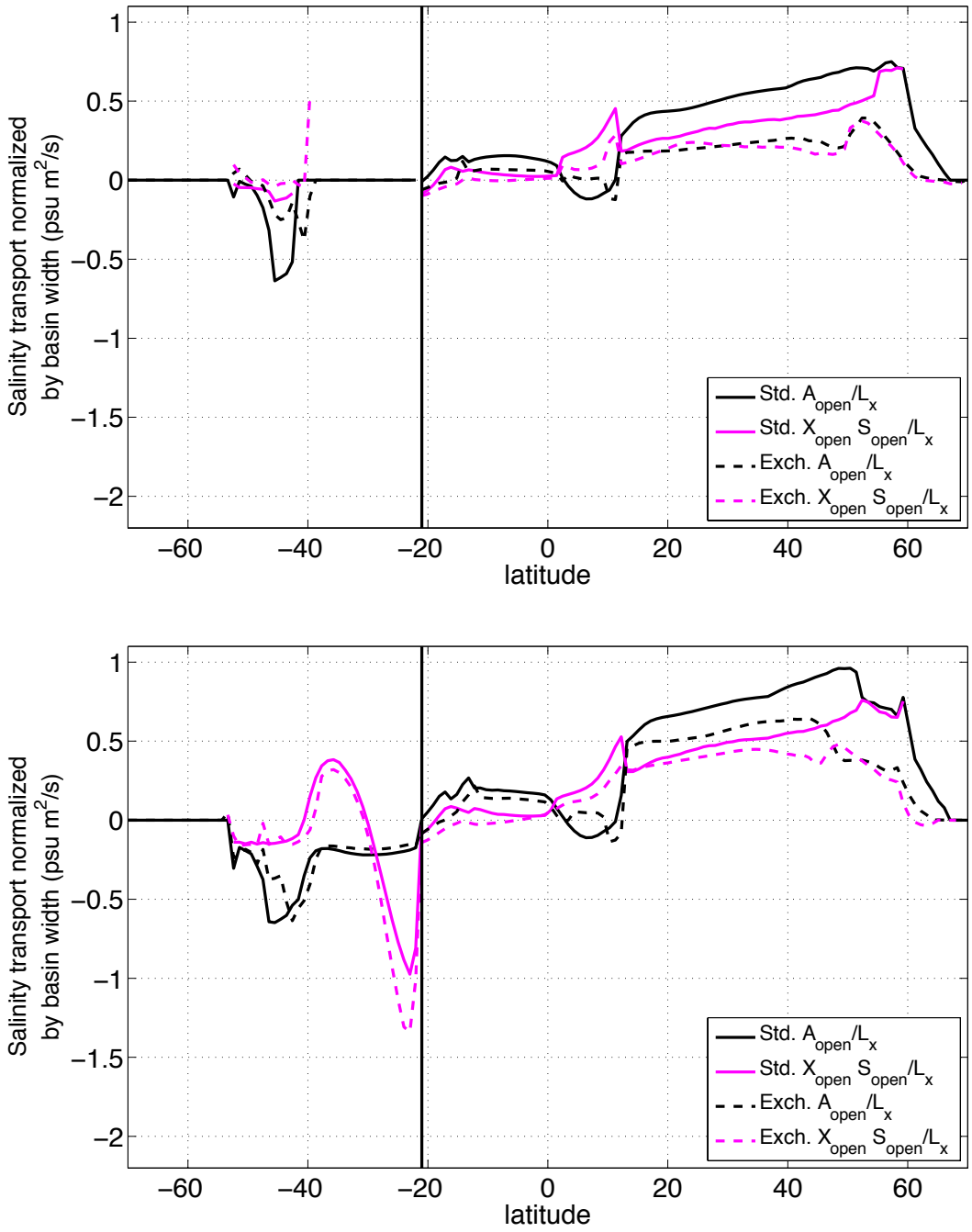

Figure 4.9: A_{open} (black lines) and $X_{open}S_{open}$ (pink lines), in the sinking basin north of $-21°$ (normalized by the basin width for ease of comparison) and in the whole domain south of $-21°$ (normalized by the domain width for ease of comparison) for streamlines χ_i (top) and streamlines χ_v (bottom). The black vertical line denotes the end of the short continent.

Chapter 5

Connecting the two cells of the meridional overturning circulation

5.1 Introduction

In the zonal average, the meridional overturning circulation (MOC) appears as two separate cells: a mid-depth cell and an abyssal cell. The upper branch of the mid-depth cell transports Antarctic Intermediate Water (AAIW) northward in the upper ocean, which is eventually transported into the North Atlantic, where it sinks to form North Atlantic Deep Water (NADW). NADW then flows southward and upwells in the Southern Ocean. From there, it flows northward as AAIW again, closing the mid-depth cell. In the abyssal cell, Antarctic Bottom Water (AABW) water is formed in the far south, flows northward in the abyss and diapycnally upwells to about 2000m in the interior of the basins. This water returns southward, upwelling along isopycnals once it enters the Southern Ocean. After it arrives near the surface, it closes the abyssal cell by sinking again. A schematic of these cells is shown in the left panel of figure 1.1. Observations indicate that the cells overlap in the deep Atlantic with some mixing between AABW and NADW there (e.g. Lumpkin & Speer 2007; Marshall & Speer 2012; Talley 2013).

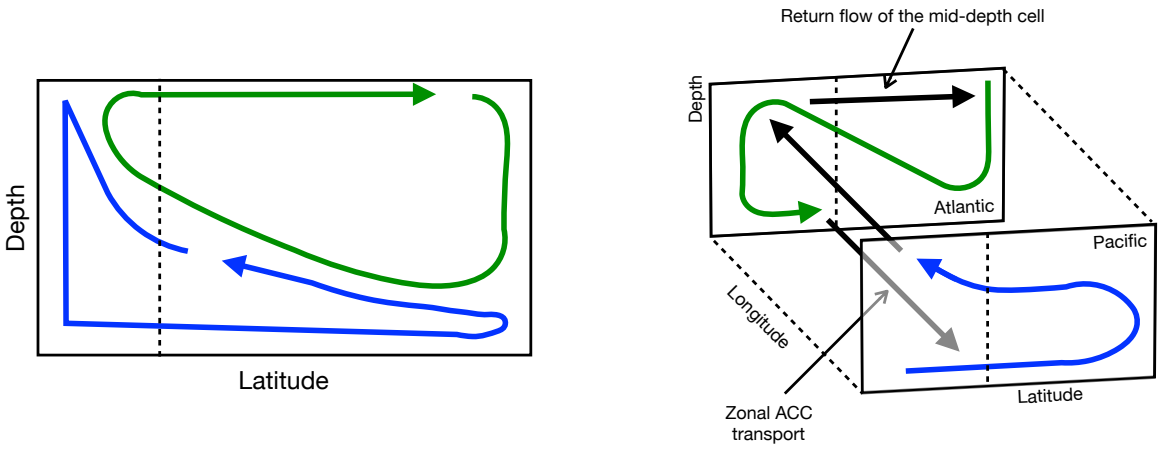

Figure 5.1: The mid-depth cell (green line) and abyssal cell (blue line) in the zonal average (left). A schematic of the continuous loop (right), in which deep water is formed in the North Atlantic, flows southward and upwells in the Southern Ocean, where it feeds AABW formation (green line). This AABW then enters the Indo-Pacific and upwells across isopycnals (blue line) before returning to the Atlantic. The vertical dashed line indicates the latitude of the southern tip of Africa. Adapted from Thompson *et al.* (2016)

Warren (1990) suggested that a portion of the NADW that upwells in the Southern Ocean flows southward to form AABW, and that an equal amount of AABW upwells in the Indo-Pacific and returns to the Atlantic as intermediate water (as shown in the right panel of figure 5.1). This paradigm has become more popular recently (Lumpkin & Speer, 2007; Talley, 2013; Thompson *et al.*, 2016; Ferrari *et al.*, 2017). In particular, Ferrari *et al.* (2017) find that NADW is recycled through the abyss in an idealized two-basin model. From the zonally averaged plots of the residual overturning circulation commonly used to characterize the MOC, it is difficult to estimate the relative transport of the mid-depth cell, the abyssal cell and the continuous loop. Here, our goal is to understand the pathway of the circulation and to examine how the transport is partitioned between these three routes in a simplified model of the world ocean.

Thompson *et al.* (2016) formulated a four-layer conceptual model of the global MOC in a domain with two basins connected by a re-entrant channel. This model predicts that more NADW is recycled through the abyss in some parameter regimes. Specifically, the circulation is two-cell-like when two conditions are met: 1) the diapycnal diffusivity is reduced

above 2000m and 2) more than 10Sv of deep water is formed in the north of the narrow basin. The MOC is thought to have been in this two-cell configuration during the Last Glacial Maximum (Ferrari *et al.*, 2014), whereas observations suggest that most NADW is recycled through the abyss before returning to the North Atlantic.

AABW generally forms in areas with a high sea-ice concentration, which likely reduces heat, salt and gas exchange with the atmosphere. Hence, water that is recycled through the abyssal Pacific may retain some of the properties it acquired at the surface of the North Atlantic. Water that simply recirculates in the abyssal cell loses such properties. Tracer observations show that about 25% of the water in the abyssal Pacific was last ventilated in the North Atlantic (Gebbie *et al.*, 2010), but it is unclear what pathway this water follows between the two basins.

In this work, we investigate the pathways of the overturning. In particular we examine how much water takes the continuous path versus the two-cell loop in an idealized-geometry primitive-equation model. The idealized model is described in section 5.2. In section 5.3, a budget of the residual transport in this model indicates that about 40% of deep water formed in the narrow basin follows the continuous path. In section 5.4, transit-time of buoyancy through the continuous path is found using an adjoint tracer experiment. Summary and discussion are given in section 5.5.

5.2 Methods

The numerical model employed is the Massachusetts Institute of Technology GCM (MITgcm; Marshall *et al.* (1997*b*,*a*)), which integrates the hydrostatic, Boussinesq primitive equations. The domain is a spherical sector, spanning from $-70°$ to $70°$ in latitude and covering $210°$ in longitude, with a horizontal resolution of $1°$. The domain consists of two idealized basins of different widths, separated by "continents" one grid point wide aligned along meridians: one continent extends from $-52.5°$ to $70°$ and one extends from $-35°$ to

70°. At the southern edge, a periodic channel of minimum latitudinal width 17.5° connects the basins, as shown in figure 5.2a. The bottom is flat and 4000 m deep, except for a sill in the periodic channel, one grid point wide and 1333 m high, located immediately south of the narrow basin's western boundary. There are 32 unequally spaced levels in the vertical, ranging from a minimum spacing of 13.6 m at the top to a maximum of 286 m at the bottom.

The equation of state is linear, with the buoyancy described by:

$$b = g\left[\alpha_T T - \beta_S (S - S_{ref})\right] , \tag{5.1}$$

where $\alpha_T = 2 \times 10^{-4}\,^{\circ}\mathrm{C}^{-1}$, $\beta_S = 7.4 \times 10^{-4}$, and $S_{ref} = 35$. Salinity is given on the practical salinity scale and is therefore presented without units.

The model is forced at the surface by zonally-uniform wind stress, τ, and freshwater flux, F, given by

$$\tau = \tau_{Max}\left(-\cos(3\pi\theta/140) + e^{-\theta^2/\sigma^2} + e^{-(\theta+47)^2/(2\sigma^2)}\right) , \tag{5.2}$$

$$F = F_s\left(\cos(7\pi\theta/8\Theta) - 2e^{-(\theta/\Theta).^2/(2\sigma_F^2)}\right) - F_0 , \tag{5.3}$$

where θ is latitude in degrees, $\tau_{Max} = 0.1\,\mathrm{N\,m^{-2}}$, $\sigma = 10°$, $F_s = 2 \times 10^{-8}\,\mathrm{m\,s^{-1}}$, $\sigma_F = 0.128$, and $\Theta = 60°$ (see figure 5.2b,c). The freshwater flux is multiplied by the negative reference salinity, $-S_{ref}$, in order to obtain the salt flux into the ocean. The constant F_0 is chosen so that the net freshwater flux into the ocean is zero.

North of $-68°$, the model surface is relaxed to a profile, T^*, given by

$$T^* = T_{eq}\left(\cos(\pi\theta/140)^{1.8} + 0.2e^{-(\theta/2\Theta-1)^2}\right) , \tag{5.4}$$

where $T_{eq} = 25°\mathrm{C}$ (see figure 5.2d) (temperature is in Celsius). The relaxation time-scale for the surface temperature is 10 days. South of $-68°$ surface heat flux out of the ocean is

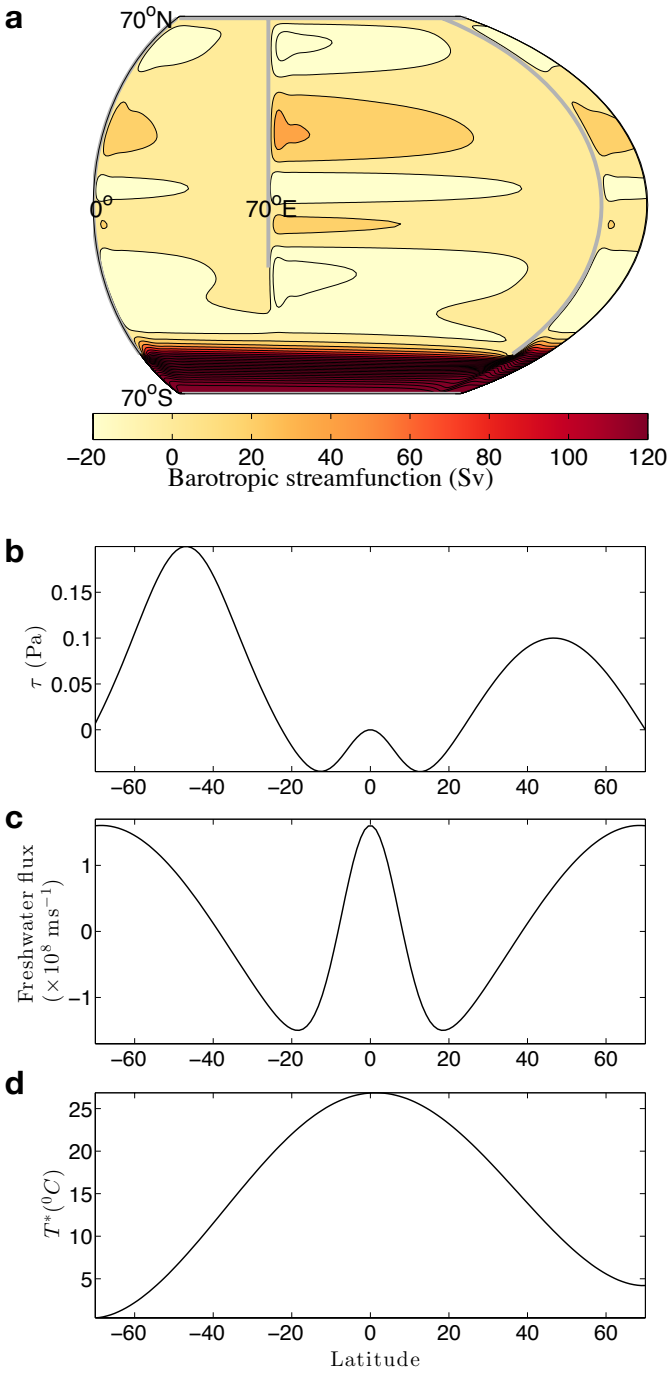

Figure 5.2: **a** The barotropic streamfunction. The grey lines indicate solid boundaries. The domain is 140° in latitude, 210°-periodic in longitude and 4000m deep. The westernmost 20° of the domain is repeated to the right of the figure. **b** Surface wind stress in Pa, **c** surface freshwater flux forcing in $\times 10^8\,\mathrm{m\,s^{-1}}$ and **d** the profile of temperature used for temperature relaxation in °C.

prescribed at a rate of 100 W/m^2. This is a crude representation of the heat flux out of the ocean under sea ice, as described by Ferrari *et al.* (2014).

Baroclinic eddies are parameterized using the Gent-McWilliams advective form (Gent & McWilliams, 1990) and the Redi (1982) isopycnal tracer mixing with equal mixing coefficients set to $\kappa_{GM} = 500$ m^2 s^{-1}. The Gent-McWilliams scheme (GM henceforth) is implemented using the boundary value problem framework described by Ferrari *et al.* (2010). The Redi tensor is changed to horizontal diffusion in regions of weak stratification, as described by Danabasoglu & McWilliams (1995). The vertical diffusivity is given by

$$\kappa_v = 2 \times 10^{-5} + 2 \times 10^{-4} \frac{\left[1 - \tanh\left(\frac{z+2000}{200}\right)\right]}{2} + 10^{-2} \frac{\left[1 + \tanh\left(\frac{z+30}{30}\right)\right]}{2}; \tag{5.5}$$

i.e. $2 \times 10^{-5}\,\mathrm{m^2\,s^{-1}}$ in the interior, increasing to $10^{-2}\,\mathrm{m^2\,s^{-1}}$ at the surface to model the mixed layer and increasing to $2 \times 10^{-4}\,\mathrm{m^2\,s^{-1}}$ below 2000m. The simulation was run for at least 5000 years, until equilibrium was reached.

As a measure of the overturning circulation, we use the zonally integrated residual overturning streamfunction (ROC; cf. Wolfe & Cessi 2015), defined as

$$\psi(y, \tilde{b}) \equiv \frac{1}{T_0} \int_0^{T_0} \int_0^{L_x} \int_{-H}^{0} v^\dagger \mathcal{H}\left[b(x, y, z, t) - \tilde{b}\right] \,\mathrm{d}z\,\mathrm{d}x\,\mathrm{d}t\,, \tag{5.6}$$

where $v^\dagger$ is the Eulerian plus parameterized eddy velocity in the meridional direction, H is the total depth, L_x is the width of the basin, T_0 is the averaging timescale (100yrs is chosen here), and $\mathcal{H}$ is the Heaviside function. The ROC streamfunction, ψ, denotes the zonally integrated transport of water above $b = \tilde{b}$.

In figure 5.3, the ROC streamfunction (filled color contours) is remapped into z-coordinates using the zonal-mean isopycnal height, which is defined as

$$\mathcal{Z}(y, \tilde{b}) \equiv -\frac{1}{T_0} \int_0^{T_0} \frac{1}{L_x} \int_0^{L_x} \int_{-H}^{0} \mathcal{H}\left[b(x, y, z, t) - \tilde{b}\right] \mathrm{d}z\,\mathrm{d}x\,\mathrm{d}t. \tag{5.7}$$

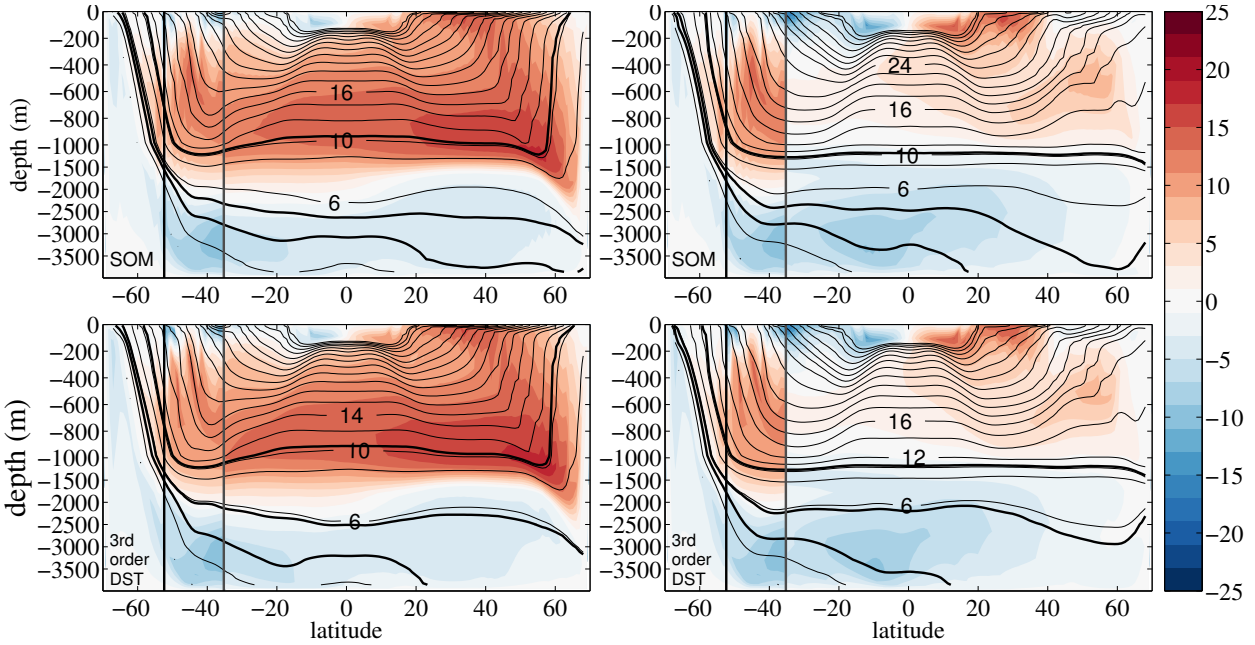

Figure 5.3: The ROC, ψ, in Sverdrups (color contours, spacing 2Sv), and $b^\sharp \times 10^3\,\mathrm{m\,s^{-2}}$, the buoyancy of the surface whose average depth is $\mathcal{Z}$ (black contours) in the sinking basin (left) and the non-sinking basin (right) using Prather (1986)'s SOM scheme (top) and the 3rd order DST scheme (bottom). The vertical black line denotes the end of the long continent and the vertical grey line denotes the end of the short continent. South of $-35°$ (the latitude of the short continent), the zonal integral of ψ is over the whole width of the domain. The thick black contours denote the isopycnals b_a, b_b, and b_c, which bound the four portions of the MOC.

In z-coordinates, it is useful to define the modified buoyancy $b^\sharp(y,z)$ (figure 5.3, black contours), where $\mathcal{Z}\left[y, b^\sharp(y,z)\right] = z$.

Because of longitudinal buoyancy gradients, the zonally-averaged remapping (5.7) distorts the vertical extent of the mixed layer. Values of $b^\sharp$ higher than $40 \times 10^{-3}\,\mathrm{m\,s^{-2}}$ are not plotted because the contours would be too close together.

The top panels of figure 5.3 show ψ, calculated using Prather (1986)'s Second Order Moments (SOM) advection scheme. This scheme has very little implicit diffusion, but no adjoint for it is currently available in the MITgcm. Therefore, we also used the 3rd order Direct Space Time (DST) advection scheme (e.g. Hundsdorfer *et al.* 1995): ψ for this scheme is shown in the bottom panels of figure 5.3. ψ is very similar in the two advection schemes, but there is slightly more overturning with the 3rd order DST scheme, because of the increased numerical mixing. For the SOM scheme, 17.4Sv of deep water (i.e. NADW)

is formed in the north of the narrow basin (the maximum of ψ in the mid-depth cell in the top-left panel of figure 5.3 is 17.4Sv) and for the 3rd order DST scheme, 17.8Sv of deep water is formed in the north of the narrow basin (the maximum of ψ in the mid-depth cell in the bottom-left panel of figure 5.3 is 17.8Sv).

For diagnostic purposes, in both simulations, the domain is divided into four density classes: 1) above b_a, 2) between b_b and b_a, 3) between b_c and b_b, and 4) below b_c. Class 1 represents the upper branch of the mid-depth cell, class 2 the lower branch of the mid-depth cell, class 3 the upper branch of the abyssal cell and class 4 the lower branch of the abyssal cell. For SOM, $b_a = 0.0104\,\mathrm{m\,s^{-2}}$, $b_b = 0.0056\,\mathrm{m\,s^{-2}}$ and $b_c = 0.005\,\mathrm{m\,s^{-2}}$, whereas for 3rd order DST $b_a = 0.0104\,\mathrm{m\,s^{-2}}$, $b_b = 0.0058\,\mathrm{m\,s^{-2}}$ and $b_c = 0.005\,\mathrm{m\,s^{-2}}$.

5.3 Pathway of the residual overturning circulation

Figures 5.4 and 5.5 show budgets of the residual velocity in our idealized model with the SOM advection scheme and with the 3rd order DST scheme respectively. In addition to the four density classes described above, the ocean is divided in the north-south direction at 35°S, and in the east-west direction at each continental boundary. We find the net residual transport across all sections connecting the domain's subdivisions. Through a Helmholtz decomposition of the flow into a velocity potential and a streamfunction, we find that the former is associated with the net transport forced by the cross-isopycnal divergence. The cross-isopycnal transport is calculated from the divergence of the horizontal residual transport above each isopycnal.

In both panels of figures 5.4 and 5.5, the green arrows show the continuous loop, and the red arrows show the remaining residual transport. We identify which flow is part of the continuous loop as follows.

The transport of the continuous loop passes from density class 2 to density class 3 on its way to the abyss and from density class 3 to density class 2 on its way back to the surface.

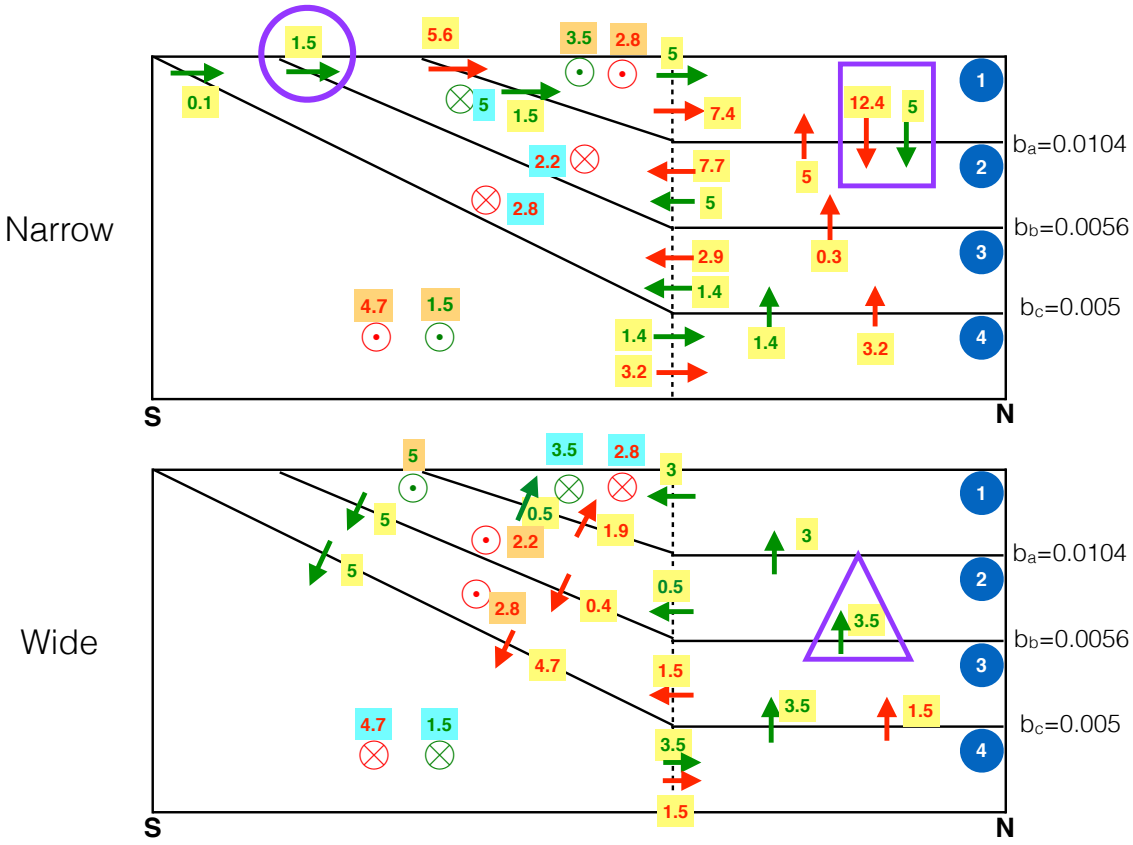

Figure 5.4: Budget of the residual circulation in Sverdrups from the simulation that uses Prather (1986)'s SOM scheme. The dashed line is at $-35°$. Numbers in blue circles indicate the density class of each layer. All other numbers indicate the residual transport between regions. Numbers with a light blue background denote the residual transport out of a sector in the zonal direction ($\otimes$) and numbers with an orange background denote the residual transport into a sector in the zonal direction ($\odot$). The green arrows show the residual transport of the continuous loop and the red arrows show all remaining transport. The arrows in the purple rectangle denote the sinking in the north of the narrow basin, some of which upwells before it reaches $-35°$. The arrow in the purple triangle denotes upwelling from density class 2 to density class 3 in the wide basin. The arrow in the purple circle denotes upwelling from density class 2 to density class 3 in the narrow sector of the channel.

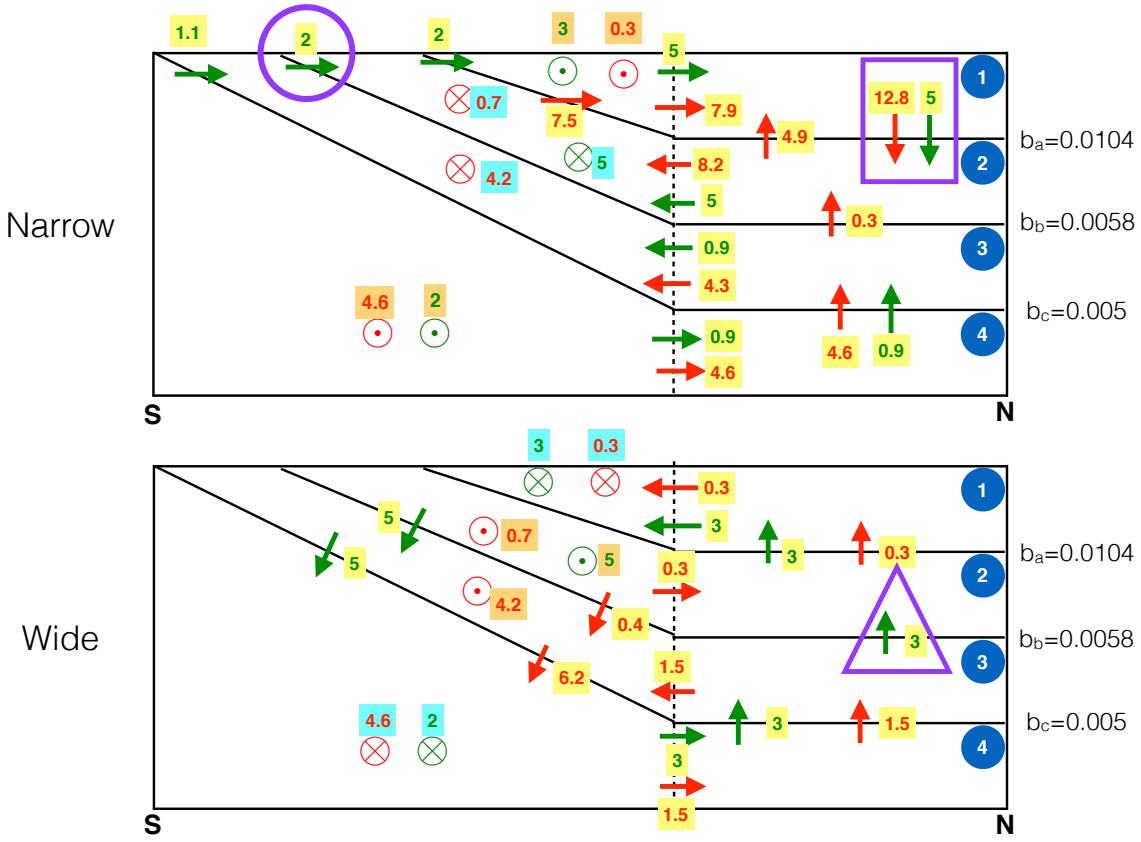

Figure 5.5: [Budget of the residual circulation in Sverdrups from the simulation that uses the 3rd order DST scheme. The dashed line is at $-35°$. Numbers in blue circles indicate the density class of each layer. All other numbers indicate the residual transport between regions. Numbers with a light blue background denote the residual transport out of a sector in the zonal direction ($\otimes$) and numbers with an orange background denote the residual transport into a sector in the zonal direction ($\odot$). The green arrows show the residual transport of the continuous loop and the red arrows show all remaining transport. The arrows in the purple rectangle denote the sinking in the north of the narrow basin, some of which upwells before it reaches $-35°$. The arrow in the purple triangle denotes upwelling from density class 2 to density class 3 in the wide basin. The arrow in the purple circle denotes upwelling from density class 2 to density class 3 in the narrow sector of the channel.

For both advection schemes, 0.3Sv upwells from density class 3 to density class 2 north of $-35°$ in the narrow basin (top panels of figures 5.4 and 5.5). This transport does not reach the surface, but returns to the abyss via the wide sector of the channel: it is not part of the continuous loop. Hence, for both advection schemes the maximum possible transport of the continuous loop is 5Sv (5Sv is the sum of the transport in the purple triangle plus the transport in the purple circle in each of figures 5.4 and 5.5).

The flow from density class 3 to density class 2 in the wide basin (purple triangles in the bottom panels of figures 5.4 and 5.5) follows the continuous loop: this transport has all passed through the abyss and continues upwelling into density class 1. Similarly, the flow from density class 3 to density class 2 in the narrow sector (purple circles in the top panels of figures 5.4 and 5.5) originates in the abyss, whether it enters density class 3 via diapycnal upwelling in the narrow basin or via northward Ekman transport in the narrow sector of the channel. If the flow from density class 3 to density class 2 in the narrow sector crosses isopycnal b_b near the surface, then it likely continues into density class 1, in which case it is considered to be part of the continuous loop.

To determine the location of the diapycnal transports across b_a, b_b and b_c, we examine the zonally integrated diapycnal velocity (figures 5.6 and 5.7). For each isopycnal b_a, b_b and b_c, we mark the zonally averaged latitude of the outcrop and of the 200m depth isocontour. 200m is chosen because it is the averaged mixed-layer depth south of $-52°$. In the narrow sector of the channel, over 3Sv of positive diapycnal transport across b_b and b_c occurs poleward of the mixed-layer latitude. The shallow location of this transport suggests that in the narrow sector of the channel, the cross isopycnal transport from density class 4 to density class 3 contributes to the cross isopycnal transport from density class 3 to density class 2 (the transports in the purple circles in figures 5.4 and 5.5). At least some of the latter appears to continue northward into density class 1, so here it is considered to be part of the continuous loop. Hence, we estimate that the continuous-loop transport is 5Sv for both

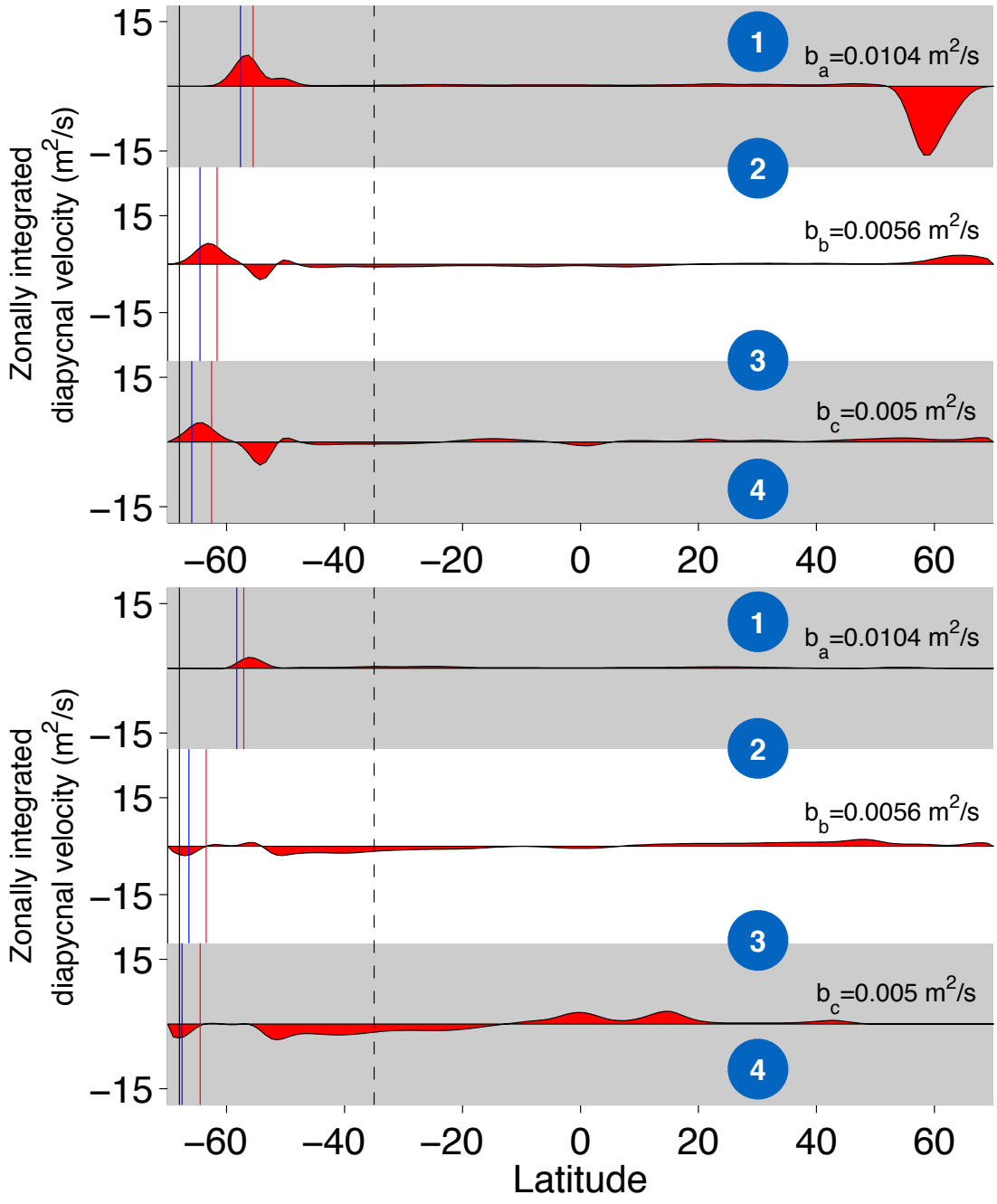

Figure 5.6: The zonally integrated diapycnal velocity in the narrow sector (top) and in the wide sector (bottom). The vertical black dashed line indicates the end of the short continent and the vertical black solid line marks −68°. The blue vertical line marks the outcrop of each buoyancy surface, zonally averaged over the appropriate sector. Similarly, the red vertical line indicates the zonally averaged latitude (over each sector) where the isopycnal depth is 200m, i.e. the approximate depth of the mixed layer in the channel. The numbers in the blue circles indicate the density class above and below each isopycnal. This figure is for the SOM advection scheme.

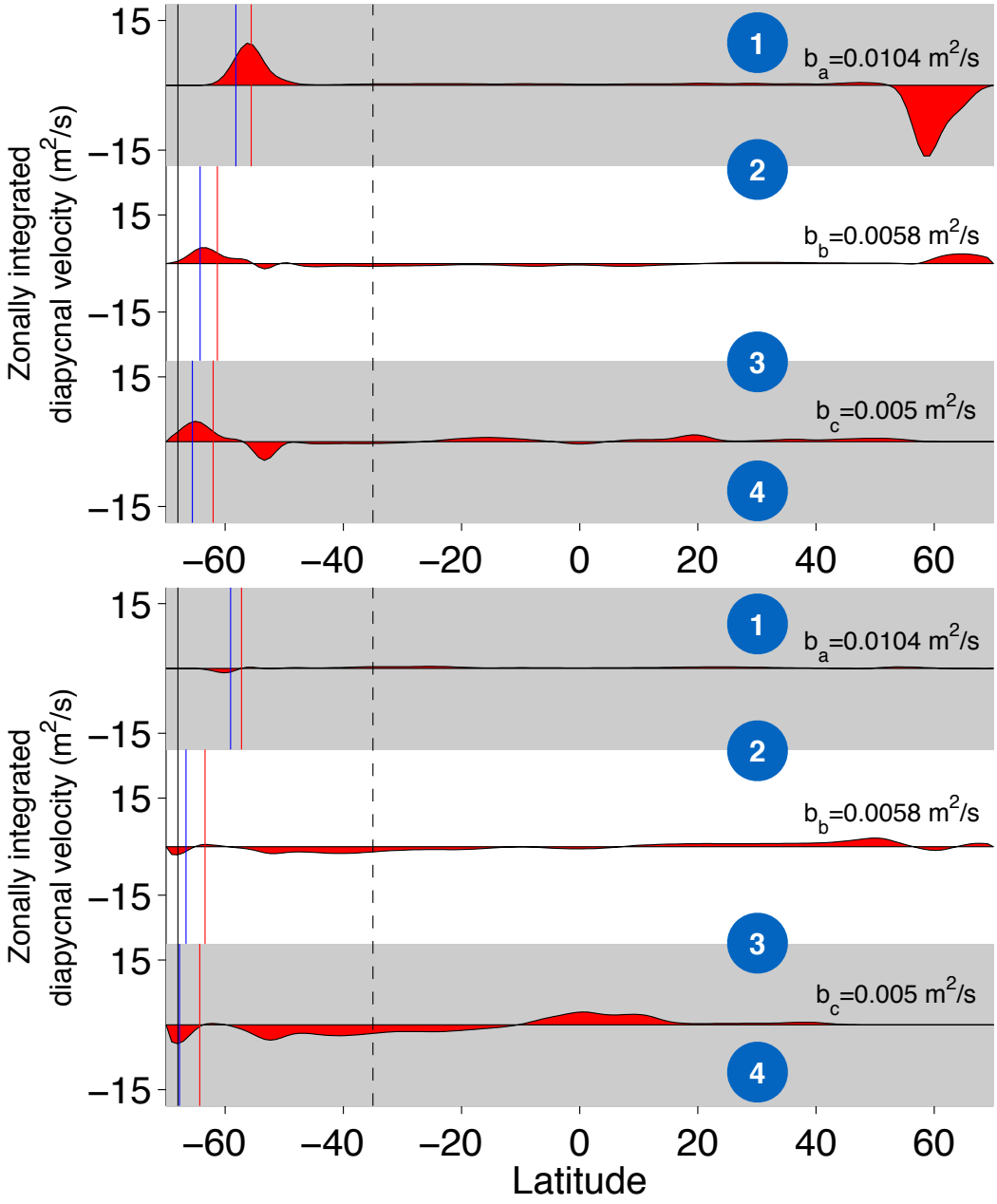

Figure 5.7: The zonally integrated diapycnal velocity in the narrow sector (top) and in the wide sector (bottom). The vertical black dashed line indicates the end of the short continent and the vertical black solid line marks −68°. The blue vertical line marks the outcrop of each buoyancy surface, zonally averaged over the appropriate sector. Similarly, the red vertical line indicates the zonally averaged latitude (over each sector) where the isopycnal depth is 200m, i.e. the approximate depth of the mixed layer in the channel. The numbers in the blue circles indicate the density class above and below each isopycnal. This figure is for the 3rd order DST advection scheme.

advection schemes: this is an upper bound on the continuous-loop transport.

Figures 5.6 and 5.7 show that most abyssal water formation occurs at depth (most downward diapycnal transport across b_c is equatorward of the mixed layer in the bottom panels of figures 5.6 and 5.7). Under 1Sv of abyssal water is formed in the mixed layer (downward diapycnal transport across b_c poleward of the mixed-layer latitude in the bottom panels of figures 5.6 and 5.7). Lumpkin & Speer (2007) hypothesize that entrainment increases the density of lower deep water in the channel, contributing to bottom water formation. Entrainment is likely augmented by the higher vertical diffusivity at depth: this explains the large amount of abyssal water formation below 2000m (see large downward transport below 2000m at about -50° in all panels of figure 5.3).

For the SOM scheme, a total of 17.4Sv sinks in the north of the narrow basin (the sum of the two arrows in the purple rectangle in the top panel of figure 5.4). 5Sv of this upwells in the narrow basin, so it cannot participate in the global overturning. 12.7Sv leaves the narrow basin in density class 2 (this represents NADW leaving the Atlantic), and 5Sv of this 12.7Sv is part of the continuous loop. Flow out of the narrow basin in density class 3 is not included in the downward branch of the continuous loop, because it returns upwelled abyssal water southward (see density class 3 in the top panel of figure 5.4). 9.7Sv of abyssal water is formed in the channel (this represents AABW formation). 5Sv follows the continuous loop from density class 1 of the narrow basin into density class 4 before returning to the surface (green arrows in figure 5.4).

For the 3rd order DST scheme, a total of 17.8Sv sinks in the north of the narrow basin (the sum of the two arrows in the purple rectangle in the top panel of figure 5.5). 4.9Sv of this upwells in the narrow basin, so it cannot participate in the global overturning. 13.2Sv leaves the narrow basin in density class 2 (this represents NADW leaving the Atlantic) and 5Sv of this 13.2Sv follows the continuous loop. Again, flow out of the narrow basin in density class 3 is not included in the downward branch of the continuous loop, because it returns

upwelled abyssal water southward (see density class 3 in the top panel of figure 5.5). 11.2Sv of abyssal water is formed in the channel (this represents AABW formation). 5Sv follows the continuous loop from density class 1 of the narrow basin into density class 4 before returning to the surface (green arrows in figure 5.5). Although more deep and abyssal water is formed with the 3rd order DST advection scheme, the transport of the continuous loop is similar for both advection schemes.

For both advection schemes, about 40% of the 13Sv of deep water leaving the narrow basin follows the continuous loop from density class 1 of the narrow basin to density class 4 and back again. This contrasts with Lumpkin & Speer (2007) and Talley (2013)'s observations, which suggest that more than 70% of the 18Sv leaving the Atlantic basin at 32°S follow the continuous loop. The transports in our model are likely to be smaller than observed transports because our channel has a smaller longitudinal extent than the Southern Ocean. It is not clear how this difference affects the fraction of deep water following the continuous loop.

5.4 The pathway of a passive tracer

The residual budget shows the strength of the continuous loop in our model, but it does not give the timescale associated with this route. Here, we use the adjoint model of the MITgcm to find the transit time of buoyancy through the downward branch of the continuous loop. We examine the sensitivity of the passive tracer concentration in a tagged region to tracer distributions at previous times. This is analogous to running the model backwards in time to discover where the tracer in the tagged region came from (Vukićević & Hess, 2000). Henceforth the sensitivity to tracer concentration at previous times is referred to as the adjoint tracer concentration.

The advection-diffusion equation for a passive tracer is

$$(\partial_t + u^\dagger \partial_x + v^\dagger \partial_y + w^\dagger \partial_z) C = \boldsymbol{\nabla} \cdot (\mathbf{K} \boldsymbol{\nabla} C) + (\kappa_v C_z)_z + \xi \,, \tag{5.8}$$

where C is the tracer concentration, ξ is the mixing by the convection scheme, $\mathbf{K}$ is the Redi tensor given by

$$\mathbf{K} \equiv \kappa_{GM} \begin{pmatrix} 1 & 0 & -\frac{b_x}{b_z} \\ 0 & 1 & -\frac{b_y}{b_z} \\ -\frac{b_x}{b_z} & -\frac{b_y}{b_z} & \left| \frac{\nabla_h b}{b_z} \right|^2 \end{pmatrix} , \tag{5.9}$$

and κ_{GM} is the Gent-McWilliams diffusion coefficient. The advection-diffusion equation for the adjoint tracer is (c.f. Todd *et al.* 2012)

$$-(\partial_t + u^\dagger \partial_x + v^\dagger \partial_y + w^\dagger \partial_z) A = \boldsymbol{\nabla} \cdot (\mathbf{K} \boldsymbol{\nabla} C) + (\kappa_v C_z)_z + \xi \,, \tag{5.10}$$

where A is the adjoint tracer concentration. The cross-isopycnal Redi transport is small. Hence, the transport of tracer, C, approximates the transport of buoyancy.

The tagged region, where the adjoint tracer is located at year 0, is situated in density classes 3 and 4, north of -35° in the wide basin (hatched region in figures 5.8 and 5.9). This roughly represents the location of AABW in the deep Indo-Pacific. At year 0, the concentration of adjoint tracer in the tagged region is 1 arbitrary tracer unit per unit volume (1ATU/m^3). There is a no-flux condition at the surface, so the volume-integral of the adjoint tracer concentration over the whole domain is constant.

The zonally-integrated thickness-weighted adjoint tracer concentration (c.f. Young 2012) is defined as

$$\int_0^{L_x} \hat{A}(y, \tilde{b}, t) \, \mathrm{d}x \equiv \int_0^{L_x} \int_{-H}^{0} A \mathcal{H} \left[b(x, y, z, t) - \tilde{b} \right] \, \mathrm{d}z \, \mathrm{d}x \,. \tag{5.11}$$

Figure 5.8 shows the transit time of $\int_0^{L_x} \hat{A}\, dx$. The transit time is defined as the first time when the zonal integral of $\hat{A}$ exceeds 50% of its equilibrium value, i.e. its value when the tracer is spread uniformly across the whole domain (c.f. Holzer 1999). We choose this definition of transit time because it does not require a long timeseries, and our adjoint run is only 500yrs long. This definition of transit time gives reasonable results even if $\int_0^{L_x} \hat{A}\, dx$ is still rising in some locations.

Figure 5.8 shows the transit time of $\int_0^{L_x} \hat{A}\, dx$, which is the timescale for adjoint tracer to reach a given latitude and depth. This transit time is equal to the forward-run timescale for buoyancy to travel from that latitude and depth into the tagged region.

The transit time of adjoint tracer from density classes 3 and 4 of the wide basin to density class 1 in the north of the narrow basin is 250yrs (top panel of figure 5.8). In other words, 250yrs is the timescale of the continuous loop's downward branch. Hence, 500yrs (the length of our run) is long enough to characterize the downward branch of the continuous loop. Very little adjoint tracer reaches density class 1 of the wide basin in our 500yr run, so our timeseries is not long enough to characterize the continuous loop's upward branch.

The adjoint tracer is transported from density class 3 to density class 2 of the wide basin on a timescale of less than 50 yrs (bottom panel of figure 5.8 north of $-35°$), without passing through the upper ocean of the channel (transit time is greater than 100yrs in the bottom panel of figure 5.8 south of $-60°$ and above -800m). In density class 2, the adjoint tracer travels from the wide basin to the equator of the narrow basin on a timescale of about 200yrs (subtract the minimum transit time in density class 2 of the wide basin from the minimum transit time in density class 2 at the equator of the narrow basin in figure 5.8).

The transit times in figure 5.8 indicate that in a forward run, some downward transport of tracer from density class 2 to density class 3 does not pass near the surface of the channel. This route from density class 2 to density class 3 may be provided by the diapycnal transport north of the mixed layer, as shown in the bottom panel of figure 5.7 (isopycnal b_b).

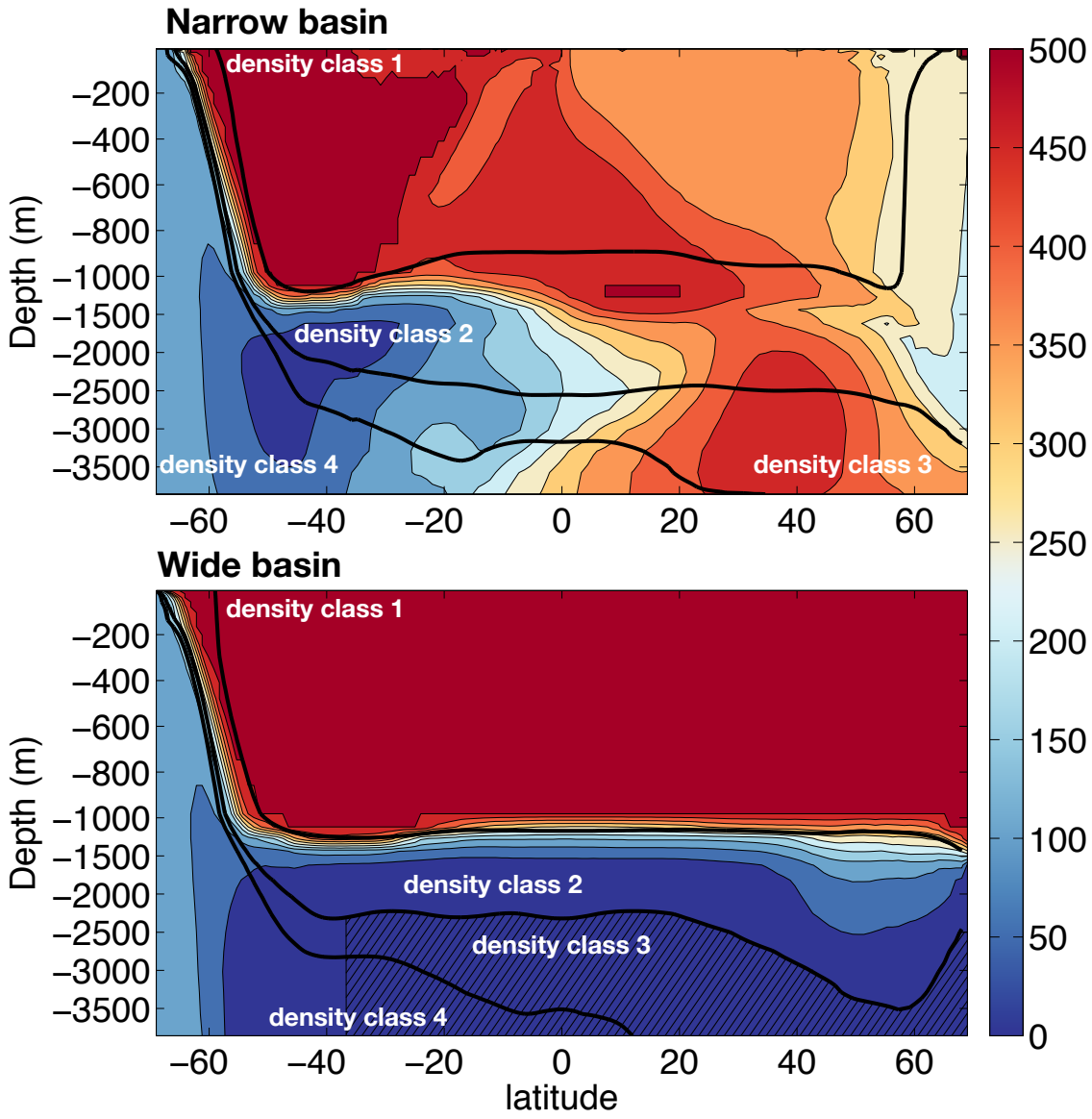

Figure 5.8: Transit time (yrs, color contours every 50yrs), defined as the first time when the zonal integral of $\hat{A}$ exceeds 50% of its equilibrium value (c.f. Holzer 1999) for the narrow basin (top) and for the wide basin (bottom). The black contours represent the dividing isopycnals $b_a = 0.0104\,\mathrm{m\,s^{-2}}$, $b_b = 0.0058\,\mathrm{m\,s^{-2}}$ and $b_c = 0.005\,\mathrm{m\,s^{-2}}$. The hatching indicates the location of the adjoint tracer at year 0. This adjoint experiment is only 500yrs long, so the transit time is capped at 500yrs.

The timescale for isopycnal flow between basins in density class 2 is about 200yrs.

Figure 5.9 shows the adjoint tracer concentration vertically integrated in each density class, normalized by $\int_{-4000m}^{0m} 1 \text{ ATU/m}^3 \, dz = 4000\text{ATU/m}^2$, for a selection of times. High adjoint tracer concentration at a given point in figure 5.9 indicates that in a forward run, that point contributes to the tracer concentration of the tagged region. Regions with low adjoint tracer concentrations in figure 5.9 do not affect the tracer concentration in the tagged region when the model is run forwards.

The route of the adjoint tracer is the reverse of the route that buoyancy follows in a forward run. The adjoint tracer upwells from density class 3 to density class 2 near the equator of the wide basin, proceeding southward along the western boundary of the wide basin (figure 5.9b). It enters the narrow basin by passing westward south of the short continent (figure 5.9f,j), follows the narrow basin's western boundary northward and then upwells into density class 1 in the north of the narrow basin (figure 5.9m).

Thus in a forward run, buoyancy near the surface of the narrow basin sinks into density class 2 near the northern edge of the narrow basin, proceeding southward along the narrow basin's western boundary and then eastward south of the short continent into the wide basin. It then travels northward in a western boundary current, sinking into the abyss near the equator.

At -500yrs, 10.6% of the adjoint tracer is in density class 1, and 7.9% of the adjoint tracer is in density class 2 of the narrow basin north of $-35°$. The ROC budget suggests that all the adjoint tracer in density class 1 arrived there via the continuous loop. Hence, about 18.5% of the volume of the tagged region enters density classes 1 and 2 of the narrow basin via the continuous loop on a timescale of 500yrs. The transport of NADW into the abyss of the wide basin is approximately $0.185V/500\text{yrs} = 2.5\text{Sv}$, where V is the volume of the tagged region. 2.5Sv compares well with the continuous loop transport into the abyss of the wide basin found in the ROC budget (3Sv).

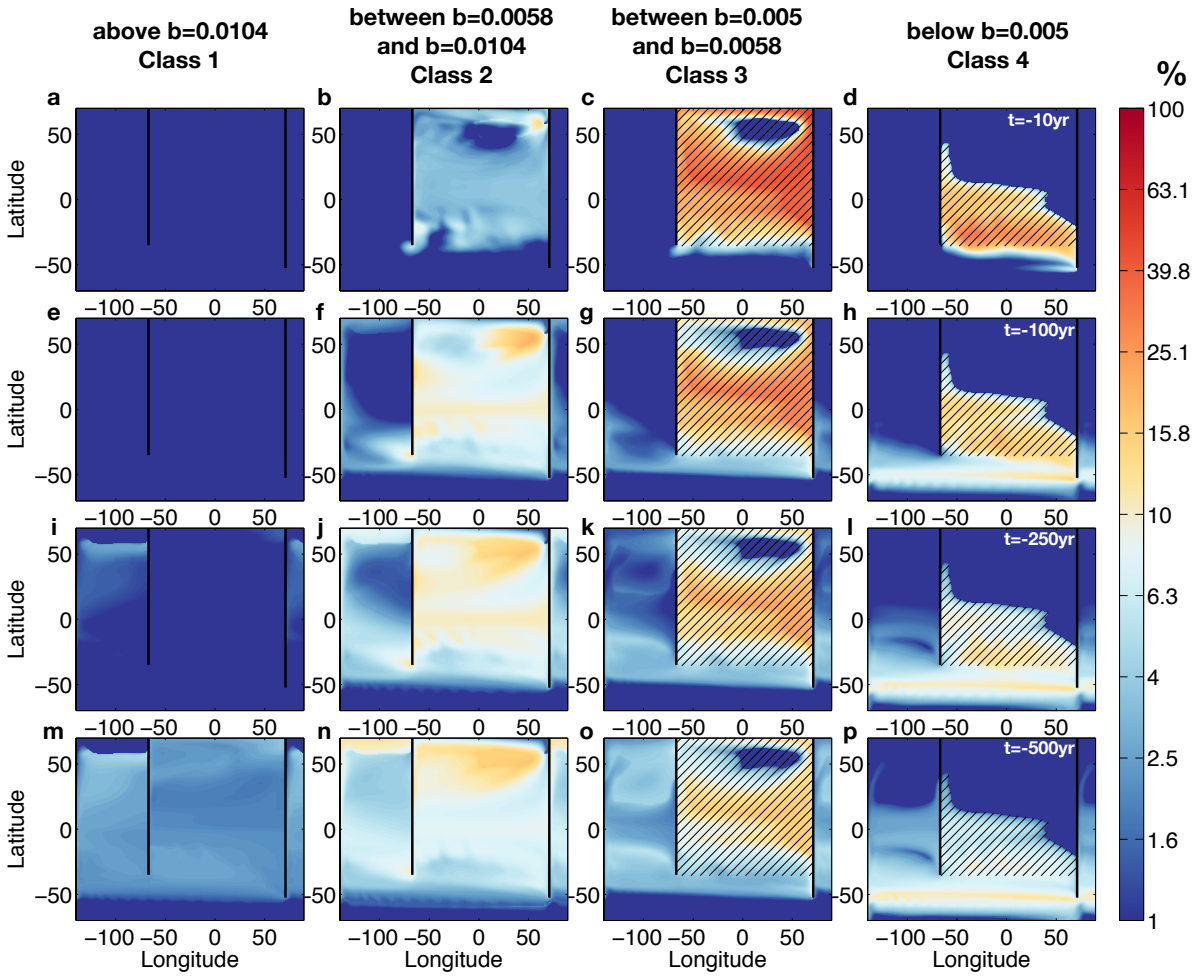

Figure 5.9: Adjoint tracer concentration, vertically integrated **a** across density class 1 at year -10, **b** across density class 2 at year -10, **c** across density class 3 at year -10, **d** across density class 4 at year -10, **e** across density class 1 at year -100, **f** across density class 2 at year -100, **g** across density class 3 at year -100, **h** across density class 4 at year -100, **i** across density class 1 at year -250, **j** across density class 2 at year -250, **k** across density class 3 at year -250, **l** across density class 4 at year -250, **m** across density class 1 at year -500, **n** across density class 2 at year -500, **o** across density class 3 at year -500 and **p** across density class 4 at year -500. Normalized by $\int_{-4000m}^{0m} 1 \text{ ATU/m}^3 \, dz$, so units are %. At year 0, the adjoint tracer is in density classes 3 and 4 of the wide basin, as indicated by the hatching. The westernmost 20° of the domain is repeated to the right of the figure.

5.5 Summary and Discussion

We use a budget of the residual circulation to estimate how much residual transport follows the continuous pathway versus the two-cell loops in an idealized-geometry primitive-equation model. A schematic of these pathways is shown in figure 1.1. The residual budget indicates that in our two-basin ocean-only model, 12.7Sv sinks in the narrow basin and travels southward into the channel. Of this 12.7Sv, only about 40% proceeds along the continuous loop. This is compatible with Thompson *et al.* (2016), who predict that when the vertical diffusivity above 2000m is reduced, as it is in our model, the continuous loop is small compared with the total rate of deep-water formation. However, our estimate is smaller than Lumpkin & Speer (2007) and Talley (2013)'s observations, which suggest that more than 70% of the 18Sv leaving the Atlantic basin at 32°S follow the continuous loop. Below 500m in the channel of our model, significant amounts of deep water are converted into bottom water. This deep water may be entrained by bottom water formed at the surface, as suggested by Lumpkin & Speer (2007).

Our channel has a smaller longitudinal extent than the Southern Ocean, so the transports of the cells and the continuous pathway in our model are smaller than the observed transports. It is not clear how this affects the fraction of deep water that follows the continuous pathway.

For a buoyancy-like tracer, the adjoint MITgcm is used to find the sensitivity of tracer concentration in the abyss to tracer concentration throughout the domain at previous times. The adjoint tracer concentration in the upper ocean suggests that about 2.5Sv follows the continuous pathway through the abyss of the wide basin. This estimate is close to the 3Sv found by the ROC budget.

Acknowledgements

Chapter 5, in full, is in preparation for submission to the Journal of Physical Oceanography. Jones, C. S.; Cessi, Paola, American Meteorological Society.

Bibliography

Allison, Lesley Catherine 2009 Spin-up and adjustment of the Antarctic Circumpolar Current and global pycnocline. PhD thesis, University of Reading.

Andrews, D. G. & McIntyre, M. E. 1978 Generalized Eliassen-Palm and Charney-Drazin theorems for waves on axismmetric mean flows in compressible atmospheres. *J. Atmos. Sci.* **35** (2), 175–185.

Antonov, J. I., Locarnini, R. A., Boyer, T. P., Mishonov, A. V. & Garcia, H. E. 2006 *World Ocean Atlas 2005, Volume 2: Salinity*. Washington, D.C.: U.S. Government Printing Office.

Biastoch, Arne & Böning, Claus W. 2013 Anthropogenic impact on Agulhas leakage. *Geophysical Research Letters* **40** (6), 1138–1143.

Biastoch, Arne, Böning, Claus W, Schwarzkopf, Franziska U & Lutjeharms, JRE 2009 Increase in Agulhas leakage due to poleward shift of Southern Hemisphere westerlies. *Nature* **462** (7272), 495–498.

Boccaletti, G., Ferrari, R., Adcroft, A., Ferreira, D. & Marshall, J. 2005 The vertical structure of ocean heat transport. *Geophysical Research Letters* **32** (10).

Bower, Amy S., Lozier, M. Susan, Gary, Stefan F. & Boning, Claus W. 2009 Interior pathways of the North Atlantic meridional overturning circulation. *Nature* **459** (7244), 243–247.

Broecker, Wallace S. 1991 The great ocean conveyor. *Oceanography* **4** (2), 79–89.

Broecker, W S, Peng, T H, Jouzel, Jean & Russell, Gary 1990 The magnitude of global fresh-water transports of importance to ocean circulation. *Climate Dynamics* **4** (2), 73–79.

Bryan, Frank O, Böning, Claus W, Holland, William R, Bryan, Frank O & Holland, William R 1995 On the midlatitude circulation in a high-resolution model of the North Atlantic. *J. Phys. Oceanogr.* **25** (3), 289–305.

Cessi, P. & Jones, C. S. 2017 Warm-route versus cold-route interbasin exchange in the meridional overturning circulation. *J. Phys. Oceanogr.* **47** (8), 2053–2080.

Childress, Stephen & Gilbert, Andrew D 2008 Magnetic Structure in Steady Integrable Flows. In *Stretch, twist, fold: the fast dynamo*, pp. 124–127. Springer Science & Business Media.

Collins, M.and Knutti, R., Arblaster, J., Dufresne, J-N., Fichefet, T., Friedlingstein, P., Gao, X., Gutowski, W.J., Johns, T., Krinner, G., Shongwe, M., Tebaldi, C., Weaver, A.J. & Wehner, M. 2013 Long-term Climate Change: Projections, Commitments and Irreversibility. In *Climate Change 2013: The Physical Science Basis. Contribution of Working Group I to the Fifth Assessment Report of the Intergovernmental Panel on Climate Change*, p. 1029. Cambridge University Press.

Craig, Phil, Ferreira, David & Methven, John 2016 The contrast between Atlantic and Pacific surface water fluxes. *Tellus Series A: Dynamic Meteorology and Oceanography* **69** (1), 1–15.

Danabasoglu, Gokhan & McWilliams, James C. 1995 Sensitivity of the global ocean circulation to parameterizations of mesoscale tracer transports. *J. Climate* **8** (12), 2967–2987.

Eden, Carsten & Willebrand, Jürgen 2001 Mechanism of interannual to decadal variability of the North Atlantic circulation. *Journal of Climate* **14** (10), 2266–2280.

Ferrari, Raffaele, Griffies, Stephen M., Nurser, A. J. George & Vallis, Geoffrey K. 2010 A boundary-value problem for the parameterized mesoscale eddy transport. *Ocean Modell.* **32**, 143–156.

Ferrari, Raffaele, Jansen, Malte F, Adkins, Jess F, Burke, Andrea, Stewart, Andrew L & Thompson, Andrew F 2014 Antarctic sea ice control on ocean circulation in present and glacial climates. *Proceedings of the National Academy of Sciences* **111** (24), 8753–8758.

Ferrari, Raffaele, Nadeau, Louis-Philippe, Marshall, David P, Allison, Lesley C & Johnson, Helen L 2017 A model of the ocean overturning circulation with two closed basins and a reentrant channel. *Journal of Physical Oceanography* **47** (12), 2887–2906.

Ferreira, David, Marshall, John & Campin, Jean-Michel 2010 Localization of deep water formation: Role of atmospheric moisture transport and geometrical constraints on ocean circulation. *J. Climate* **23** (6), 1456–1476.

Garabato, Alberto C Naveira, Polzin, Kurt L, King, Brian A, Heywood, Karen J & Visbeck, Martin 2004 Widespread intense turbulent mixing in the Southern Ocean. *Science* **303** (5655), 210–213.

Geay, J Emile, Cane, M A & Naik, N 2003 Warren revisited: Atmospheric freshwater fluxes and "Why is no deep water formed in the North Pacific". *Journal of Geophysical Research: Oceans* **108** (C6).

Gebbie, Geoffrey, Huybers, Peter, Gebbie, Geoffrey & Huybers, Peter 2010 Total Matrix Intercomparison: A Method for Determining the Geometry of Water-Mass Pathways. *J. Phys. Oceanogr.* **40** (8), 1710–1728.

Gent, Peter R, Danabasoglu, Gokhan, Donner, Leo J, Holland, Marika M, Hunke, Elizabeth C, Jayne, Steve R, Lawrence, David M, Neale, Richard B, Rasch, Philip J, Vertenstein, Mariana, Worley, Patrick H, Yang, Zong-Liang, Zhang, Minghua, Danabasoglu, Gokhan, Donner, Leo J, Holland, Marika M, Hunke, Elizabeth C, Jayne, Steve R, Lawrence, David M, Neale, Richard B, Rasch, Philip J, Vertenstein, Mariana, Worley, Patrick H, Yang, Zong-Liang & Zhang, Minghua 2011 The Community Climate System Model Version 4. *J. Climate* **24** (19), 4973–4991.

Gent, Peter R. & McWilliams, James C. 1990 Isopycnal mixing in ocean circulation models. *J. Phys. Oceanogr.* **20** (1), 150–155.

Gnanadesikan, Anand 1999 A simple predictive model for the structure of the oceanic pycnocline. *Science* **283** (5410), 2077–2079.

Gordon, Arnold L 1985 Indian-Atlantic transfer of thermocline water at the Agulhas retroflection. *Science* **227**, 1030–1034.

Gordon, Arnold L. 1986 Interocean exchange of thermocline water. *Journal of Geophysical Research: Oceans* **91** (C4), 5037–5046.

Gordon, Arnold L, Lutjeharms, Johann R E & Gründlingh, Marten L 1987 Stratification and circulation at the Agulhas Retroflection. *Deep Sea Research Part A. Oceanographic Research Papers* **34** (4), 565–599.

Gordon, Arnold L, Weiss, Ray F, Smethie, William M & Warner, Mark J 1992 Thermocline and intermediate water communication between the South Atlantic and Indian Oceans. *Journal of Geophysical Research: Oceans* **97** (C5), 7223–7240.

Häkkinen, Sirpa & Rhines, Peter B. 2004 Decline of Subpolar North Atlantic Circulation During the 1990s. *Science* **304** (5670), 555–559.

Hallberg, Robert & Gnanadesikan, Anand 2006 The role of eddies in determining the structure and response of the wind-driven Southern Hemisphere overturning: Results from the Modeling Eddies in the Southern Ocean (MESO) project. *Journal of Physical Oceanography* **36** (12), 2232–2252.

Hátún, Hjálmar, Sandø, Anne Britt, Drange, Helge, Hansen, Bogi & Valdimarsson, Heðinn 2005 Influence of the Atlantic subpolar gyre on the thermohaline circulation. *Science* **309** (5742), 1841–1844.

Held, Isaac M & Schneider, Tapio 1999 The surface branch of the zonally averaged mass transport circulation in the troposphere. *Journal of the atmospheric sciences* **56** (11), 1688–1697.

Hewitt, C, Stouffer, R, Broccoli, A, Mitchell, J & Valdes, Paul J 2003 The effect of ocean dynamics in a coupled GCM simulation of the Last Glacial Maximum. *Climate Dynamics* **20** (2-3), 203–218.

Holzer, Mark 1999 Analysis of passive tracer transport as modeled by an atmospheric general circulation model. *Journal of climate* **12** (6), 1659–1684.

Hughes, Tertia M. C. & Weaver, Andrew J. 1994 Multiple equilibria of an asymmetric two-basin ocean model. *J. Phys. Oceanogr.* **24** (3), 619–637.

Huisman, Selma, Dijkstra, Henk A., von der Heydt, A. & de Ruijter, W. P. M. 2009 Robustness of multiple equilibra in the global ocean circulation. *Geophys. Res. Lett.* **36**, L01610.

Huisman, Selma E, Dijkstra, Henk A, von der Heydt, A S, de Ruijter, W P M, von der Heydt, A S & de Ruijter, W P M 2012 Does net E-P set a preference for North Atlantic sinking? *J. Phys. Oceanogr.* **42** (11), 1781–1792.

Hundsdorfer, Willem, Koren, Barry, Verwer, JG & others 1995 A positive finite-difference advection scheme. *Journal of computational physics* **117** (1), 35–46.

Jansen, Malte F & Nadeau, Louis-Philippe 2016 The effect of Southern Ocean surface buoyancy loss on the deep-ocean circulation and stratification. *Journal of Physical Oceanography* **46** (11), 3455–3470.

Jones, C. S. & Cessi, P. 2016 Interbasin transport of the meridional overturning circulation. *J. Phys. Oceanogr.* **46** (4), 1157–1169.

Jones, C. S. & Cessi, P. 2017 Size matters: another reason why the Atlantic is saltier than the Pacific . *J. Phys. Oceanogr.* **47** (11), 2843–2859.

Kamphuis, V, Huisman, S E & Dijkstra, H A 2011 The global ocean circulation on a retrograde rotating earth. *Climate of the Past* **7** (2), 487–499.

Kang, Sarah M, Held, Isaac M, Frierson, Dargan MW & Zhao, Ming 2008 The response of the ITCZ to extratropical thermal forcing: Idealized slab-ocean experiments with a GCM. *Journal of Climate* **21** (14), 3521–3532.

Karsten, Richard, Jones, Helen & Marshall, John 2002 The role of eddy transfer in setting the stratification and transport of a circumpolar current. *Journal of Physical Oceanography* **32** (1), 39–54.

Landerer, Felix W, Jungclaus, Johann H & Marotzke, Jochem 2007 Regional dynamic and steric sea level change in response to the ipcc-a1b scenario. *Journal of Physical Oceanography* **37** (2), 296–312.

Levermann, Anders, Griesel, Alexa, Hofmann, Matthias, Montoya, Marisa & Rahmstorf, Stefan 2005 Dynamic sea level changes following changes in the thermohaline circulation. *Climate Dynamics* **24** (4), 347–354.

Lévy, M., Klein, P., Tréguier, A.-M., Iovino, D., Madec, G., Masson, S. & Takahashi, K. 2010 Modifications of gyre circulation by sub-mesoscale physics. *Ocean Modelling* **34** (1), 1–15.

Locarnini, R. A., Mishonov, A. V., Antonov, J. I., Boyer, T. P. & Garcia, H. E. 2006 *World Ocean Atlas 2005, Volume 1: Temperature*. Washington, D.C.: U.S. Government Printing Office.

Lumpkin, Rick & Speer, Kevin 2007 Global ocean meridional overturning. *Journal of Physical Oceanography* **37** (10), 2550–2562.

Maier-Reimer, Ernst & Hasselmann, Klaus 1987 Transport and storage of CO_2 in the ocean: an inorganic ocean-circulation carbon cycle model. *Climate dynamics* **2** (2), 63–90.

Marotzke, Jochem & Willebrand, Jürgen 1991 Multiple equilibria of the global thermohaline circulation. *J. Phys. Oceanogr.* **21** (9), 1372–1385.

Marshall, David P., Munday, R. David, Allison, Lesley C., Hay, Russell J. & Johnson, Helen L. 2016 Gill's model of the antarctic circumpolar current, revisited: The role of latitudinal variations in wind stress. *Ocean Modelling* **97**, 37–51.

Marshall, John, Adcroft, Alistair, Hill, Chris, Perelman, Lev & Heisey, Curt 1997*a* A finite-volume, incompressible Navier Stokes model for studies of the ocean on parallel computers. *J. Geophys. Res.* **102** (C3), 5753–5766.

Marshall, John, Hill, Chris, Perelman, Lev & Adcroft, Alistair 1997*b* Hydrostatic, quasi-hydrostatic, and nonhydrostatic ocean modeling. *J. Geophys. Res.* **102** (C3), 5733–5752.

Marshall, John & Radko, Timour 2003 Residual-mean solutions for the antarctic circumpolar current and its associated overturning circulation. *Journal of Physical Oceanography* **33** (11), 2341–2354.

Marshall, John & Speer, Kevin 2012 Closure of the meridional overturning circulation through southern ocean upwelling. *Nature Geoscience* **5** (3), 171.

McCartney, Michael S & Mauritzen, Cecilie 2001 On the origin of the warm inflow to the Nordic Seas. *Progress in Oceanography* **51** (1), 125–214.

Munk, Walter H. 1966 Abyssal recipes. *Deep Sea Research and Oceanographic Abstracts* **13** (4), 707 – 730.

Nikurashin, Maxim & Vallis, Geoffrey 2012 A theory of the interhemispheric meridional overturning circulation and associated stratification. *Journal of Physical Oceanography* **42** (10), 1652–1667.

Nilsson, Johan, Langen, Peter L., Ferreira, David & Marshall, John 2013 Ocean basin geometry and the salinification of the Atlantic Ocean. *J. Climate* **26**, 6163–6184.

Osborn, TR 1980 Estimates of the local rate of vertical diffusion from dissipation measurements. *Journal of Physical Oceanography* **10** (1), 83–89.

Prather, Michael J. 1986 Numerical advection by conservation of second-order moments. *J. Geophys. Res.* **91** (D6), 6671–6681.

Rahmstorf, Stefan 1996 On the freshwater forcing and transport of the Atlantic thermohaline circulation. *Climate Dynamics* **12** (12), 799–811.

Redi, M. H. 1982 Oceanic isopycnal mixing by coordinate rotation. *J. Phys. Oceanogr.* **12** (10), 1154–1158.

Reid, Joseph L. 1961 On the temperature, salinity, and density differences between the Atlantic and Pacific oceans in the upper kilometre. *Deep Sea Research (1953)* **7** (4), 265 – 275.

Reid, Joseph L 1979 On the contribution of the Mediterranean Sea outflow to the Norwegian-Greenland Sea. *Deep Sea Research Part A. Oceanographic Research Papers* **26** (11), 1199–1223.

Ridgway, KR & Dunn, JR 2007 Observational evidence for a southern hemisphere oceanic supergyre. *Geophysical Research Letters* **34** (13).

Rintoul, Stephen Rich 1991 South Atlantic interbasin exchange. *Journal of Geophysical Research: Oceans* **96** (C2), 2675–2692.

Schmitt, Raymond W, Bogden, Philip S, Dorman, Clive E, Schmitt, Raymond W, Bogden, Philip S & Dorman, Clive E 1989 Evaporation minus precipitation and density fluxes for the North Atlantic. *J. of Phys. Oceanogr.* **19** (9), 1208–1221.

Schmittner, Andreas, Silva, Tiago AM, Fraedrich, Klaus, Kirk, Edilbert & Lunkeit, Frank 2011 Effects of mountains and ice sheets on global ocean circulation. *Journal of Climate* **24** (11), 2814–2828.

Seager, Richard, Liu, Haibo, Henderson, Naomi, Simpson, Isla, Kelley, Colin, Shaw, Tiffany, Kushnir, Yochanan, Ting, Mingfang, Liu, Haibo, Henderson, Naomi, Simpson, Isla, Kelley, Colin, Shaw, Tiffany, Kushnir, Yochanan & Ting, Mingfang 2014 Causes of Increasing Aridification of the Mediterranean Region in Response to Rising Greenhouse Gases*. *J. Climate* **27** (12), 4655–4676.

Seager, Richard, Naik, Naomi & Vecchi, Gabriel A 2010 Thermodynamic and dynamic mechanisms for large-scale changes in the hydrological cycle in response to global warming. *J. Climate* **23** (17), 4651–4668.

van Sebille, E., Biastoch, A., van Leeuwen, P. J. & de Ruijter, W. P. M. 2009 A weaker Agulhas Current leads to more Agulhas leakage. *Geophysical Research Letters* **36** (3).

Seidov, Dan & Haupt, Bernd J. 2005 How to run a minimalist's global ocean conveyor. *Geophysical Research Letters* **32** (7).

Speich, Sabrina, Blanke, Bruno & Madec, Gurvan 2001 Warm and cold water routes of an OGCM thermohaline conveyor belt. *Geophysical Research Letters* **28** (2), 311–314.

Speich, Sabrina, Blanke, Bruno, de Vries, Pedro, Drijfhout, Sybren, Döös, Kristofer, Ganachaud, Alexandre & Marsh, Robert 2002 Tasman leakage: A new route in the global ocean conveyor belt. *Geophysical Research Letters* **29** (10), 55–1–55–4.

Stocker, T. F. & Wright, D. G. 1991 A zonally averaged ocean model for the thermohaline circulation. Part II: Interocean circulation in the Pacific-Atlantic basin system. *J. Phys. Oceanogr.* **21** (12), 1725–1739.

Stocker, Thomas F., Wright, Daniel G. & Broecker, Wallace S. 1992 The influence of high-latitude surface forcing on the global thermohaline circulation. *Paleoceanogr.* **7** (5), 529–541.

Stommel, Henry 1957 A survey of ocean current theory. *Deep Sea Research (1953)* **4**, 149–184.

Stommel, Henry 1958 The abyssal circulation. *Deep Sea Research (1953)* **5** (1), 80 – 82.

Stommel, Henry 1961 Thermohaline convection with two stable regimes of flow. *Tellus* **13** (2), 224–230.

Stommel, Henry & Arons, AB 1959 On the abyssal circulation of the world ocean i. stationary planetary flow patterns on a sphere. *Deep Sea Research (1953)* **6**, 140–154.

Talley, L D 2008 Freshwater transport estimates and the global overturning circulation: Shallow, deep and throughflow components. *Progress in Oceanography* **78** (4), 257–303.

Talley, Lynne D. 2013 Closure of the Global Overturning Circulation Through the Indian, Pacific, and Southern Oceans: Schematics and Transports. *Oceanography* **26**.

Talley, Lynne D, Pickard, George L, Emery, William J & Swift, James H 2011 *Descriptive Physical Oceanography*, pp. 298–301, 498–499. Elsevier.

Thompson, Andrew F, Stewart, Andrew L & Bischoff, Tobias 2016 A multibasin residual-mean model for the global overturning circulation. *Journal of Physical Oceanography* **46** (9), 2583–2604.

Todd, Robert E, Rudnick, Daniel L, Mazloff, Matthew R, Cornuelle, Bruce D & Davis, Russ E 2012 Thermohaline structure in the california current system: Observations and modeling of spice variance. *Journal of Geophysical Research: Oceans* **117** (C2).

Toggweiler, JR & Samuels, B 1993 Is the magnitude of the deep outflow from the Atlantic Ocean actually governed by Southern Hemisphere winds? In *The Global Carbon Cycle*, pp. 303–331. Springer.

Toggweiler, JR & Samuels, B 1995 Effect of drake passage on the global thermohaline circulation. *Deep Sea Research Part I: Oceanographic Research Papers* **42** (4), 477–500.

Toggweiler, JR & Samuels, B 1998 On the ocean's large-scale circulation near the limit of no vertical mixing. *Journal of Physical Oceanography* **28** (9), 1832–1852.

Vallis, Geoffrey K 2006 *Atmospheric and Oceanic Fluid Dynamics: Fundamentals and Large-scale Circulation*, pp. 586–587. Cambridge Univ. Press.

Vukićević, Tomislava & Hess, Peter 2000 Analysis of tropospheric transport in the pacific basin using the adjoint technique. *Journal of Geophysical Research: Atmospheres* **105** (D6), 7213–7230.

Wang, Xiaoli, Stone, Peter H. & Marotzke, Jochem 1995 Poleward heat transport in a barotropic ocean model. *J. Phys. Oceanogr.* **25** (2), 256–265.

Warren, Bruce A 1981 *Evolution of physical oceanography*, chap. Deep circulation of the world ocean, pp. 6–41. MIT Press, Cambridge, MA.

Warren, Bruce A. 1983 Why is no deep water formed in the North Pacific? *J. Mar. Res.* **41** (2), 327–347.

Warren, Bruce A 1990 Suppression of deep oxygen concentrations by drake passage. *Deep Sea Research Part A. Oceanographic Research Papers* **37** (12), 1899–1907.

Waterhouse, Amy F, MacKinnon, Jennifer A, Nash, Jonathan D, Alford, Matthew H, Kunze, Eric, Simmons, Harper L, Polzin, Kurt L, St. Laurent, Louis C, Sun, Oliver M, Pinkel, Robert & others 2014 Global patterns of diapycnal mixing from measurements of the turbulent dissipation rate. *Journal of Physical Oceanography* **44** (7), 1854–1872.

Weaver, A. J., Bitz, C. M., Fanning, A. F. & Holland, M. M. 1999 Thermohaline circulation: High-latitude phenomena and the difference between the Pacific and Atlantic. *Annu. Rev. Earth Planet Sci.* **27** (1), 231–285.

Whalen, CB, Talley, LD & MacKinnon, JA 2012 Spatial and temporal variability of global ocean mixing inferred from argo profiles. *Geophysical Research Letters* **39** (18).

Wills, Robert C & Schneider, Tapio 2015 Stationary eddies and the zonal asymmetry of net precipitation and ocean freshwater forcing. *J. Climate* **28** (13), 5115–5133.

Wolfe, Christopher L & Cessi, Paola 2011 The adiabatic pole-to-pole overturning circulation. *Journal of Physical Oceanography* **41** (9), 1795–1810.

Wolfe, C. L. & Cessi, P. 2015 Multiple regimes and low-frequency variability in the quasi-adiabatic overturning circulation. *J. Phys. Oceanogr.* **45**, 1690–1708.

Wyrtki, Klaus & Kendall, Robert 1967 Transports of the Pacific equatorial countercurrent. *Journal of Geophysical Research* **72** (8), 2073–2076.

Young, William R. 2012 An exact thickness-weighted average formulation of the Boussinesq equations. *J. Phys. Oceanogr.* **42** (5), 692–707.

Zhang, Rong & Delworth, Thomas L 2005 Simulated tropical response to a substantial weakening of the Atlantic thermohaline circulation. *Journal of Climate* **18** (12), 1853–1860.

Zhang, R. & Vallis, G. K. 2007 The role of bottom vortex stretching on the path of the north atlantic western boundary current and on the northern recirculation gyre. *J. Phys. Oceanogr.* **37** (8), 2053–2080.